DIRECT LASER DEPOSITION OF POROUS STRUCTURES AND GRADIENT METAL-CERAMIC COMPOSITE COATINGS

By

THOMAS PAUL LOUIS GUALTIERI

A thesis submitted in partial fulfillment of
the requirements for the degree of

MASTER OF SCIENCE in MECHANICAL ENGINEERING

WASHINGTON STATE UNIVERSITY
Mechanical and Materials Engineering Department

APRIL 2016

To the Faculty of Washington State University:

The members of the Committee appointed to examine the thesis of THOMAS PAUL LOUIS GUALTIERI find it satisfactory and recommend that it be accepted.

_____

Amit Bandyopadhyay, Ph.D., Chair

_____

Susmita Bose, Ph.D.

_____

David P. Field, Ph.D.

ACKNOWLEDGEMENT

I would like to thank everyone and express my gratitude to all the people who helped me in one way or another while working towards my goal of finishing my degree. I would like to start with my advisor Dr. Amit Bandyopadhyay. I am very grateful that he gave me the opportunity to start working in the lab and get involved in all the projects being worked on. If not for these experiences I would never know of some of the fascinating things going on in the engineering field. I want to thank him for all the time spent helping me to develop my skills as a researcher. He provided valuable help discussing projects, working on paper drafts, providing comments, and helping me improve my work. I am very grateful for all the help and giving me the opportunity to go down this path in life. I also would like to extend my gratitude to Dr. Susmita Bose for helping me as well. She was like a second advisor who also helped and gave advice on all my projects. The words of wisdom from both of you helped me greatly during my studies and I am very appreciative for all of them.

I would like to thank all my friends and collogues who helped me in one way or another. Whether it was in the lab or outside all these people played a large role in helping me to achieve my degree. Gabriela Pereira Ferraz, thank you for your mental support, words of advice, input on projects, help to keeping me on track, and make my journey though grad school more enjoyable. Jose Marcial and John Young, thank you for all the great times, adventures, and Friday afternoon lunches. Craig Owen for helping me to find engineering, helping me with research and classes, and watching soccer. Pavlo (Pasha) Rudenko, for showing me what it's like to be in a small company and getting me involved in some great experiences. And to all the others that have helped

me but I don't have room to write about: Anish Shivaram, Himanshu Sahasrabudhe, Sahar Vahabzadeh, Dongxu Ke, and Sam Robertson.

I would also like to thank the Hydro Research Foundation and JCATI for their support and help completing these projects. Thank you for believing in me and giving me this great opportunity. The information, data, or work presented herein was funded in part by the Office of Energy Efficiency and Renewable Energy (EERE), U.S. Department of Energy, under Award Number DE-EE0002668 and the Hydro Research Foundation.

Last and most importantly I would like to thank my family. My parents Dan and Paula, and my sister Brianna. Without your help, guidance, and love none of this would be possible.

DIRECT LASER DEPOSITION OF POROUS STRUCTURES AND GRADIENT METAL-CERAMIC COMPOSITE COATINGS

Abstract

by Thomas Paul Louis Gualtieri, M.S.
Washington State University
May 2016

Chair: Amit Bandyopadhyay

Direct laser deposition is an additive manufacturing technique capable of producing complex geometries, bond different materials, repair broken parts, and add protective coating. In the present study it is used to make micro-porous scaffolds and apply protective vanadium and niobium carbide coatings. Micro-porous metal filters are a difficult thing to make but are required for many applications. In this study it was hypothesized that laser engineering net shaping (LENS) could be used to make porous Ti6Al4V scaffolds with an interconnected micro-porous structure. This proved to be true with cylinders made to have 15.9% porosity, and a pore size less than 100μm. These structures were made by only altering processing parameters, which yielded a scaffold with obstructed random pore interconnectivity. The scaffolds had a compressive strength of 645-556MPa and martensitic like α′ grains. Another study was done to apply hard niobium and vanadium carbide surface coatings to stainless steel. The objective was to used LENS to deposit stainless steel coatings with added carbides to eventually make a gradient coating with increased protective qualities. Parts that have suffered material loss from abrasive wear or cavitation could have material added back as well as add a protective coating at the same time. Compositions

ranging from 5% to 100% of the carbides were mixed with stainless steel. The coatings were then deposited on a stainless steel 304 substrate individually, as well as in a series to make a gradient structure. These coatings all increased hardness, wear resistance, and 100%VC significantly increased the materials resistance to damage from abrasive water. The carbides integrated into the SS304 matrix on the grain boundaries making a metal ceramic composite. These precipitates left residual stress in the structure which increased the hardness and wear resistance. The study proved that the addition of these carbides did increase the protective qualities and could make a gradient coating with properties tailored to the user's preference.

TABLE OF CONTENTS

LIST OF TABLES

LIST OF FIGURES

CHAPTER ONE

LASER FABRICATION OF POROUS STRUCTURES AND HARD SURFACE COATINGS

1.1 Introduction

Direct laser deposition (DLD) is an additive manufacturing (AM) technology that has recently been given much attention for its versatile abilities. DLD is one of the more advanced forms of additive manufacturing[1]. It is a form of direct energy deposition and can also be known as laser solid forming (LSF). One of the most common of these machines is laser engineering net shaping (LENS)[2]. LENS is a free form laser deposition system that can make 3D parts from a CAD file. Its additive abilities allow it to make complex geometries, bond different materials, and repair damaged parts[2–4]. DLD separates itself from other AM processes by being able deposit material simultaneously or at different points during a build. This ability to add different materials has the potential to significantly reduce processing cost and shorten product development[5,6]. It gives it much more versatility than powder bed methods, and has opened up a field of research for making new materials via laser bonding. Three research projects were conducted to explore some of LENS capabilities. The first one was trying to build micro-porous Ti6Al4V filters using LENS. The next two projects were based on making gradient metal-ceramic-composite (MCC) coatings with vanadium carbide (VC) and Niobium carbide (NbC) mixed with stainless steel. This coating could then be used to repair damaged parts that have experience material loss while simultaneously adding extra protection. All projects demonstrate the flexibility of LENS and increase the understanding of all the abilities of this AM process.

1.2 LENS Unique Capabilities

The impact that 3D printing can have on modern manufacturing is well known[7]. It is not a farfetched idea to think of custom implants being printed or astronauts printing parts in space[5,8,9]. DLD is a very lucrative AM technique due to its capabilities to make complex geometries, bond new materials, apply coatings, and repair parts. For these reasons it has been of interest to many industries such as aerospace, medical, and repair industries.

LENS operates by melting powder material with a continuous wave Nd:YAG laser then depositing it on a substrate. Powder is deposited under the laser from a hopper via argon transport. It is delivered under the laser through four nozzles that are positioned around the beam.

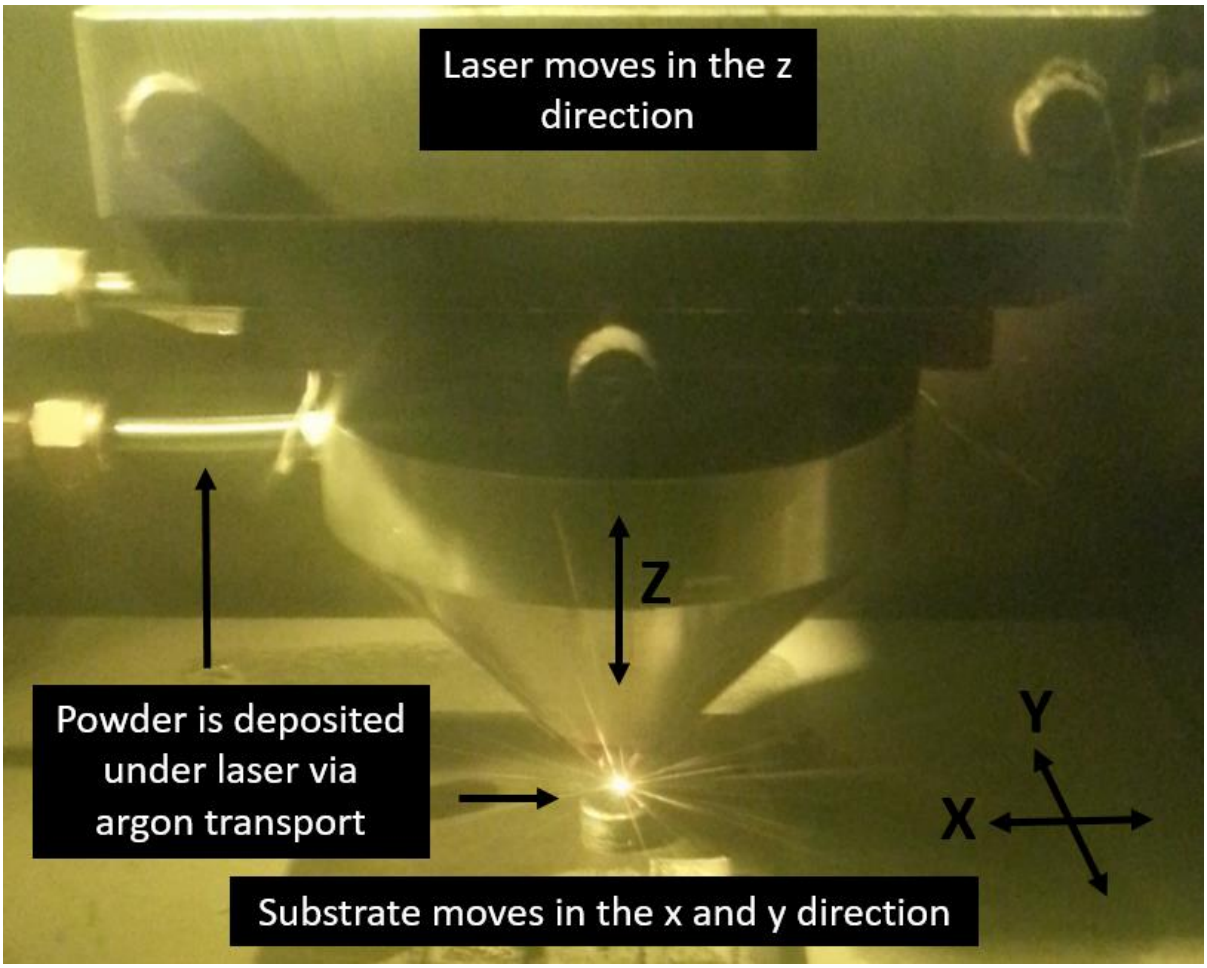

Figure 1.1: Laser Engineering Net Shaping (LENS) – A freeform powder based additive manufacturing process

The powder is then melted and deposited on the substrate where it solidifies. The platform moves in the x and y directions, and the deposition head moves in the z direction. It builds a part layer-by-layer while the laser powder, powder feed rate, scan speed, hatch angle, and hatch distance are controlled to achieve desired structure and part properties. This is all done in an argon atmosphere with oxygen levels held below 10ppm. An image of the LENS process can be seen in **Fig 1.1**.

The main thing that LENS can offer is it can build a part in a way that optimizes functionality in one process, that currently cannot be done or would take multiple steps. For example, in the past research has been done on the LENS to make custom porous hip implants[10–12]. The LENS could make the main body of the hip implant to the exact size and shape the patient requires. It could then change the build parameters to tailor the mechanical properties. In this example make a dense outside layer for strength and a porous interior to reduce the stiffness. The LENS could then add a calcium phosphate coating to the outside of the stem for increased tissue growth and add a MMC on the femoral head for increased wear resistance[3,13–15]. This shows the power of DLD and how it could make manufacturing more efficient and flexible. The LENS was able to make a complex part, optimize mechanical properties, add different material coatings, and be able to change any of these parameters for no extra manufacturing cost.

The capabilities of LENS have led to it being researched for applications such as making intricate structures, repairing parts, adding hard coating, and more. Being that LENS is an AM process it is expected to be able to make intricate parts. This has been proven in the past and is not a surprise[6]. The real novel research is in the repair and coating research. Past examples of this is LENS has been used to strengthen metal by just running a laser on the surface[16,17]. The laser melts the surface which then solidifies at a high rate, and subsequently strengthens the surface. The deposition ability of LENS makes it so it can fix parts that have experience material loss[18–22].

LENS adds back material just as a welder can deposit feed stock to different areas. This saves companies money by not having to replace parts. In addition to fixing parts, a large area of research has been devoted to using DLD to deposit protective coatings to prevent further damage of components[23–27]. Since the laser can reach very high temperatures, LENS can be used to melt and deposit various refractory metals and ceramics. These two abilities mixed together make it so LENS can be used to not only repair parts, but add a coating to them as well to prevent future damage. To add to that the LENS can also do more than just add a coating to the top of base material. It can mix and bond the coating and bulk material, and add the material back gradually. This results in a compositionally gradient layer that increases adhesion and protection of the coating to the part[6,13,28–31]. LENS has even been used to add protective coatings by bonding the substrate metal with the atmospheres. For example a laser ran over titanium in a nitrogen environment, producing titanium nitride while simultaneously depositing silicon nitride[32]. Though much research has been done, the versatility of DLD means it has the capabilities to do much more.

Though DLD is an advanced AM technique that has had extensive research done on it, it is still a young technology. AM in general is not a mature field, and DLD does not deviate from that[5]. There is still much research to be done on the abilities of LENS in order for it to be fully integrated into manufacturing. For this reason, the projects presented in the paper were conducted. The first one involves making micro-porous titanium structures using the LENS. The next two are focused on making gradient surface coating to repair and protect stainless steel.

1.3 DLD of Micro-Porous Ti6Al4V Filters

Porous metal structures serve an important function in several systems and are required for many applications. They play a significant role in many industries and have been used as filters, scaffolds, flame arrestors, and various other purposes that are difficult to replace with other

materials. Micro porous interconnected metal structures are especially difficult to make and only certain processes can produce such structures [33]. In this study it was hypothesized the LENS was a viable way to make micro porous Ti6Al4V structures by only changing processing parameters. This idea was tested and the results were analyzed for interconnectivity and internal structure.

Important factors must be taken into consideration when making micro-porous structures. Based on the application, features such as size, interconnectivity, shape, consistency, surface area to volume ratio, and more must be controlled. AM is now being looked at to make these difficult structures, as well as new ones that could not be made before [34]. This is due to AM's ability to give more precise control of internal structure, be able to make complex bulk structures, and fabricate structures not possible with conventional manufacturing [35]. LENS processing could possibly be used to make these metal structures with fine interconnected porosity. In this study experimentation was done using LENS to see if it is a viable process for creating micro porous interconnected Ti6Al4V structures.

As mentioned earlier, AM has starting to be adopted in many industries such as the aerospace and medical [22,36–38]. AM has potential to make massive changes in these fields by making designs in one process with no additional tooling required [39,40]. This makes it so parts can cost much less as well as can be made more efficient by optimizing the geometry [41]. In order for AM to make parts in one process it needs to be able to make all types of components, such as a porous and dense parts. Porous metals in the past have been made to be used as filters, flow meters, pressure control, storage reservoirs, flame arrestors, attenuation devices, gas distribution, and media retention [42]. Many parts are housed internally in different systems, and it would be ideal to have these structures built internally, as opposed to adding it later during assembly. This means AM

could add these porous structures internally to parts without having to design for installation or assembly. This is only possible if the process can build the porous structure.

LENS is a viable candidate for making controlled porosity structures. In the past many other processes have been used to make porous metal such as compressing and sintering titanium fibers, compressing and sintering particles, plasma spraying of powder, foaming by expansion of argon filled pores, and polymeric sponge replication [43]. LENS can be used to make porous structure by designing porosity as well as controlling process parameters. Other AM processes have been used in the past to make porous Ti6Al4V such as direct metal laser sintering [44,45], direct laser forming [46,47], select laser melting/select laser sintering [33,48], electron beam melting [49–52], multistage lost wax investment casting [34] and 3D fiber depositing system [43,53]. All these methods have their advantages and disadvantages when compared to each other. Direct metal laser sintering, direct laser forming, and electron beam melting all require a powder bed in order to build parts. This makes it so these processes can produce large overhangs, but powder must be removed after the part is finished. 3D fiber depositing uses a binder and dispersant to hold the metal suspension together before sintering, which is a post processing step. These post processing steps are setbacks when manufacturing and it would be ideal to avoid them. LENS unique capabilities of directly building a part and not requiring a powder bed or binder give it advantages over other AM processes. It also has the ability to modify the material and add secondary materials during the build, which may be needed when optimizing a system [54]

1.4 Deposition of Hard Carbide Coatings for Repair and Protection

As mentioned earlier, laser cladding and repair is a way LENS can be utilized in industries. Vanadium carbide (VC) and Niobium Carbide (NbC) coatings have been used in the past to protect tools from damage, improve mechanical properties, lengthen service life, and increase corrosion

resistance[55–57]. Both carbides are incredibly hard, have high wear resistance, and a high melting temperature[58–60]. In the past both carbides have shown to increase protective properties by being added to steel either as a coating or a metal matrix composite (MMC). For this reason, it has now been looked at to be added to stainless steel to make a gradient coating to repair and add protection to damaged parts.

1.4.0 Abrasive Wear and Cavitation

Figure 1.2: Cavitation erosion marks in a Pelton turbine[61]

In many industries there are service parts that undergo material loss due to wear, erosion, corrosion, cavitation, and more. These damaged parts cost industries a lot to replace and time to repair them. An industry where this is prominent is the hydroelectric. Parts are constantly damaged and broken due to abrasives water flow and cavitation. Cavitation erosion is damage to parts caused by the continual evaporation and collapse of bubbles. These vapor bubbles cause pitting, material loss, and makes the part more susceptible to corrosion[62,63]. **Fig 1.2** shows an image of some common cavitation damage in hydraulic turbines. When this happens it lowers the efficiency of the turbine by changing the hydraulic profile[61]. Likewise abrasives in the water can wear away parts, causing damage and reduction and efficiency[64–66].

1.4.1 Surface Modifications

A way to prevent this damage is surface modification of the turbines and components. One of the main benefits of this method is inexpensive materials can be used for the bulk of the part while only a small portion of expensive ones are used to increase protection[67]. Generally speaking

materials with high hardness and tensile strengths are the most resistant to abrasive water and cavitation damage[68,69]. In the past many hard high modulus materials have been research for coatings to be applied to components for increased resistance[61–63,65,67,70–81]. A common coating used for increased cavitation resistance is tungsten carbide. Transition metal carbides in group IV to VI are generally used as hard phases in many common alloys[82]. Since WC showed potential to increase cavitation and abrasive resistance in steels, this paper explored the use of VC and NbC.

1.4.2 Strengthening Mechanisms

VC and NbC can be used to make a protective coating by using it to strengthen the metal, or be applied as a hard ceramic coating. Both carbides can diffuse into the grains and strengthen the lattice by substitution[83,84]. It can also be added as a precipitate and be dispersed in the steel making the coating a MMC[85]. These precipitates cause internal stress and increase the hardness and strength. This method has been used to enhance metal properties in stainless cast iron and tool steels to increase wear and corrosion resistance[86,87]. The other way is the carbides are deposited on the surface. Both carbides are very hard, stable, and ideal for a protective coating. These are the three ways the carbides can be used to coat and strengthen steel.

1.4.3 Vanadium and Niobium Carbide Coatings

In the past VC, NbC, and other V and Nb compound coatings primarily have been applied using thermal-reactive diffusion(TRD)[56,58,88,89], chemical vapor deposition(CVD)[66,90,91], physical vapor deposition(PVD)[66,90,91], and plasma jet cladding[60,86]. These methods have all proven to make very hard coatings with impressive properties of high hardness and good adhesion. There are some issues though. CVD requires high processing temperatures which can be costly[88]. PVD need expensive equipment and generally results in a weaker coating due to limited diffusion[88]. TRD also is limited by diffusion and only yields coatings with a small depth and limited coating thickness[60]. This means there is very little depth of material that needs to be removed before the

bulk material is exposed and the part is just as vulnerable to damage as it would be without the coating. It would be more ideal to have a coating with a larger depth in order to further protect the part if the initial coating is breached.

1.4.4 Past Research of Laser Processing of Coatings

Laser surface processing has many advantages compared to the other coating techniques. It has a fast processing speed, can give very good metallurgical bond between substrate and coating, is easily automated, parameters can be accurately controlled, can process complex shapes, and depending on material, deposit thick coatings[92]. In the past it has been shown that VC coatings could be applied using Nb:YAG laser[84,85,92,93]. All past research was slightly different in the way they bonded the carbides and used one of the strengthening mechanisms to make a good coating. J. Nurminen from the Technology Centre KETEK used laser cladding to make MMC's of with nickel and steel alloys, but not stainless steel. He compared the wear resistance of different MMC's of WC, VC, and TiC. It was found that of all the steels, the M2 steel with VC had the best abrasive wear resistance[85]. Y. Herrera of Central University of Venezuela deposited pure VC with a Nb:YAG laser on AISI 1045 steel. He proved that VC could be successfully deposited on an α-Fe matrix. It was found that there was good integration, adhesion, and the coating had a hardness of~ 2500-2800HK_{100}[84]. Swapnil Shah of University of Tennessee also deposited VC using a Nb:YAG laser on AISI H13 steel. In this study they tested the oxidation and found VC has a high affinity towards oxygen, making it more susceptible to oxidation above 800˚C. The VC coating did show great resistance to exposure to molten aluminum and was able to protect the steel from chemical attack. Likewise research has been done on depositing NbC this way as well[94]. M. Sansone of Universita della Basilicata deposited thin films of NbC using a Nd:YAG laser. This study was only to show thin films could be made with NbC, material property testing was minimal[94].

1.4.5 Objectives and Novelty of Research

It is now known that abrasive wear and cavitation cause significant damage to hydro turbine parts. This damages results in material loss, lower efficiency, and failure of parts. Currently the most common way to fix cavitation or abrasive water damage is by adding welding filler back to where material was lost[61]. These patches do not considerably improve future cavitation resistance and more maintenance procedure are needed for their maintenance. In the past coatings consisting of MMC's or very hard materials are applied to resist cavitation and abrasive water damage. Though many of these processes can only make a small coating that cannot be added back to damaged parts and if broken will not protect the material any longer. Likewise, these coatings cannot be added back to a damaged part to restore material and fix it. It was hypothesized that LENS would be a viable process to be able to add a functionally gradient coating of VC and NbC mixed with stainless steel. The objective of this research was to make a coating that was first a MMC of VC and NbC that would have higher hardness and wear resistance than the stainless steel substrate. It would then be able to gradually increase carbide content, which would increase hardness and wear resistance, until the coating was 100% carbide. This would make it so the top coating had very abrasive wear resistance, hardness, and modulus. If broken over time though, the material underneath would still provide added protection. LENS could then be used to not only build new parts with these coatings, but fix damaged parts and add extra protection. If successful it could reduce maintenance cost of damaged parts, increase efficiency of hydropower plants, and increase the lifetime of components.

1.5 References

1. Qiu C, Ravi G a., Dance C, Ranson A, Dilworth S, Attallah MM. Fabrication of large Ti–6Al–4V structures by direct laser deposition. *J Alloys Compd*. 2015;629:351-361. doi:10.1016/j.jallcom.2014.12.234.

2. Yu J, Lin X, Wang J, Chen J, Huang W. Applied Surface Science Mechanics and energy analysis on molten pool spreading during laser solid forming. *Appl Surf Sci*. 2010;256(14):4612-4620. doi:10.1016/j.apsusc.2010.02.060.

3. Roy M, Vamsi Krishna B, Bandyopadhyay A, Bose S. Laser processing of bioactive tricalcium phosphate coating on titanium for load-bearing implants. *Acta Biomater*. 2008;4(2):324-333. doi:10.1016/j.actbio.2007.09.008.

4. Wohlers T, Gornet T. History of additive manufacturing Introduction of non-SL systems Introduction of low-cost 3D printers. *Wohlers Rep 2011*. 2011:1-23.

5. Maxwell J. Standards Spur 3D Printing. *ASTM Standardization News*. http://www.astm.org/sn/features/standards-spur-3d-printing-nd15.html.

6. Collins PC, Banerjee R, Banerjee S, Fraser HL. Laser deposition of compositionally graded titanium-vanadium and titanium-molybdenum alloys. *Mater Sci Eng A*. 2003;352(1-2):118-128. doi:10.1016/S0921-5093(02)00909-7.

7. Bandyopadhyay A, Gualtieri T, Bose S. Global Engineering and Additive Manufacturing. In: Bandyopadhyay A, Bose S, eds. *Additive Manufacturing*. Vol 1st ed. CRC Press; 2015.

8. Harbaugh J. Space Station 3-D Printer Builds Ratchet Wrench to Complete First PHase of Operations. *NASA*. http://www.nasa.gov/mission_pages/station/research/news/3Dratchet_wrench.

9. Tampi T. Move Over Titanium, 3D Printed Bone Implants are Here. *3D Printing Industry*. http://3dprintingindustry.com/2015/05/18/move-over-titanium-3d-printed-bone-implants-are-here/.

10. Balla KV, Bose S, Bandyopadhyay A. Low stiffness porous Ti structures for load-bearing implants. *Acta Biomater*. 2007;3(6):997-1006. doi:10.1016/j.actbio.2007.03.008.

11. Xue W, Krishna BV, Bandyopadhyay A, Bose S. Processing and biocompatibility evaluation of laser processed porous titanium. *Acta Biomater*. 2007;3(6):1007-1018. doi:10.1016/j.actbio.2007.05.009.

12. Bandyopadhyay A, Krishna B V., Xue W, Bose S. Application of Laser Engineered Net Shaping (LENS) to manufacture porous and functionally graded structures for load bearing implants. *J Mater Sci Mater Med*. 2009;20(SUPPL. 1):S29-S34. doi:10.1007/s10856-008-3478-2.

13. Balla VK, DeVasConCellos PD, Xue W, Bose S, Bandyopadhyay A. Fabrication of compositionally and structurally graded Ti-TiO2 structures using laser engineered net

shaping (LENS). *Acta Biomater*. 2009;5(5):1831-1837. doi:10.1016/j.actbio.2009.01.011.

14. Samuel S, Nag S, Scharf TW, Banerjee R. Wear resistance of laser-deposited boride reinforced Ti-Nb-Zr-Ta alloy composites for orthopedic implants. *Mater Sci Eng C*. 2008;28(3):414-420. doi:10.1016/j.msec.2007.04.029.

15. Roy M, Balla VK, Bandyopadhyay A, Bose S. MgO-doped tantalum coating on Ti: Microstructural study and biocompatibility evaluation. *ACS Appl Mater Interfaces*. 2012;4(2):577-580.

16. Balla VK, Soderlind J, Bose S, Bandyopadhyay A. Microstructure, mechanical and wear properties of laser surface melted Ti6Al4V alloy. *J Mech Behav Biomed Mater*. 2014;32:335-344. doi:10.1016/j.jmbbm.2013.12.001.

17. Vamsi Krishna B, Bandyopadhyay A. Surface modification of AISI 410 stainless steel using laser engineered net shaping (LENSTM). *Mater Des*. 2009;30(5):1490-1496. doi:10.1016/j.matdes.2008.08.003.

18. Pavlov M, Novichenko D, Doubenskaia M. Optical diagnostics of deposition of metal matrix composites by laser cladding. *Phys Procedia*. 2011;12(PART 1):674-682. doi:10.1016/j.phpro.2011.03.084.

19. Onwubolu GC, Davim JP, Oliveira C, Cardoso a. Prediction of clad angle in laser cladding by powder using response surface methodology and scatter search. *Opt Laser Technol*. 2007;39(6):1130-1134. doi:10.1016/j.optlastec.2006.09.008.

20. Boisselier D, Sankaré S. Influence of Powder Characteristics in Laser Direct Metal Deposition of SS316L for Metallic Parts Manufacturing. *Phys Procedia*. 2012;39:455-463. doi:10.1016/j.phpro.2012.10.061.

21. Xiong Z, Chen GX, Zeng XY. Effects of process variables on interfacial quality of laser cladding on aeroengine blade material GH4133. *J Mater Process Technol*. 2009;209(2):930-936. doi:10.1016/j.jmatprotec.2008.03.004.

22. Sexton L, Lavin S, Byrne G, Kennedy a. Laser cladding of aerospace materials. *J Mater Process Technol*. 2002;122(1):63-68. doi:10.1016/S0924-0136(01)01121-9.

23. Das M, Balla VK, Basu D, Manna I, Sampath Kumar TS, Bandyopadhyay A. Laser processing of in situ synthesized TiB-TiN-reinforced Ti6Al4V alloy coatings. *Scr Mater*. 2012;66(8):578-581. doi:10.1016/j.scriptamat.2012.01.010.

24. Karthik D, Kalainathan S, Swaroop S. Surface modification of 17-4 PH stainless steel by laser peening without protective coating process. *Surf Coatings Technol*. 2015;278:138-145. doi:10.1016/j.surfcoat.2015.08.012.

25. Pang W, Man HC, Yue TM. Laser surface coating of Mo–WC metal matrix composite on Ti6Al4V alloy. *Mater Sci Eng A*. 2005;390(1-2):144-153. doi:10.1016/j.msea.2004.07.065.

26. del Val J, Comesaña R, Lusquiños F, et al. Laser cladding of Co-based superalloy coatings: Comparative study between Nd:YAG laser and fibre laser. *Surf Coatings Technol*. 2010;204(12-13):1957-1961. doi:10.1016/j.surfcoat.2009.11.036.

27. Das M, Bysakh S, Basu D, et al. Microstructure, mechanical and wear properties of laser processed SiC particle reinforced coatings on titanium. *Surf Coatings Technol*. 2011;205(19):4366-4373. doi:10.1016/j.surfcoat.2011.03.027.

28. Man HC, Zhang S, Cheng FT, Guo X. In situ formation of a TiN/Ti metal matrix composite gradient coating on NiTi by laser cladding and nitriding. *Surf Coatings Technol*. 2006;200(16-17):4961-4966. doi:10.1016/j.surfcoat.2005.05.017.

29. Zheng M, Fan D, Li XK, Li WF, Liu Q Bin, Zhang J Bin. Microstructure and osteoblast response of gradient bioceramic coating on titanium alloy fabricated by laser cladding. *Appl Surf Sci*. 2008;255(2):426-428. doi:10.1016/j.apsusc.2008.06.078.

30. Roy M, Balla VK, Bandyopadhyay A, Bose S. Compositionally graded hydroxyapatite/tricalcium phosphate coating on Ti by laser and induction plasma. *Acta Biomater*. 2011;7(2):866-873. doi:10.1016/j.actbio.2010.09.016.

31. Kruth J-P, Leu MC, Nakagawa T. Progress in Additive Manufacturing and Rapid Prototyping. *CIRP Ann - Manuf Technol*. 1998;47(2):525-540. doi:10.1016/S0007-8506(07)63240-5.

32. Zhang Y, Sahasrabudhe H, Bandyopadhyay A. Additive manufacturing of Ti-Si-N ceramic coatings on titanium. *Appl Surf Sci*. 2015;346:428-437. doi:10.1016/j.apsusc.2015.03.184.

33. Van Der Stok J, Van Der Jagt OP, Amin Yavari S, et al. Selective laser melting-produced porous titanium scaffolds regenerate bone in critical size cortical bone defects. *J Orthop Res*. 2013;31(5):792-799. doi:10.1002/jor.22293.

34. Ryan GE, Pandit AS, Apatsidis DP. Porous titanium scaffolds fabricated using a rapid prototyping and powder metallurgy technique. *Biomaterials*. 2008;29(27):3625-3635. doi:10.1016/j.biomaterials.2008.05.032.

35. Conner BP, Manogharan GP, Martof AN, et al. Making sense of 3-D printing: Creating a map of additive manufacturing products and services. *Addit Manuf*. 2014;1-4:64-76. doi:10.1016/j.addma.2014.08.005.

36. Brookes KJ a. PM AM at Farnborough. *Met Powder Rep*. 2014;69(6):34-35. doi:10.1016/S0026-0657(14)70277-2.

37. Truscott M, Booysen G, De Beer D. Rapid Prototyping and manufacturing in medical product development. *3rd Int Conf Addit Technol DAAAM Spec Conf*. 2010;21(1):1-2.

38. Wauthle R, Vrancken B, Beynaerts B, et al. Effects of build orientation and heat treatment on the microstructure and mechanical properties of selective laser melted Ti6Al4V lattice structures. *Addit Manuf*. 2015;5:77-84. doi:10.1016/j.addma.2014.12.008.

39. Emmelmann C, Sander P, Kranz J, Wycisk E. Laser additive manufacturing and bionics: Redefining lightweight design. *Phys Procedia*. 2011;12(PART 1):364-368. doi:10.1016/j.phpro.2011.03.046.

40. Buchbinder D, Schleifenbaum H, Heidrich S, Meiners W, Bültmann J. High power Selective Laser Melting (HP SLM) of aluminum parts. *Phys Procedia*. 2011;12(PART 1):271-278. doi:10.1016/j.phpro.2011.03.035.

41. Lyons B. Additive Manufacturing in Aerospace: Examples and Research Outlook. In: *Frontiers of Engineering 2011: Reports on Leading-Edge Engineering from the 2011 Symposium*. Vol ; 2012:15-24.

42. Federation MPI. Porous Metal Design Guidebook. www.mpif.org.

43. Li JP, De Wijn JR, Van Blitterswijk C a., De Groot K. Porous Ti6Al4V scaffold directly fabricating by rapid prototyping: Preparation and in vitro experiment. *Biomaterials*. 2006;27(8):1223-1235. doi:10.1016/j.biomaterials.2005.08.033.

44. Khaing MW, Fuh JYH, Lu L. Direct metal laser sintering for rapid tooling: Processing and characterisation of EOS parts. *J Mater Process Technol*. 2001;113(1-3):269-272. doi:10.1016/S0924-0136(01)00584-2.

45. Traini T, Mangano C, Sammons RL, Mangano F, Macchi a., Piattelli a. Direct laser metal sintering as a new approach to fabrication of an isoelastic functionally graded material for manufacture of porous titanium dental implants. *Dent Mater*. 2008;24(11):1525-1533. doi:10.1016/j.dental.2008.03.029.

46. Harrysson OL a., Cansizoglu O, Marcellin-Little DJ, Cormier DR, West H a. Direct metal fabrication of titanium implants with tailored materials and mechanical properties using electron beam melting technology. *Mater Sci Eng C*. 2008;28(3):366-373. doi:10.1016/j.msec.2007.04.022.

47. Hollander D a., Von Walter M, Wirtz T, et al. Structural, mechanical and in vitro characterization of individually structured Ti-6Al-4V produced by direct laser forming. *Biomaterials*. 2006;27(7):955-963. doi:10.1016/j.biomaterials.2005.07.041.

48. Yadroitsev I, Shishkovsky I, Bertrand P, Smurov I. Manufacturing of fine-structured 3D porous filter elements by selective laser melting. *Appl Surf Sci*. 2009;255(10):5523-5527. doi:10.1016/j.apsusc.2008.07.154.

49. Parthasarathy J, Starly B, Raman S, Christensen A. Mechanical evaluation of porous titanium (Ti6Al4V) structures with electron beam melting (EBM). *J Mech Behav Biomed Mater*. 2010;3(3):249-259. doi:10.1016/j.jmbbm.2009.10.006.

50. Cheng XY, Li SJ, Murr LE, et al. Compression deformation behavior of Ti–6Al–4V alloy with cellular structures fabricated by electron beam melting. *J Mech Behav Biomed Mater*. 2012;16:153-162. doi:10.1016/j.jmbbm.2012.10.005.

51. Heinl P, Rottmair a., Körner C, Singer RF. Cellular Titanium by Selective Electron Beam Melting. *Adv Eng Mater*. 2007;9(5):360-364. doi:10.1002/adem.200700025.

52. de Peppo GM, Palmquist a., Borchardt P, et al. Free-Form-Fabricated Commercially Pure Ti and Ti6Al4V Porous Scaffolds Support the Growth of Human Embryonic Stem Cell-Derived Mesodermal Progenitors. *Sci World J*. 2012;2012:1-14. doi:10.1100/2012/646417.

53. Li JP, Habibovic P, van den Doel M, et al. Bone ingrowth in porous titanium implants produced by 3D fiber deposition. *Biomaterials*. 2007;28(18):2810-2820. doi:10.1016/j.biomaterials.2007.02.020.

54. Sahasrabudhe H, Harrison R, Carpenter C, Bandyopadhyay A. Stainless steel to titanium

bimetallic structure using LENS^{TM}. *Addit Manuf*. 2015;5:1-8. doi:10.1016/j.addma.2014.10.002.

55. Li Q, Lei Y, Fu H. Surface & Coatings Technology Laser cladding in-situ NbC particle reinforced Fe-based composite coatings with rare earth oxide addition. *Surf Coat Technol*. 2014;239:102-107. doi:10.1016/j.surfcoat.2013.11.026.

56. Orjuelag A, Rincón R, Jairo J. Surface & Coatings Technology Corrosion resistance of niobium carbide coatings produced on AISI 1045 steel via thermo-reactive diffusion deposition. *Surf Coat Technol*. 2014;259:667-675. doi:10.1016/j.surfcoat.2014.10.012.

57. Medeiros FFP, Da Silva a. GP, De Souza CP. Synthesis of niobium carbide at low temperature and its use in hardmetal. *Powder Technol*. 2002;126(2):155-160. doi:10.1016/S0032-5910(02)00042-6.

58. Chicco B, Borbidge W., Summerville E. Experimental study of vanadium carbide and carbonitride coatings. *Mater Sci Eng A*. 1999;266(1-2):62-72. doi:10.1016/S0921-5093(99)00035-0.

59. Liu H, Zhu J, Liu Y, Lai Z. First-principles study on the mechanical properties of vanadium carbides VC and V4C3. *Mater Lett*. 2008;62:3084-3086. doi:10.1016/j.matlet.2008.01.136.

60. Cai X, Xu Y, Zhong L, Zhao N, Yan Y. Kinetics of niobium carbide reinforced composite coating produced in situ. *Vaccum*. 2015;119:239-244. doi:10.1016/j.vacuum.2015.05.035.

61. Santa JF, Blanco JA, Giraldo JE, Toro A. Cavitation erosion of martensitic and austenitic stainless steel welded coatings. *Wear*. 2011;271(9-10):1445-1453. doi:10.1016/j.wear.2010.12.081.

62. Jafarzadeh K, Valefi Z, Ghavidel B. The effect of plasma spray parameters on the cavitation erosion of Al2O3-TiO2 coatings. *Surf Coatings Technol*. 2010;205(7):1850-1855. doi:10.1016/j.surfcoat.2010.08.044.

63. Hong S, Wu Y, Zhang J, Zheng Y, Qin Y, Lin J. Ultrasonics Sonochemistry Effect of ultrasonic cavitation erosion on corrosion behavior of high-velocity oxygen-fuel (HVOF) sprayed near-nanostructured WC – 10Co – 4Cr coating. *Ultrason Sonochem*. 2015;27:374-378. doi:10.1016/j.ultsonch.2015.06.006.

64. Kumar P, Saini RP. Study of cavitation in hydro turbines-A review. *Renew Sustain Energy Rev*. 2010;14(1):374-383. doi:10.1016/j.rser.2009.07.024.

65. Ruizhu Z. Mechanical Properties of WC-8Co Wear- Resistant Coating on Pump Impellers Surface by Electro- Spark. *Rare Met Mater Eng*. 2015;44(7):1587-1590. doi:10.1016/S1875-5372(15)30097-7.

66. Makuch N, Piasecki A, Dziarski P, Kulka M. Technology In fluence of laser alloying with boron and niobium on microstructure and properties of Nimonic 80A-alloy. *Opt Laser Technol*. 2015;75:229-239. doi:10.1016/j.optlastec.2015.07.015.

67. Lo KH, Cheng FT, Kwok CT, Man HC. Improvement of cavitation erosion resistance of AISI 316 stainless steel by laser surface alloying using fine WC powder. *Surf Coatings Technol*. 2003;165(3):258-267.

68. Plesset BYMS, Ellis AT. On the mechanism of cavitation in centrifugal pumps. *Wear*. 1958;1(4):353. doi:10.1016/0043-1648(58)90042-5.

69. Qiu N, Wang L, Wu S, Likhachev DS. Research on cavitation erosion and wear resistance performance of coatings. *Eng Fail Anal*. 2015;55:208-223. doi:10.1016/j.engfailanal.2015.06.003.

70. Hou G, Zhao X, Zhou H, et al. Cavitation erosion of several oxy-fuel sprayed coatings tested in deionized water and artificial seawater. *Wear*. 2014;311(1-2):81-92. doi:10.1016/j.wear.2013.12.026.

71. Deplancke T, Lame O, Cavaille J, Fivel M, Riondet M, Franc J. Outstanding cavitation erosion resistance of Ultra High Molecular Weight Polyethylene (UHMWPE) coatings. *Wear*. 2015;328-329:301-308. doi:10.1016/j.wear.2015.01.077.

72. Krella A, Czyzniewski A. Cavitation erosion resistance of Cr-N coating deposited on stainless steel. *Wear*. 2006;260(11-12):1324-1332. doi:10.1016/j.wear.2005.09.018.

73. Krella A, Czyzniewski A. Cavitation resistance of Cr-N coatings deposited on austenitic stainless steel at various temperatures. *Wear*. 2009;266(7-8):800-809. doi:10.1016/j.wear.2008.11.002.

74. Krella A, Czyzniewski A. Cavitation erosion resistance of nanocrystalline TiN coating deposited on stainless steel. *Wear*. 2008;265(7-8):963-970. doi:10.1016/j.wear.2008.02.004.

75. Belous V, Vasyliev V, Luchaninov A, et al. Cavitation and abrasion resistance of Ti-Al-Y-N coatings prepared by the PIII&D technique from filtered vacuum-arc plasma. *Surf Coatings Technol*. 2013;223:68-74. doi:10.1016/j.surfcoat.2013.02.031.

76. Bitzer M, Rauhut N, Mauer G, et al. Cavitation-resistant NiTi coatings produced by low-pressure plasma spraying (LPPS). *Wear*. 2015;328-329:369-377. doi:10.1016/j.wear.2015.03.003.

77. Hattori S, Komoriya I, Kawasaki S, Kono S. Cavitation erosion of silver plated coatings in a low-temperature environment. *Wear*. 2012;292-293:74-81. doi:10.1016/j.wear.2012.05.031.

78. Cheng F, Jiang S, Liang J. Cavitation erosion resistance of microarc oxidation coating on aluminium alloy. *Appl Surf Sci*. 2013;280:287-296. doi:10.1016/j.apsusc.2013.04.151.

79. Zheng ZB, Zheng YG, Sun WH, Wang JQ. Tribology International Effect of heat treatment on the structure , cavitation erosion and erosion – corrosion behavior of Fe-based amorphous coatings. *Tribiology Int*. 2015;90:393-403. doi:10.1016/j.triboint.2015.04.039.

80. Kim S-J, Lee S-J, Kim I-J, Kim S-K, Han M-S, Jang S-K. Cavitation and electrochemical characteristics of thermal spray coating with sealing material. *Trans Nonferrous Met Soc China*. 2013;23(4):1002-1010. doi:10.1016/S1003-6326(13)62559-5.

81. Coddet P, Verdy C, Coddet C, Debray F, Lecouturier F. Surface & Coatings Technology Mechanical properties of thick 304L stainless steel deposits processed by He cold spray. *Surf Coat Technol*. 2015;277:74-80. doi:10.1016/j.surfcoat.2015.07.001.

82. Woydt M, Mohrbacher H, Vleugels J, Huang S. Niobium carbide for wear protection – tailoring its properties by processing and stoichiometry. *Met Powder Rep*. 2016;00(00). doi:10.1016/j.mprp.2015.12.010.

83. Park D, Huh M, Jung W, Suh J, Shim J, Lee S. Effect of vanadium addition on the creep resistance of 18Cr9Ni3CuNbN austenitic stainless heat resistant steel. *J Alloys Compd*. 2013;574:532-538. doi:10.1016/j.jallcom.2013.05.106.

84. Herrera Y, Grigorescu I., Ramirez J, Di Rauso C, Staia M. Microstructural characterization of vanadium carbide laser clad coatings. *Surf Coatings Technol*. 1998;108-109:308-311. doi:10.1016/S0257-8972(98)00662-8.

85. Nurminen J, Näkki J, Vuoristo P. Microstructure and properties of hard and wear resistant MMC coatings deposited by laser cladding. *Int J Refract Met Hard Mater*. 2009;27(2):472-478. doi:10.1016/j.ijrmhm.2008.10.008.

86. Hoshiyama Y, Miyazaki T, Miyake H. Rapidly solidified thick stainless cast iron alloy deposit with niobium carbide particles produced by plasma spraying. *Surf Coatings Technol*. 2011;205(SUPPL. 2):S374-S377. doi:10.1016/j.surfcoat.2011.03.114.

87. Uematsu Y, Kakiuchi T, Tokaji K, Nishigaki K, Ogasawara M. Materials Science & Engineering A Effects of shot peening on fatigue behavior in high speed steel and cast iron with spheroidal vanadium carbides dispersed within martensitic-matrix microstructure. *Mater Sci Eng A*. 2013;561:386-393. doi:10.1016/j.msea.2012.10.045.

88. Aghaie-Khafri M, Fazlalipour F. Vanadium carbide coatings on die steel deposited by the thermo-reactive diffusion technique. *J Phys Chem Solids*. 2008;69(10):2465-2470. doi:10.1016/j.jpcs.2008.04.040.

89. Sen U, Pazarlıoglu SS, Sen S. Niobium boride coating on AISI M2 steel by boro-niobizing treatment. *Mater Lett*. 2008;62(16):2444-2446. doi:10.1016/j.matlet.2007.12.042.

90. Aghaie-Khafri M, Fazlalipour F. Kinetics of V(N,C) coating produced by a duplex surface treatment. *Surf Coatings Technol*. 2008;202:4107-4113. doi:10.1016/j.surfcoat.2008.02.027.

91. Sen U. Kinetics of niobium carbide coating produced on AISI 1040 steel by thermo-reactive deposition technique. *Mater Chem Phys*. 2004;86(1):189-194. doi:10.1016/j.matchemphys.2004.03.002.

92. Shah S V, Dahotre NB. Laser surface-engineered vanadium carbide coating for extended die life. *J Mater Process Technol*. 2002;124(1-2):105-112. doi:10.1016/S0924-0136(02)00109-7.

93. Teghil R, De Bonis A, Galasso A, et al. Nanostructured thin films obtained by ultra-short pulse laser deposition of vanadium carbide. *Appl Surf Sci*. 2009;255:5220-5223. doi:10.1016/j.apsusc.2008.07.135.

94. Sansone M, Bonis A De, Santagata A, Rau J V, Galasso A, Teghil R. Pulsed laser ablation and deposition of niobium carbide. *Appl Surf Sci*. 2015. doi:10.1016/j.apsusc.2015.10.056.

CHAPTER TWO

MICRO-POROUS TI6AL4V FILTERS

2.1 Introduction

Porous metal filters are an important part of many systems and also a rather difficult structure to manufacture. They are used as flame arrestors, scaffolds, filters, flow control devises, and many other applications. It is especially difficult to make these structures with interconnected porosity. In many of these application the structure needs to have proper size, interconnectivity, shape, consistency, surface area to volume ratio, and more. AM processes are now being researched with to see if they can make these complex structures. In the present study LENS was examined to see if micro-porous Ti6Al4V structures could be made consistently and with interconnectivity.

2.2 Materials and Methods

2.2.0 LENS Processing of Porous Ti6Al4V Structures

Porous Filters were made using LENS 750 (Optomec Inc., Albuquerque, NM). Description of how LENS works in the first chapter (pg. 2). Ti6Al4V powder (ATI Powder Metals, Pittsburgh, PA) with a powder size of -100/+325 mesh was deposited under the laser from a hopper via argon transport. All samples were built using only Ti6Al4V on a Ti6Al4V plate.

2.2.1 Designing Parameters for Porous Structure

Processing parameters were first chosen based on past work done on LENS[1,2]. Other AM methods have previously used designed porous structure made in a CAD file to build there scaffolds [3–7]. This was considered before building the samples for this study. Due to past knowledge of how the LENS runs it was decided to try and control porosity by only changing the build parameters. By doing this it would mean the user would not have to make a designed porosity

in the CAD file, but only have to change build parameters in a certain location to make a porous structure with known properties. Testing was done by first researching how porous structure were built in the past. Each sample had either the powder feed rate, scan speed, hatch distance, angle of hatch layer, or slice distance adjusted based on the previous builds results. Due to so many parameters and a large range of values for each, not all combinations could be tested. First 10 samples were built, all having different build parameters. Based on the results from that, parameters were refined and 10 more samples were made. Out of those 10 samples, the parameters for the parts with the finest porosity and build quality are shown. Build quality is the part having no visible or unwanted defects.

2.3 Analysis

2.3.0 SEM Analysis of Pores and Microstructure

The microstructure and apparent pore size was observed using a field emission scanning The microstructure and apparent pore size was observed using a field emission scanning electron microscope (FEI Quanta 200) (FEI Inc., OR, USA). The samples were all first ground and polished until they had a mirror surface. This was done starting with 200 grit SiC and successively using higher grits, ending at 1200. Polishing was done using 1µm, 0.3µm, and 0.05µm alumina suspensions on a velvet cloth wheel. First the samples were looked at under the SEM so pore size could be estimated visually. The samples were then removed and etched using Kroll's Reagent (2ml hydrofluoric acid, 6ml nitric acid, 92ml DI water). The etched samples were then viewed again in SEM to observer the microstructure.

2.3.1 Pore Shape and Interconnectivity Test

Proof of pore interconnectivity was done by physical testing as well as running micro CT scans. The physical testing was done by observing if air would pass though the samples. An apparatus

was made that clamped the sample cylinders down and did not let air pass around the sides. This can be seen in **Fig 2.1**. One side had an opening where an air compressor hose was inserted. The other side was open to the environment. The apparatus was immersed in a water tank where a camera was set up in front of it. Air was then let in on the one side of the sample from an air compressor. If bubbles released from the sample, it proved there was interconnectivity. Next the apparent porosity of the samples were calculated using the Archimedes method [8]. From this the density of the sample was calculated to compare with the density of standard Ti6Al4V to show accuracy of pore calculation.

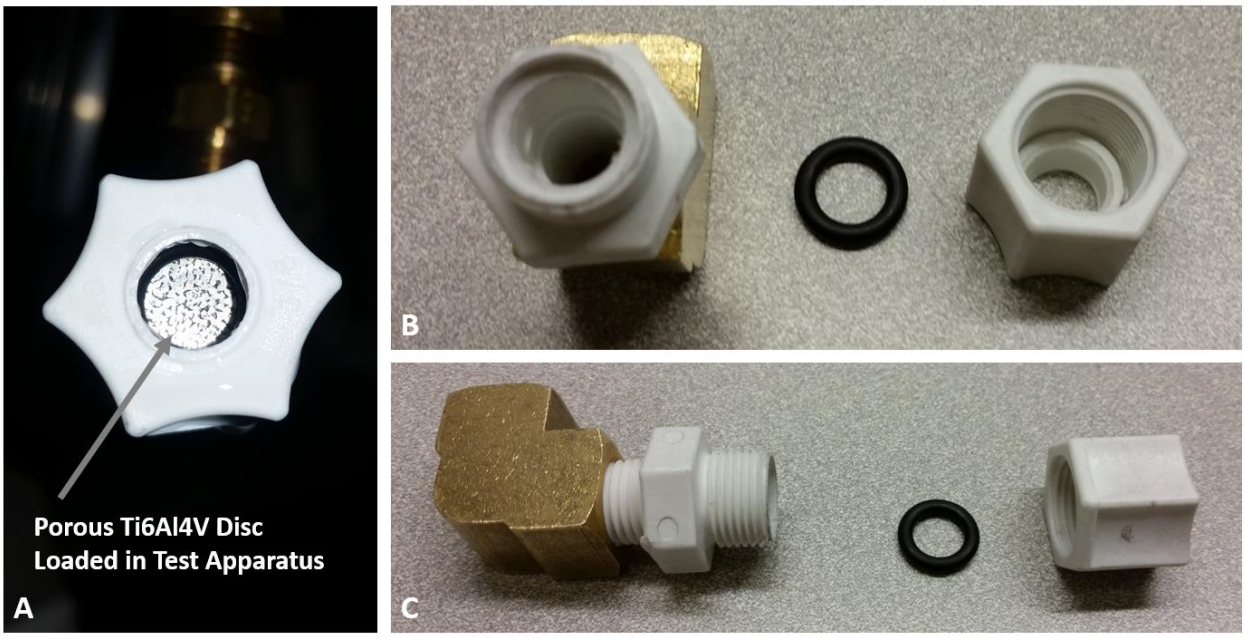

Figure 2.1: Image of interconnected porosity test apparatus. A) Apparatus loaded with a porous Ti6Al4V disc before testing. B) Front view of test apparatus. C) Side view of test apparatus.

2.3.2 Compressive Strength Test

Compression tests were conducted on samples built using the parameters that produced the lowest porosity. Three cylinders were built to be 7mm by 14mm to try and achieve 2:1 diameter

to height ratio. Test were conducted on a screw-driven universal testing machine (AG-IS, Shimadzu, Japan). A stroke rate of 0.5 mm/min was used. The samples were pressed until they fractured. The stress-strain was then plotted and ultimate compressive strength determined.

2.4 Results

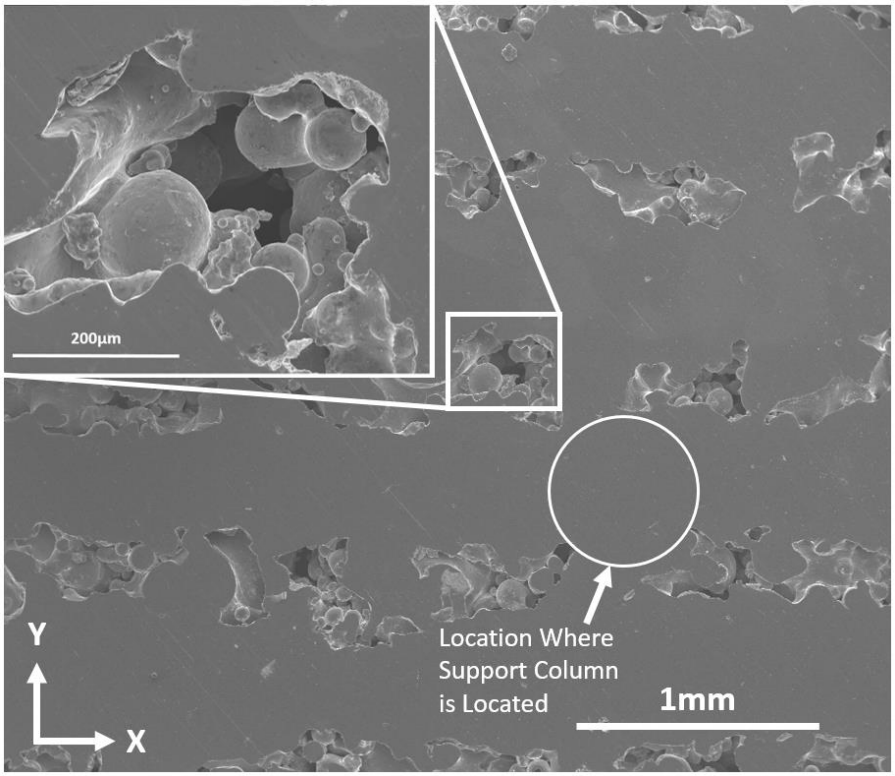

Figure 2.2: LENS processed Ti6Al4V porous structure, sample 2 from table 1. The Z direction, which is the build direction, is normal to the image.

2.4.0 Parameters and Properties

When building the scaffolds, it was found that best way to build the porous structures was by using a low laser power and slow scan speed. Parameters and porosity calculations can be seen in **Table 2.1**. The parameters listed are from the final build and samples that exhibited the lowest porosity. Sample 2 resulted in the lowest calculated porosity and images of it can be seen in **Fig**

2.2, Fig 2.3, and Fig 2.4. Porosity calculations of sample 2 can be seen in Table 1. It was found that it had a porosity of 15.4% with pore interconnectivity.

Table 2.1: Processing Parameters for Ti6Al4V Structure†							
Number	Hatch (in)	Angle (°)	Slice (in)	PF* Rate	Laser (Amp)	Porosity (%)	Density (g/cm^3)
1	0.03	[0/90]	0.01	17.9	31	15.78	4.40
2	0.03	[0/90]	0.01	17.9	31	15.38	4.46
3	0.03	[0/120/240]	0.015	17.9	31	17.25	4.37
4	0.025	[0/120/240]	0.005	11.5	31	21.51	4.36
5	0.025	[0/90]	0.005	11.5	31	17.04	4.40
†All samples proved to have interconnected porosity					Avg.	17.39	4.40
*Powder Feed Rate (g/min)					STD	2.18	0.03

The average porosity of the final samples was 17.4% with the highest porosity sample being 21.5%. It should be noted that earlier builds produced samples with much large apparent porosity that are not listed in the table. Using the weight measurements used to calculate the porosity, the density of the metal was calculated. It came out to be 4.40g/cm^3 ±0.03 which is what past research has also found Ti6Al4V to be [9,10]. This verifies the calculations accuracy and that most all pores are open. If there was closed porosity the buoyancy of the internal channels would cause the density calculation to have variation [11].

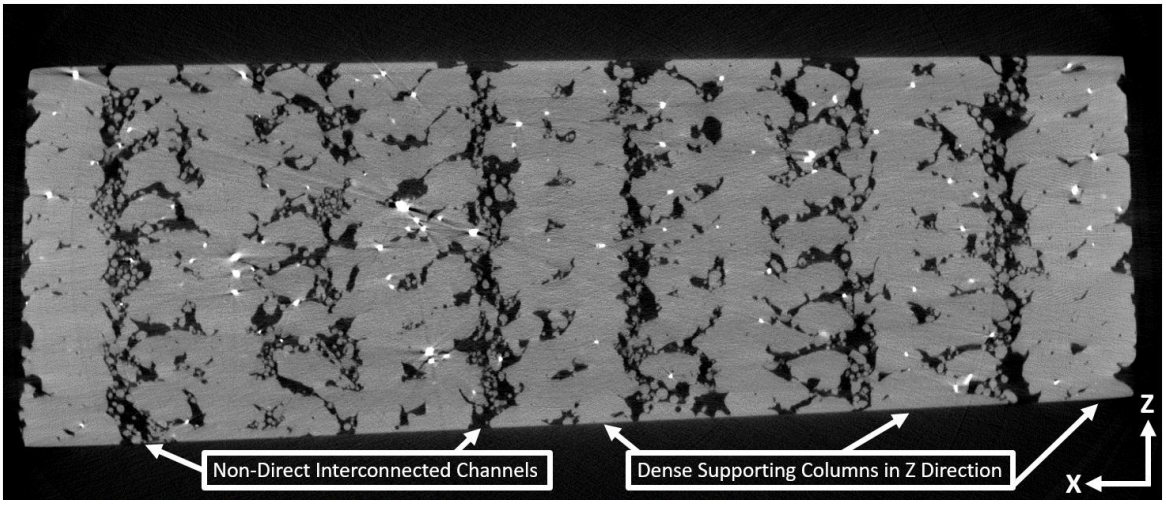

Figure 2.3: LENS processed Ti6Al4V µCT image of internal porous structure.

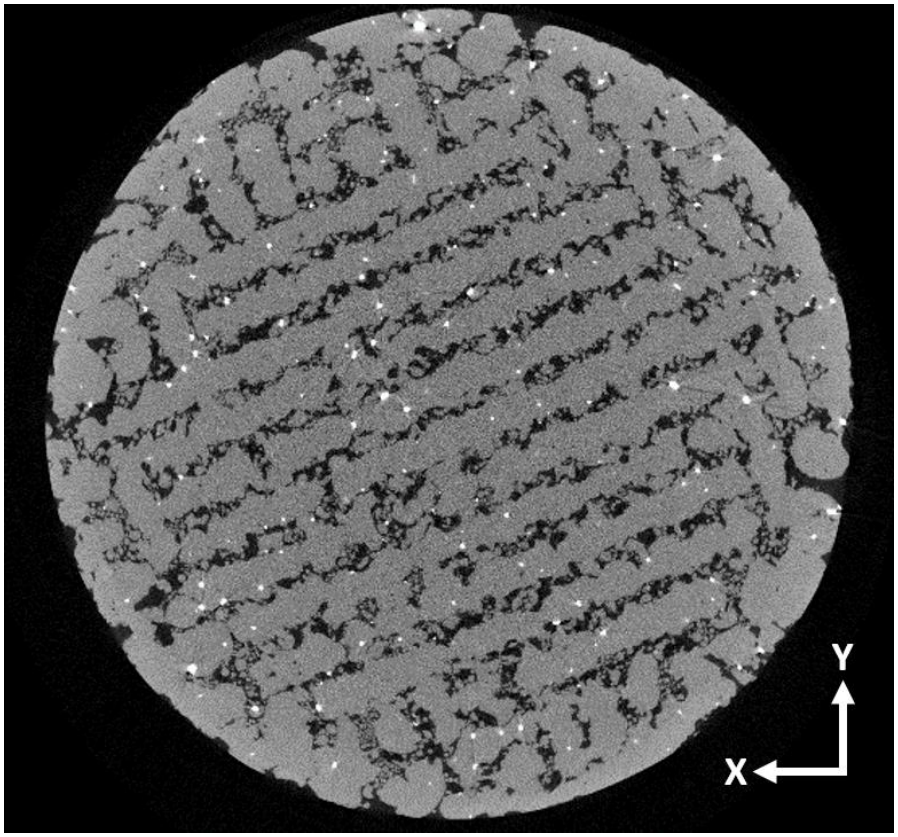

Figure 2.4: LENS processed Ti6Al4V µCT image of top surface of porous structure.

2.4.1 Pore Shape, Size, and Morphology

Fig 2.3 shows and image of the polished top section of sample 2 from the table. It can be seen that there are pore openings in linear patterns going across the sample in the x direction. Within the larger pores there are spherical shaped structures randomly oriented. These can also be seen in **Fig 2.5**. These structures are partially sintered Ti6Al4V. One advantage of free form laser based AM processes is there is no stress being applied to the build such as in molding processes. No mechanical force being applied to powder based parts has been known to lead to porosity [12]. The metal is in powder form when deposited under the laser. The low laser powder does not fully melt the powder as fast as higher powers. Then as a hatch is being built, a melt pool forms and grows. It grows larger the longer the laser is at that location. By having a slow scan speed, the melt pool

has time to grow and fully melt in the center. At a certain width the powder is being deposited on top of the hatch, slightly above the focal point of the laser, as well as on the sides of the hatch. Due to it not being directly under the laser, and the laser power being relatively low, the powder only partially sinters on the sides. This leaves the spherical structure seen in between the larger pores in **Fig 2.3**.

The larger pores are in a linear pattern due to the formation between the hatches. Each dense area is where a scan of the laser was making a hatch. The pore shape looks random across each pore. The pores in between the hatches are not continuous and are broken in intervals. This is due to the [0/90]˚ build orientation. This makes the pores form into a pattern, but each pore has a random shape, and filled partially with sintered powder. It should also be noted the areas between pores appear to have no porosity and are fully dense.

This pattern can also be seen in **Fig 2.4** which is a micro CT scan of the cross section of sample 2. There was column like structures that appeared to be fully dense in the direction of the build. In between them were layers in the horizontal direction that were fully dense. Within the open areas between them, there were small spots of material in spherical shapes. The large columns areas were places the hatches crossed when being built in the [0/90]˚ configuration. The layered areas were spots that only the hatch going in either the 0˚ or 90˚ direction was heading. In between all these hatches were the partially sintered Ti6Al4V. It also appears that the outside is almost fully dense, but may have some voids allowing for gas transfer.

2.4.2 Microstructure

Microstructural images can be seen in **Fig 2.5** of Ti6Al4V porous structures. The grain structure consists of homogeneous acicular grains that are quasi-directional in certain areas. This is due to epitaxial growth of grains while the part is being built layer-by-layer [13]. The needle like

grains are acicular α′ (HCP) grains [7,14]. This is typical of LENS processed Ti6Al4V due to fast cooling rates. The areas where the acicular grains are oriented in the same direction is where β (BCC) grains existed [7]. When the metal first begins to solidify, it forms the β phase, which then begins to transform to the α phase upon further cooling [7,13]. The fast cooling does not allow for a full transition to the α′ phase due to no time for the V atoms to diffuse out of the β structure [7,15]. This results in a martensitic type structure with fine α′ plates [10,13]. Then as the alloy cooled rapidly the acicular α grains developed. Some areas, such as in Fig 6, are random oriented martensitic type acicular grains.

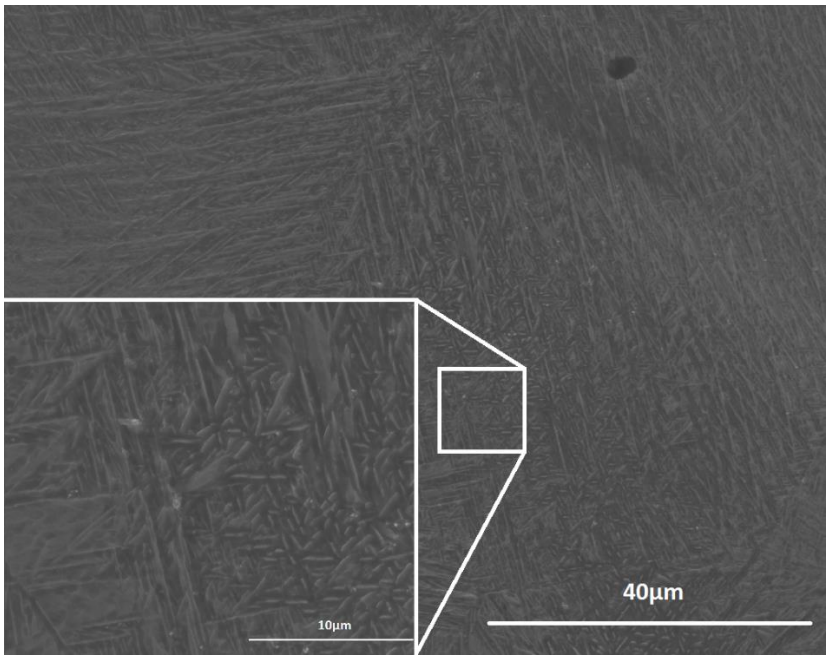

Figure 2.5: Image of LENS processed Ti6Al4V microstructure, 2500x and 10000x magnification

2.4.5 Compression Testing

When building the samples for testing, the parameters for sample 2 from **Table 2.1** were used because it produced the lowest porosity. Ideally this would produce samples with the exact same porosities. This did not prove to be the case and it was found that there was some variability in the

measured porosities. Out of five cylinders built using the same parameters, the porosity ranged from 15.9% to 21.9%, with an average porosity of 19.3% and standard deviation of 2.0%. Table 2 shows the different porosities of the samples built for compression testing. The samples were all built using a STL file of a cylinder that was 7mm diameter and 14mm tall. Due to the large hatches and contours of the build, the cylinder's dimensions on average were 9.5mm diameter and 15.9mm tall. Therefore, the ratio of height to diameter on average was 1.7, slightly less than 2:1.

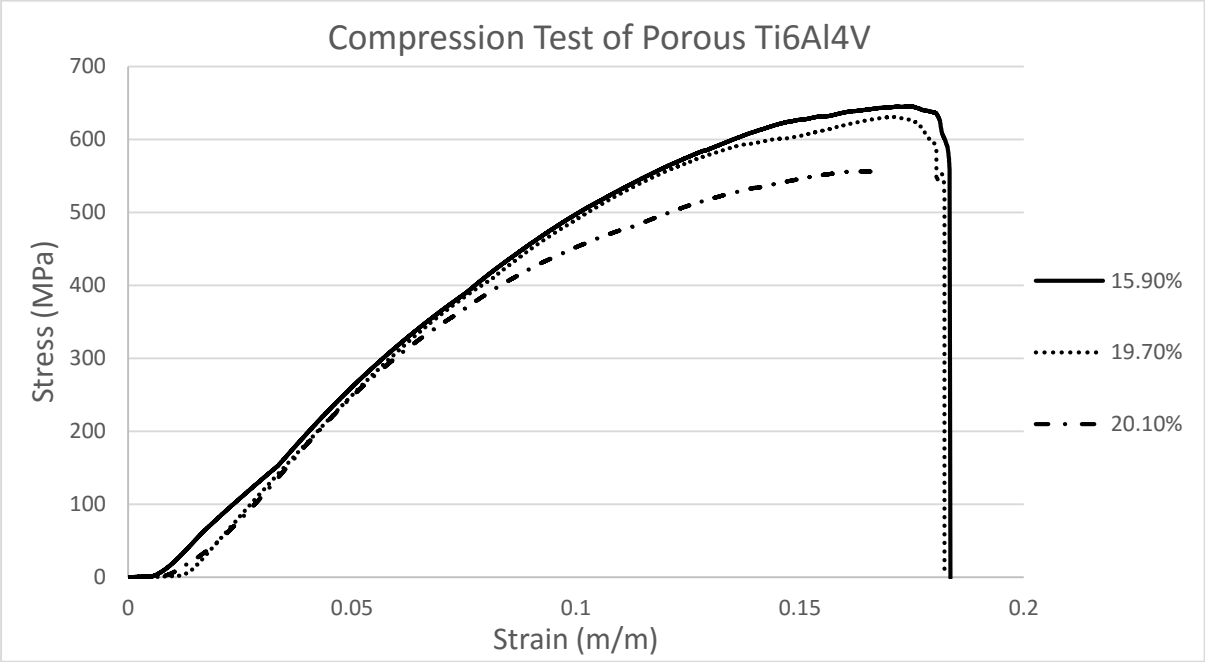

Figure 2.6: Stress-Strain plot of compression test of porous Ti6Al4V cylinders. Though processed using the same parameters, different porosities were measured for each sample. The respective porosities of each compression test is listed on the plot.

Fig 2.6 shows the stress strain plot from the compression tests. Only three test were done in order to preserve 2 of the samples. It can be seen they all follow a similar trend of starting linear, then as the pores start to collapse, the slope gradually decreases. This continues until the ultimate compressive strength is reached, and the porous structure catastrophically fractures 45° to the axial direction. This is common for metals because they fail in shear, which is 45° to the axial directions

when loaded in the axial direction [16]. **Fig 2.7** shows an images of the 19.3% sample before and after testing. It also shows an image of the samples after compressive testing. It can be seen that the 15.9% and 19.3% sample both fractured in the 45° direction. **Fig 2.8** is an image of the fracture surfaces of the 15.9% porous sample. There is clear signs of shearing and plastic deformation that resulted in a planar fracture 45° to the axial direction. Globules of the partially sintered powder can be seen distributed across the fracture surface. Surrounding them are planer surfaces that were the supporting structure that have plastically deformed and failed in the 45° direction.

Table 2.2

Porous Ti6Al4V Compression Test*			
Porosity		Ultimate Compressive Strength (MPa)	
15.90%		645.4	
18.70%		N/A	
19.70%		631	
20.10%		556.4	
21.90%		N/A	
Avg.	19.30%	Avg.	610.9
STD	2.00%	STD	47.8

*Samples ultimate compressive strength listed as N/A means compression tests were not conducted on them.

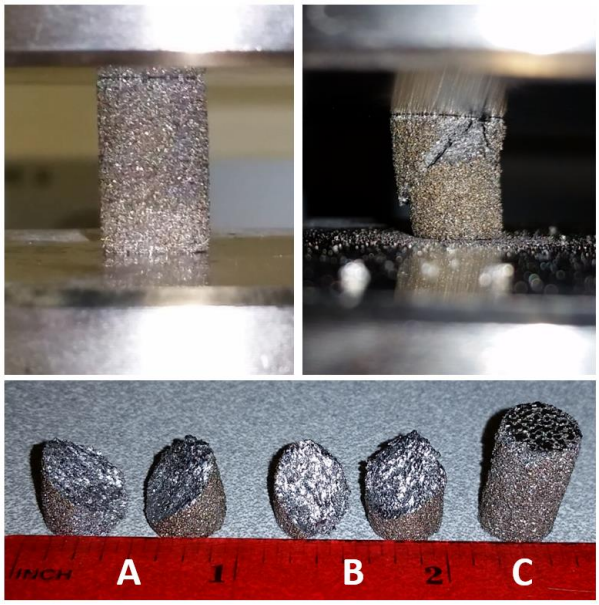

Figure 2.7: Top Left: 19.7% sample loaded for compression test. Top Right: 19.7% porous structure fractured at 45°. Bottom: Samples after compression test: A: 15.9%, B: 19.7%, C: 20.1%.

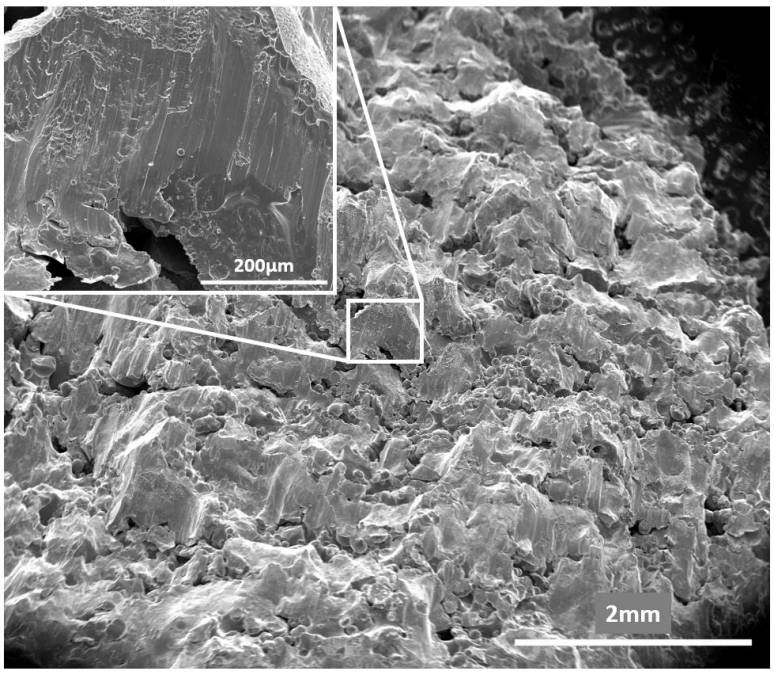

Figure 2.8: Fracture surface of 15.8% porous sample. Cylinder axial direction is normal to the image.

The 15.9% and 19.7% samples have curves that continue all the way until no load is present. The 20.1% curve however stops as the slope becomes negative. This was due to the machine thinking that the sample had fractured and it stopped recording data. It is believed that the 20.1% sample would follow the same trend as the last two though, and would fracture shortly after ultimate compressive strength (UCS). The UCS for the three samples are listed in **Table 2.2**. As is expected the UCS increases with decreasing porosity.

2.5 Discussion

2.5.0 Microstructure

The laser processed microstructure of Ti6Al4V has been known to change the properties of the metal. The martensitic like structure tends to increase the hardness due to the alloying elements forming tiny compounds such as Ti_3Al. These small compounds are hard spots that improve microhardness [7]. This intern can also make the structure more brittle. The dispersed α' grains that are randomly oriented in a martensitic type manner are characteristic of Widmanstatten structure [17]. This happens when cluster of α laths group together, which happens during the β to α transition. To truly know the mechanical properties and hardness of these structures, more mechanical testing must be done.

2.5.1 Building Porous Ti6Al4V Structures

Finding the proper hatch distance, powder feed rate, and laser power proved to be difficult. In order to make fine pore size there needed to be very little distance between each hatch. As laser power increased, more material melted, and made thicker hatches. Likewise, as the powder feed rate was increased, larger hatches were made. It was difficult to figure out these parameters because as one changes, the others needed to be adjusted. It was found that a hatch distance of 0.025 and 0.03in. worked well to make small gaps between hatches when the PFR was 17.9 g/min

and laser power was 31A. To make fully dense Ti6Al4, generally a laser power of 40W is used. A low laser power was used in order to only partially sinter the Ti6Al4V powder and make a structure of powder metal all partially bonded together. This would make very fine channels between areas that were left open by the hatches. Therefore, the structure has larger channels that air can pass through, but in-between those channels there is randomly oriented partially melted powder that obstructs direct flow.

2.5.2 Morphology of Structure

The resulting scaffold structure provides many advantages over traditional manufacturing and other AM processes. The partially sintered powders obstruct passage ways that are present throughout the scaffold. In Fig 4 these globules of Ti6Al4V can be seen in the middle of the channels. This increases the filtering ability of the structure as well as the surface area. Porous structures have been used in the past as catalyst for various processes. For higher efficiency it is optimal to have the highest surface area per unit volume [18]. The small globules in the LENS processes structure provide an increase in surface area, as well as extra filtration ability if used for such an application.

These obstructed channels are unique to LENS processes samples compared to other AM processes. Other AM processes can make porous structures with interconnected porosity, as listed in the introduction. Many of them can make fine interconnected porosity and channels as well. A distinct difference the LENS process has is the randomness and internal obstruction of the interconnected channels. **Fig 2.9** shows a schematic representing different types of internal porosity. Some AM processes can make micro porous scaffolds, but only have internal channels that run strait through the sample. This means the only thing obstructing flow or filters undesirables is the channel size. This type of pore can be seen in **Fig 2.9A**. Many of the other AM processes

used to make scaffolds also can make designed porosity with internal channel structures that make a non-direct path through the sample. It is a large advantage of other AM systems that they have the ability to make designed porosity then make a scaffold almost exactly as the design[7,18]. The channels then obstruct direct flow, increasing filtering capability and surface area of the structure. **Fig 2.9B** is an example of this type of structure. As mentioned before, the porous structures in this study were not made from a CAD designed pore structure, but by adjusting the processing parameters of the build. The pore structure was created by producing hatches near each other, then having powder spill over and partially sinter between them. This left a scaffold with the structure of **Fig 2.9A**, but added random oriented powder in between the hatches. The partially sintered particles build up and obstruct the passages in the center of the channel as well as add extra surface area and roughness. A representative schematic of this can be seen in **Fig 2.9C**. This structure could be favored in applications where high surface area and filtration capabilities are required.

Another advantage to the LENS processed structure is the dense supporting columns that are present across the samples. Fig 4 shows the columns present in the Z-direction of the build. These columns form where two hatches cross each other during the build. Fig 4 in particular is an image of a [0/90]˚ specimen. This means the columns form where the 0˚ crosses the 90˚ hatch. **Fig 2.3** point out where this would be located on the top section. These structures add strength and structural integrity to the scaffold. They are oriented in the X, Y, and Z directions, giving support in the horizontal and vertical directions. The number and direction of these support columns can be changed with different hatch orientation. For example samples 3 and 4 were built using [0/120/240]˚. This would mean there were support structures in all those directions, as well as the Z-direction.

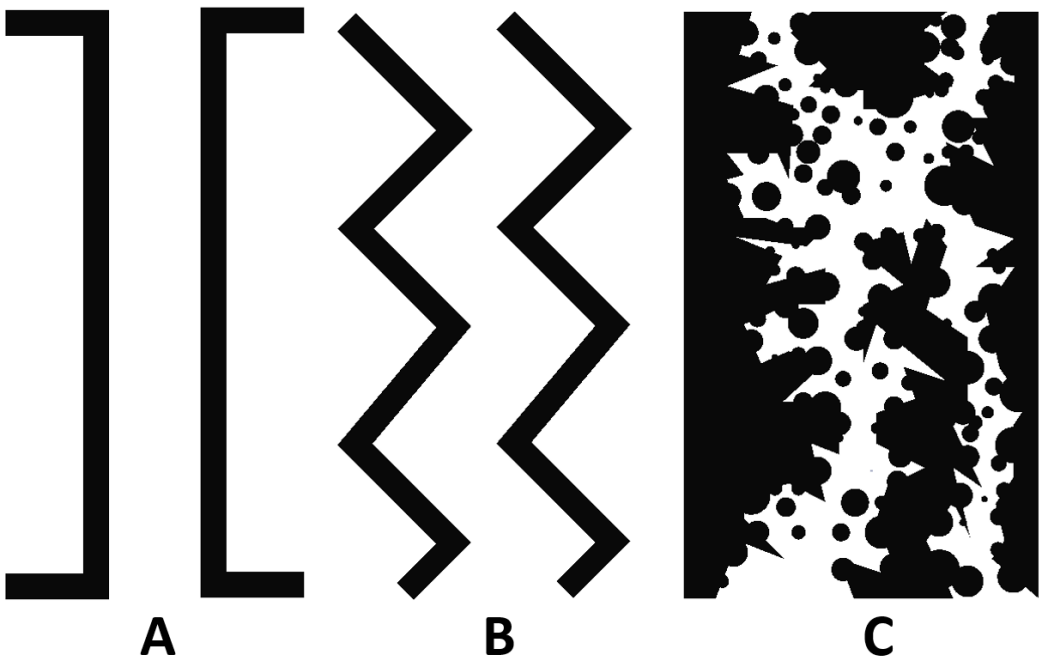

Figure 2.9: Images of different pore structure AM is capable of making. (A) Direct channel where gas and particles that are smaller than the pore size can pass through. (B) Non-Direct Channel where gas and items cannot directly pass, but structure is still open between channels. (C) LENS processed porous structure with non-direct channels, variability on walls, and obstructions in between passage ways.

2.5.3 Compressive Strength

As expected, the UCS decreased with increasing porosity. An interesting thing that occurred was there was a much larger difference in the UCS between the 19.7% and 20.1% porosity (74.6MPa) compared to the difference between 15.9% and 19.7% (14.5MPa). This could possibly suggest as porosity continues to increase, the UCS begins to decrease at an increasing rate. Yet there is too little of data to draw any major conclusions. In one study the compressive strength of 17% porous pure titanium structure developed using LENS processing was found to have an UCS of 463MPa [2]. This was the closest study found to the testing done for this paper. The 17% pure

titanium had 182.4MPa less than the 15.9% sample from this study. There were no other reports of UCS of Ti6Al4V with this low of porosity to compare the results to. The UCS of pure Ti6Al4V is ~1000MPa [16]. This means that the addition of 15.9% porosity reduces the UCS by roughly 35%. Overall this shows the scaffold still has a relatively high UCS even with the added porosity, and is still substantially more than CP-Ti with roughly the same porosity.

2.5.4 Designed vs. Processed Porosity

When comparing the designed porosity and the LENS processed porous structures, there are pros and cons for each. The designed porosity can yield very predictable structures with homogeneity. It can be tailored to have different sizes and integrated into a design of a larger structure. Yet it would be difficult or impossible to create a designed porosity that has the morphology of the LENS processed structure. As mentioned earlier this structure could be favorable for high surface area and filtration applications. One problem that always arises with random structure is if it is reproducible. In our study we found that using the same parameters yielded near the same porosity (±2.0%), build quality, and always produced interconnected porosity. It can be seen in **Fig 2.4** that even though there is variation across the structure, the overall structure has the same pattern. From this it can be said the structure is reproducible and consistent with a small degree of error.

Another large advantage is these structures can be added to a part at any given time during the build. Since this structure is not designed in a CAD file, it can manually be added to any structure by simply changing the building parameters. This could add simplicity to a build instead of trying to add porosity to the CAD model of the entire part. Though this tactic may not be ideal for all situations, it could prove to be an easy solution in some. For example, if a designer want to add a porous structure to an intake of a part. Instead of spending all the time designing it, they just add

a solid plate covering the intake in the CAD file. Then the operator programs the build speed and parameters into the machine, and changes them for when it builds this particular plate to the parameters that produce the desired porosity. Then the part can be built with microporous intake filter with little to no effort in changing the design.

2.6 Summary

Porous structures are an important and needed structure in many modern day applications. They are difficult structure to make, especially if fine interconnected porosity is desired. AM processes have been looked at to make these structures due to their versatility and ability to make intricate geometries. In this study LENS was used to make micro porous structures out of Ti6Al4V. The structure was made by changing the build parameters as opposed to designing a CAD model of the pore structure. After optimization of build parameters interconnected porous structures were made with porosity ranging from 21% to 15.5%. The structures had a supporting network of dense columns with obstructed interconnected channels in between them. The obstructions were made by partially sintered Ti6Al4V powder that were created by using a slow scan speed and low laser power. Visual analysis of the structure shows it would have higher surface area and be ideal for use as a filter due to the globules of metal in the center of the interconnected channels. The structure had an ultimate compressive strength that varied from 645-556MPa. The microstructure was similar to that of laser processed Ti6Al4V with martensitic like grains. Overall LENS proved to be a viable way to make porous structure by only changing build parameters, which means the structure could be added to any part of a build and implemented easily on designs.

2.7 References

1. Balla KV, Bose S, Bandyopadhyay A. Low stiffness porous Ti structures for load-bearing implants. *Acta Biomater*. 2007;3(6):997-1006. doi:10.1016/j.actbio.2007.03.008.

2. Xue W, Krishna BV, Bandyopadhyay A, Bose S. Processing and biocompatibility evaluation of laser processed porous titanium. *Acta Biomater*. 2007;3(6):1007-1018. doi:10.1016/j.actbio.2007.05.009.

3. de Peppo GM, Palmquist a., Borchardt P, et al. Free-Form-Fabricated Commercially Pure Ti and Ti6Al4V Porous Scaffolds Support the Growth of Human Embryonic Stem Cell-Derived Mesodermal Progenitors. *Sci World J*. 2012;2012:1-14. doi:10.1100/2012/646417.

4. Hollander D a., Von Walter M, Wirtz T, et al. Structural, mechanical and in vitro characterization of individually structured Ti-6Al-4V produced by direct laser forming. *Biomaterials*. 2006;27(7):955-963. doi:10.1016/j.biomaterials.2005.07.041.

5. Ryan GE, Pandit AS, Apatsidis DP. Porous titanium scaffolds fabricated using a rapid prototyping and powder metallurgy technique. *Biomaterials*. 2008;29(27):3625-3635. doi:10.1016/j.biomaterials.2008.05.032.

6. Cheng XY, Li SJ, Murr LE, et al. Compression deformation behavior of Ti–6Al–4V alloy with cellular structures fabricated by electron beam melting. *J Mech Behav Biomed Mater*. 2012;16:153-162. doi:10.1016/j.jmbbm.2012.10.005.

7. Sun J, Yang Y, Wang D. Mechanical properties of a Ti6Al4V porous structure produced by selective laser melting. *Mater Des*. 2013;49:545-552. doi:10.1016/j.matdes.2013.01.038.

8. Wu Y-C, Lee T-M, Chiu K-H, Shaw S-Y, Yang C-Y. A comparative study of the physical and mechanical properties of three natural corals based on the criteria for bone-tissue engineering scaffolds. *J Mater Sci Mater Med*. 2009;20(6):1273-1280. doi:10.1007/s10856-009-3695-3.

9. Yusop a. H, Bakir a. a., Shaharom N a., Abdul Kadir MR, Hermawan H. Porous biodegradable metals for hard tissue scaffolds: A review. *Int J Biomater*. 2012;2012. doi:10.1155/2012/641430.

10. Wauthle R, Vrancken B, Beynaerts B, et al. Effects of build orientation and heat treatment on the microstructure and mechanical properties of selective laser melted Ti6Al4V lattice structures. *Addit Manuf*. 2015;5:77-84. doi:10.1016/j.addma.2014.12.008.

11. Matyas J, Wegeng R, Robinson M, Casella A, Mccloy J. Experimental Characterization of Thermal Wadis in Support of Lunar Exploration. 2011;(September).

12. Kruth JP, Levy G, Klocke F, Childs THC. Consolidation phenomena in laser and powder-bed based layered manufacturing. *CIRP Ann - Manuf Technol*. 2007;56(2):730-759. doi:10.1016/j.cirp.2007.10.004.

13. Cain V, Thijs L, Van Humbeeck J, Van Hooreweder B, Knutsen R. Crack propagation and

fracture toughness of Ti6Al4V alloy produced by selective laser melting. *Addit Manuf*. 2014;5:68-76. doi:10.1016/j.addma.2014.12.006.

14. Hosford WF. *Physical Metallurgy, Second Edition*. Taylor & Francis; 2010.

15. Bandyopadhyay A, Krishna B V., Xue W, Bose S. Application of Laser Engineered Net Shaping (LENS) to manufacture porous and functionally graded structures for load bearing implants. *J Mater Sci Mater Med*. 2009;20(SUPPL. 1):S29-S34. doi:10.1007/s10856-008-3478-2.

16. Hibbeler RC. *Mechanics of Materials*. Vol 8th ed. Upper Saddle River, NJ 07458: Pearson Prentice Hall; 2011.

17. Collins PC, Banerjee R, Banerjee S, Fraser HL. Laser deposition of compositionally graded titanium-vanadium and titanium-molybdenum alloys. *Mater Sci Eng A*. 2003;352(1-2):118-128. doi:10.1016/S0921-5093(02)00909-7.

18. Yadroitsev I, Shishkovsky I, Bertrand P, Smurov I. Manufacturing of fine-structured 3D porous filter elements by selective laser melting. *Appl Surf Sci*. 2009;255(10):5523-5527. doi:10.1016/j.apsusc.2008.07.154.

CHAPTER THREE

VANADIUM CARBIDE METAL-CERAMIC COMPOSITE COATINGS

3.1 Introduction.

VC has incredible hardness (~ 2500 HV), high wear resistance, and a high melting temperature (2810˚C)[1,2]. It is a part of the group VB that is known to make very hard phases in many common alloys[3]. In the past it has been used to strengthen steel as a protective coating for tooling and other components[4–6]. This added strength increased modulus and hardness which has shown to increase resistance to cavitation and abrasive wear damage[7,8]. An easy and cost effective way to protect a part from damage is to add a surface treatment, which can be done by laser surface treatment[4,9]. It would also be ideal if this coating could be gradient and have the ability to gradually increase the protective capabilities. Likewise, be able to fix damaged parts by not only adding back material, but increasing resistance to future damage as well. It was hypothesized that LENS could deposit a gradient coating of VC in SS304 to make an metal matrix composite (MMC) with increased hardness, wear resistance, and abrasive water resistance. The LENS process could then be used to build and add these coatings to new parts, or repair damaged ones and add extra protection.

3.2 Materials and Methods

3.2.0 LENS Processing

VC powder was purchased from American Elements® with 99% purity and a particle size of -100/+270 mesh. 304/304L (SS304) powder was bought from Carpenter® with a powder size of -140/+325 mesh. The composition of the powder is listed in **Table 3.1**. They were mixed in proportions of 0%, 5%, 10%, and 20%wt.VC. Powders were weighed and mixed on a ball mill for

one hour to ensure thorough mixing and heterogeneity. For the rest of this paper the coatings will be referred to by their respective VC content. Coatings were mixed before and not mixed using the LENS to know the exact content of the VC powder. The LENS could mix the powders by loading each one separately into different hoppers. The LENS system used had two hoppers that could be engaged separately or at the same time. If this was done the composition could gradually be changed at any rate the operator desired. This gives complete control of the rate of change and ratio of VC:SS304. If this was done it would be difficult to know the exact amount of VC in each coating. Therefore, the powders were mixed before in exact weight amounts for research purposes.

Table 3.1: Chemical Compositions of Materials Used (wt.%)

	C	Cr	Ni	P	Si	Mn	S	N
304/304L Plate	0.022	18.15	8.05	0.033	0.44	1.72	0.0003	0.07
304/30L Powder	0.03	18 to 20	8 to 12	0.045	1	2	0.030	-

Coatings were deposited on both SS316 and SS304 substrates, but only the SS304 results will be reported. SS316 was first used because it was all that was available at the time. The intention of this study was to build only on SS304. Since only the coatings properties were tested and not the substrate, no analysis of SS316 was done in this paper. The only thing analyzed was the coatings adhesion to the SS316. All mechanical properties were tested away from the bond zone. Adding the coating to SS316 should not change the bulk coatings properties. SS316 is very similar to SS304 with the a slight differences of Ni and Cr proportions, and the addition of small amounts of Mo and Co[10]. Once SS304 substrates arrived, all coatings were built on the SS304. Hot rolled SS304 substrates were purchased from Penn Stainless Products and its constituent elements are listed in **Table 3.1**.

Table 3.2: Build Parameters of Coatings[†]

	Hatch (in.)	Angle (˚)	Slice (in)	PF[*] (g/min)	Power (W)
All Compositions[‡]	0.015	[0, 90]˚	0.015	27.6	580
100%VC	0.015	[0, 90]˚	0.015	21.0	650

* Powder feed rate is estimated by calculation of other powders feed rates, and difference in densities leaves some error
† All laser passes were done at the power as the deposition of the coating
‡ All compositions except 100%VC

Coatings were made using a LENS 750 (Optomec Inc., Albuquerque, NM). Description of LENS processing is in the first chapter (pg. 2). Parameters were chosen based on past work done in the lab. After some trail an error a set of parameters were chosen. These are listed in **Table 3.2**, and were used for all the coating with the exception of the 100%VC. This was done in order to keep consistency between the coatings, and only study how the addition of carbides changed the coating properties. The 100%VC were made differently because of past research and the fact VC has a very high melting temperature (2810˚C)[2]. It was assumed that higher power would ensure better diffusion into the coating, as well as be more likely to melt the powder. All samples were made in argon gas with oxygen levels below 30ppm.

For each samples two layers were deposited in a .42in x .58in rectangle with one contour. The only exception to this was the 100%VC which was deposited twice on top of a 20%VC sample to make a gradient coating. For each composition a sample was also made with an additional laser pass. This means after the second layer was deposited, the powder feeder was shut off and the laser was run over the sample again at the same speed and power as it was built. This was in order to densify and smooth the surface of the coating. This method has shown in the past to increase the hardness of SS410 and Ti6Al4V [11,12]. A sample was also made with a laser pass being performed on each layer, to see if it helped to densify the coating even more. After the first batch of samples

was created it was apparent the coatings were porous. Because of this a 20%VC sample was made with a laser pass done on each layer to try and make the coating denser. Also to show proof of being able to make a gradient filling on a broken part, a 12mm diameter cylinder was built with twenty layers of 10%VC, twenty layers of 20%VC, and five layers of 100%VC. All parameters remained the same for the respective coatings of the cylinder.

3.2.1 Physical Characterization

The microstructure was analyzed by first grinding and polishing the top surface. Silicon carbide paper was used successively with 120, 300, 600 and 1000 grit sandpapers. Sample surfaces were then polished on a felt disc with 1µm, 0.5µm and 0.3µm alumina powder until surfaces had a mirror surface finish. Polished surfaces were then etched with either 15ml HCl – 5ml HNO_3 – 100ml H_2O or 100ml HCl – 5ml H_2O_2 (30%). Different etchants were used because results were slightly different between samples from the first etchant. It was later found the second etchant worked much better and was used for all samples after the first batch. Each sample was then examined in a field emission scanning electron microscope (FEI Quanta 200, OR). Energy dispersive spectroscopy (EDS) was done down the cross section of the gradient cylinder with a Field Emission SEM (FE Sirion, Portland, OR) fitted with a Genesis EDAX detector. XRD analysis was done on the coatings using a Cu Kα1 radiation (PANalytical X'Pert Pro MPD, Netherlands).

3.2.2 Mechanical Characterization

The coatings hardness, wear rate, coefficient of friction (COF), and abrasive water resistance were all examined. Hardness was measured down the cross section of the coatings starting at the top surface, and taking a measurement every 0.2mm until the substrate was reached. Then a few more data points were taken into the bulk of the substrate. Measurements were taken

using a Vickers micro hardness tester (HMV-2T, Shimadzu, Kyoto, Japan). A load of 0.9807N with a dwell time of 15s. Three passes were done down the depth of each sample and the averages of the top surface were reported.

Wear rate and COF were measured using a Nanovea series tribometer (Microphotonics Inc., CA. USA). A linear reciprocating test was conducted with a spherical pin on the square coatings. A silicon nitride ball with a 3mm diameter was used with a 10mm stroke length, 5N load, 1200mm/min speed, and 1km distance. 1km was chosen to determine stable COF and also cause enough material loss to have an observable wear track. Test were done in DI water at room temperature. Images of the wear tracks were taken with an optical microscope to measure the width of the wear track and calculate approximate wear rate. Force sensors recorded data from the tribometer as it took a measurement every 100ms and was reported as a sine curve. The average value of the curve was found and made the zero value. Absolute value of the adjustment from the baseline was taken to make all the data positive. Then for every 5000 values the largest 10 were averaged and divided by 5N to normalize the data and attain the static COF.

Abrasive water tests were conducted using an OMAX 2652 JetMachining® Center abrasive water jet (OMAX, Kent, WA). Samples were built in linear patterns on a SS304 plate. Abrasive water was then shot at the samples and run over them at 180in/min. The spot size of the jet was 0.030in, it was shot at 49Ksi, with a 1lb/min garnet flow rate. 80 HPA® (High Performance Alluvial) garnet (Barton, StreetGlens Falls, NY) was used as the abrasive. Three test were run down each coating, and there were two of each type of coating. The cross section of the cut area was then analyzed and compared.

3.3 Results

3.3.0 Processing Parameters

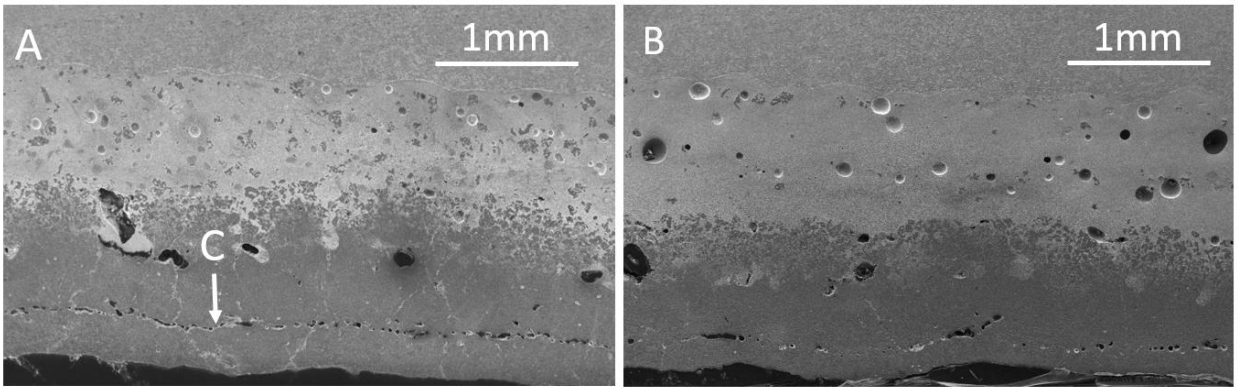

Figure 3.1: (A) SEM image of a coating with two layers 100%VC (bottom), 2 layers 20%VC in the center, on a SS304 Substrate (B) SEM image of a coating with the same compositions as A, but had a laser pass on each layer of the 20%VC, and one laser pass on the top layer of the 100%VC (C) Porous gap between first and second 100% VC coating

A high laser power was used in order to melt and integrate the VC into the stainless steel. Past research has even used higher laser powers than our machine is capable of reaching[5]. Lower laser power has shown to retain more austenite[11]. This study wanted to increase abrasive water and cavitation resistance of the metal, which a martensitic structure is better suited. Higher power has been shown to produce more martensite and also should better diffuse the VC into the coating. For these reasons a higher laser power was used for the 100%VC.

A difficulty with LENS processing is it takes a long time to optimize parameters. When doing the first set of builds parameters are chosen based on past research and the operators knowledge of the LENS. Then the only way to know if the coatings were dense at the time is by visual inspection through the radiation shielding panel. In order to really see the build quality, the parts must be taken out of the machine, cut from the substrate, and analyzed by a microscope. This

takes a considerable amount of time and is why optimizing build parameters takes a considerable amount of time, material, and trials. Full optimization of building parameters was not done in this study for the reasons mentioned, with an emphasis on the time and cost of materials. Since this study was done for initial proof of concept and material property testing, the porous coatings made were deemed satisfactory.

The goal of this study was to have fully dense coatings and parameters were chosen to try and achieve this. When the first pure SS304 coatings were built they appeared to be dense by visual inspection while in the LENS. Since it appeared good the parameters were used for all the other coatings. This was in order to keep consistency between the samples. Even if one parameter is changed, it can change the mechanical properties of the coating. This is because any change in parameters changes the shape and dynamics of the melt pool, which changes the thermal history, and subsequently produces a different grain structure[13]. Therefore, it was important for testing to keep all parameters the same for the coatings with mixed compositions to compare. Though if these coatings were going to be used in a real application, optimization for all different compositions should be done. When the first batch of coatings were finally cut and analyzed it was found they all had varying degrees of porosity. When this was found it was hypothesized that possibly by doing a laser pass on each layer deposited would help to densify the coating. This was tried when making the 20%VC coating.

The high laser power used when depositing the 100%VC effectively melted the powder but did result in some cracking and porosity. There is a highly porous layer between the first and second layer deposited which can be seen in **Fig. 3.1C**. This could weaken the top layer and inhibit the ability to build multiple layers on a structure with good mechanical properties. Since this layer was present and the laser was melting the VC, it was hypothesized that by running a laser pass on

the top layer, it could help to bond the two layers and get rid of the porosity. The results from this will be discussed later. There are definite dense areas of the VC deposited, but also many areas of very fine microporous structure. This is most likely a result of solidification of the particles not melting and densifying completely. It could also be because the laser was not melting the VC fully, or the dynamics of solidification have a tendency to leave small porosity upon cooling. In past work VC powder has very small porosity in the particles[14]. The porous areas of the coating have a very similar appearance. By visual inspection of the top surface of the polished VC there is some cracking apparent and pores. Also when building the 100%VC the layers deposited were not as thick as the mixture coatings.

3.3.1 Microstructure

LENS processing of SS304 resulted in finer small grains with more heterogeneous morphology. Microstructure of all the samples can be seen in **Fig 3.2**.The grains in the substrate were much larger and typical of a hot rolled plate 304[15,16]. The grains have a non-uniform size and shape dispersed in grains elongated in the direction the plate was rolled. This is better shown in a less magnified image, which can be seen in **Fig 3.3**. It is quite apparent that LENS processing caused a significant decrease in grain size. This is typical of LENS due to fast solidification rates but also can be a factor of other causes[17,18]. In the 5%VC, 10%VC, and 20%VC samples the grain structures all look very similar. They have roughly the same morphology and size as the SS304, but there is now a lighter color material occupying the grain boundaries. Looking at the 5%VC, it appears there is less of the lighter color material, with some grain boundaries still being void like in the SS304. The 10% sample seems to have almost all the grain boundaries occupied, and the

20%VC is fully saturated with the material. **Fig 3.4** is a larger image of the 20%VC laser pass grain structure. Along with being on the grain boundaries, there are also small globules dispersed

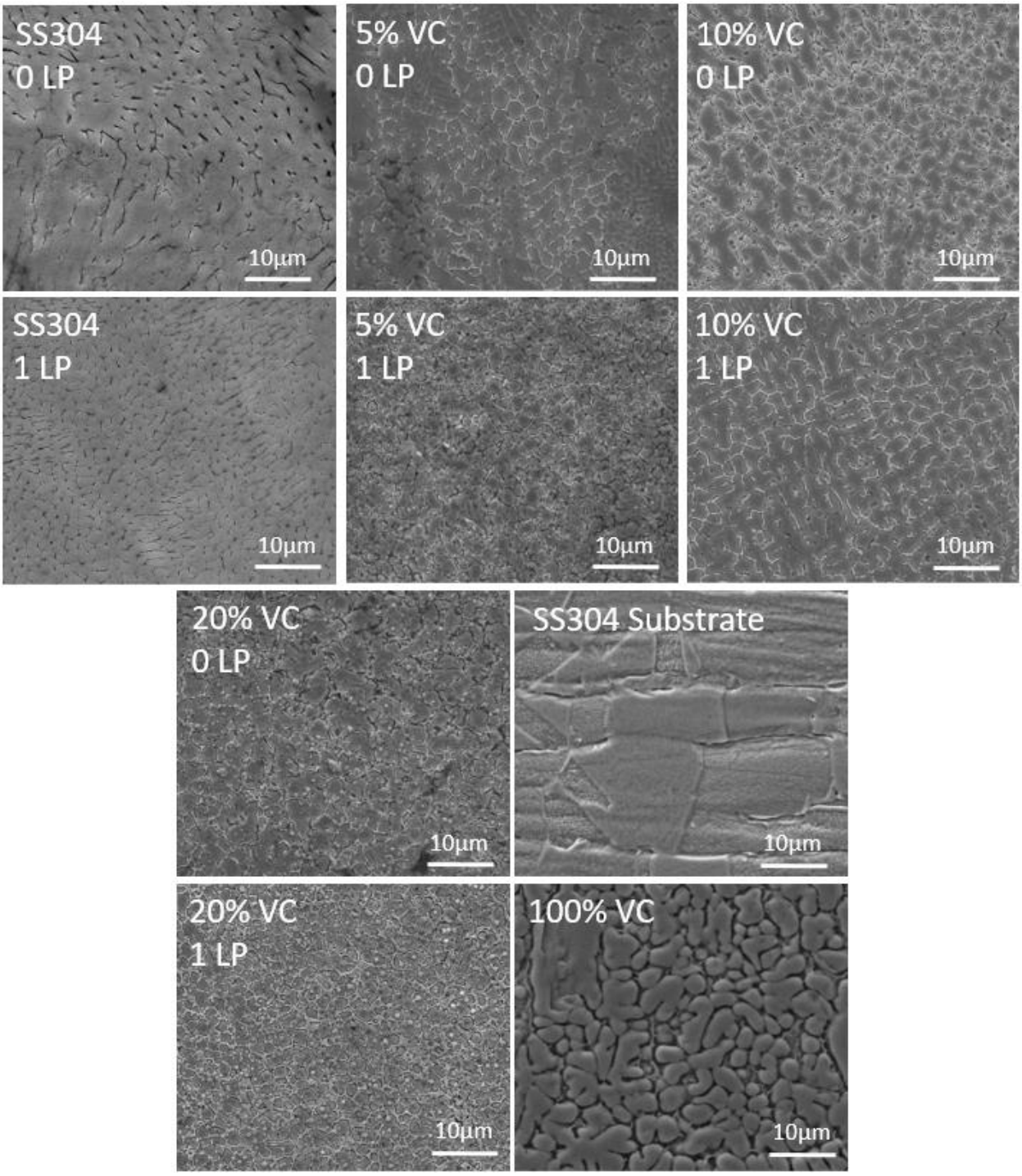

Figure 3.2: Microstructure of all samples

on the grains. The structure is very homogeneous as there appears to be no area void of the material. Due to the lighter color material being absent in the SS304 and present in all other samples, it is quite apparent it is VC or other constituent compounds formed during processing. This has also been seen in the past when a high vanadium content steel, Vanadis 4, was deposited using a laser[5].

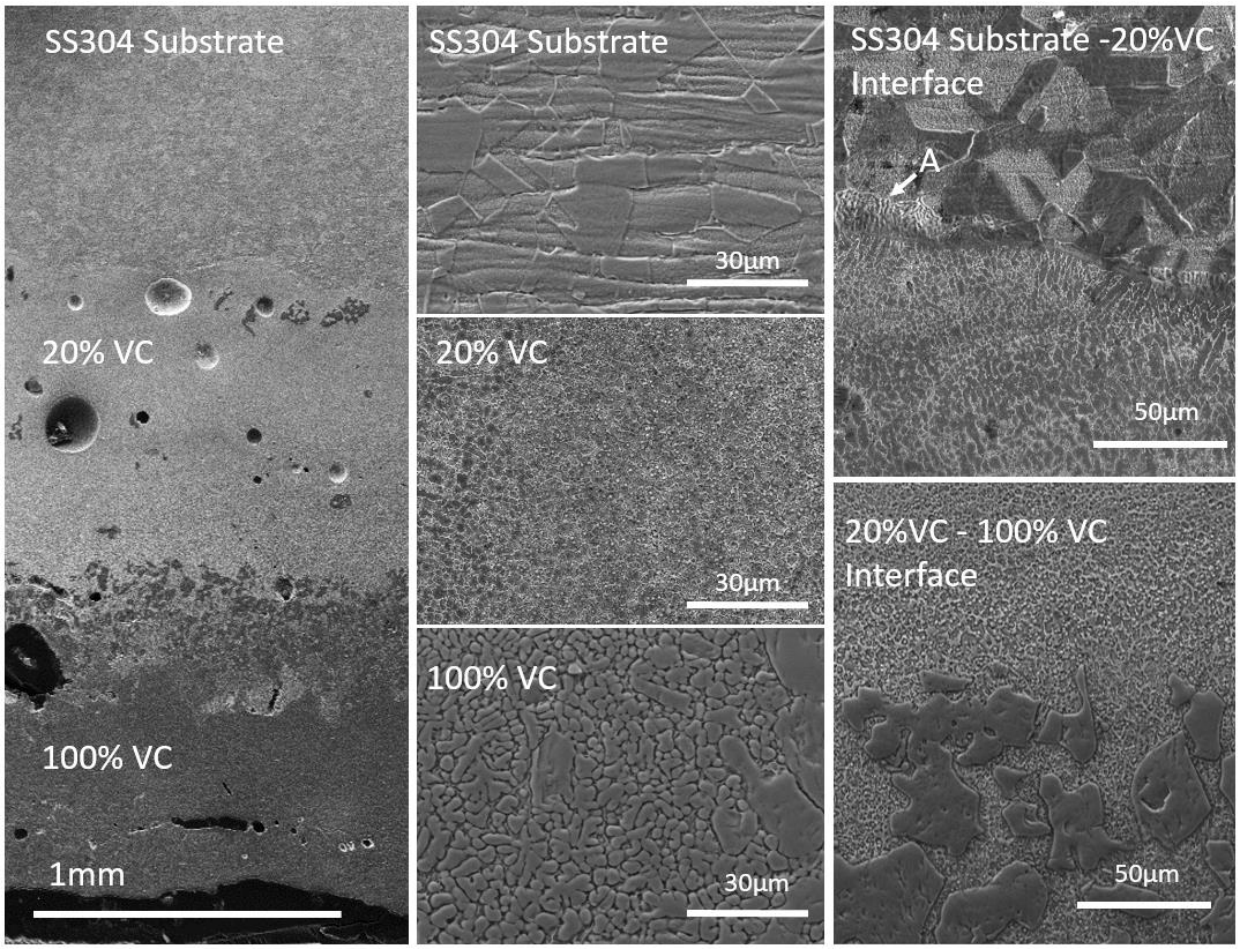

Figure 3.3: (Left) Image of 100%VC-20%VC-SS304 coatings (Center) Image of the respective grain structures at each layer (Right) Image of interfaces between each layer.

Fig 3.3 shows the coating from **Fig 3.1B**. The left most image is the profile of the coating, next to it is the respective microstructures of each layer, and to the right of them are the interfaces between each layer. The interface between the SS304 substrate and 20%VC coating shows a distinctive line were the coating bonded to the substrate. Inspecting the interface, there appeared

to be no gaps or pores between the two zones. There were some pores near the interface in the coating, few to none on the interface. There is a distinct line where the grain structures change size, but no micro-porous area, or large bond area that could be brittle or a week spot. An interesting thing to note is it appears the substrate has no change in grain structure near the interface. This means there was no notable heat affected zone (HAZ), or it is highly localized. **Fig 3.3A** shows a small area of grains that look more like the SS304 coatings. They are small grains but have no VC in the grain boundaries. There are a few areas like these along the interface, but a majority of it is a distinctive boundary with no visible HAZ.

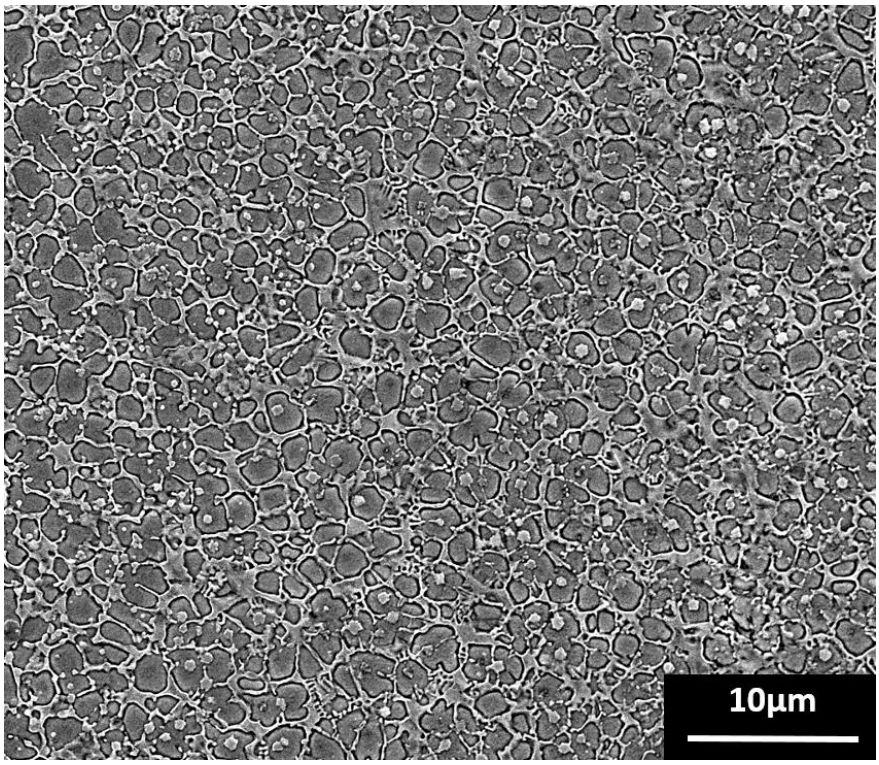

Figure 3.4: 20%VC microstructure

The 100%VC to 20%VC have a much more gradient interface. **Fig 3.5** is a larger image of the interface to display just how gradient it is. As 100%VC is deposited the VC is mixed and with the primarily SS304 coating and disperses into roughly 50µm precipitates. These precipitates are curved and have few to no sharp edges, which suggest the VC is dissolving in the surrounding

matrix[19]. It then gradually became more VC until only pockets of the 20%VC coating were remaining. Finally, it became 100%VC. There is some large porosity between the interface which could be seen in **Fig 3.1**.

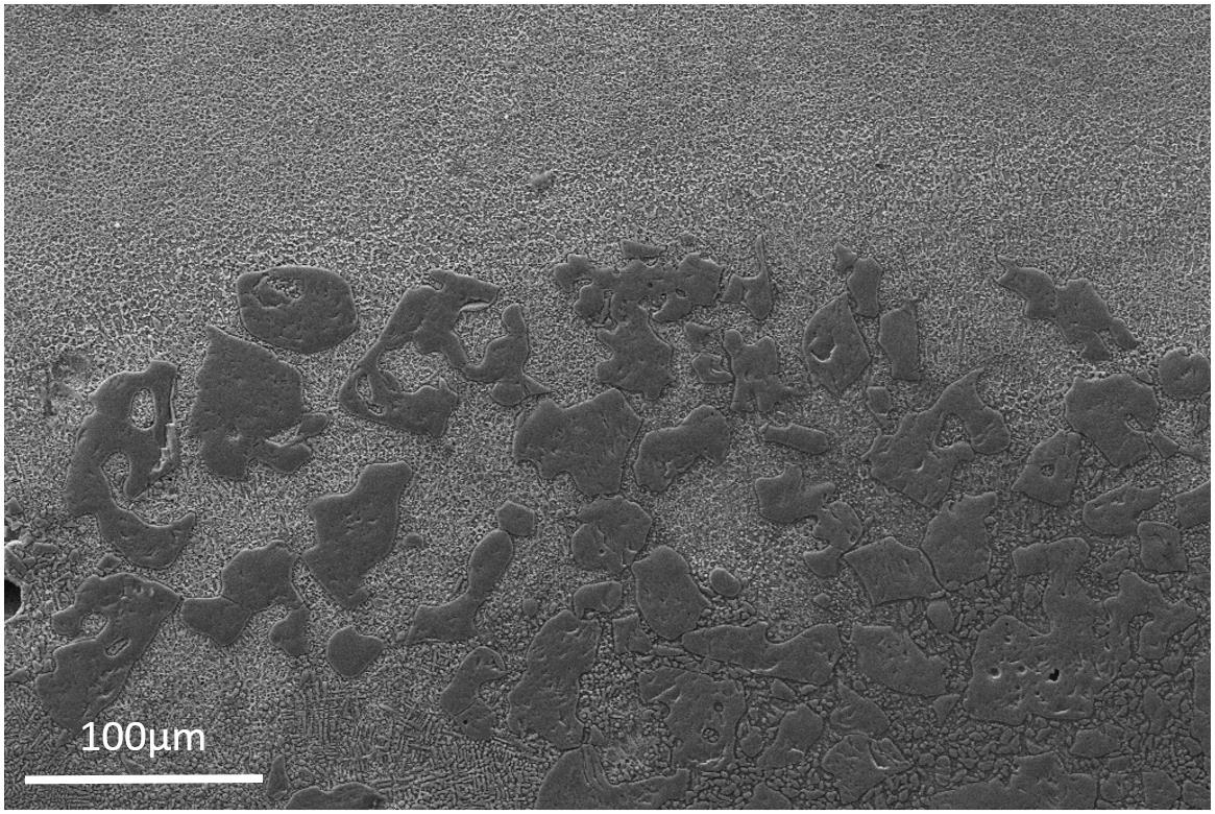

Figure 3.5: Interface of 100%VC and 20%VC coating

3.3.2 Effect of Laser Pass

The laser pass proved to densify the metal at the surface, as well as increase the distribution of the VC. When comparing the laser pass grains to the non-laser pass in **Fig 3.2**, there was not a very large difference in the grain morphology or size. In the SS304 the grains do appear to become slightly smaller and more homogeneous. Between the VC samples this is harder to distinguish. The images were taken near the top surface to be sure they were in the HAZ. In almost all the images, it appears the VC was more heterogeneously distributed between the grains. The grain morphology also seems more uniform as well.

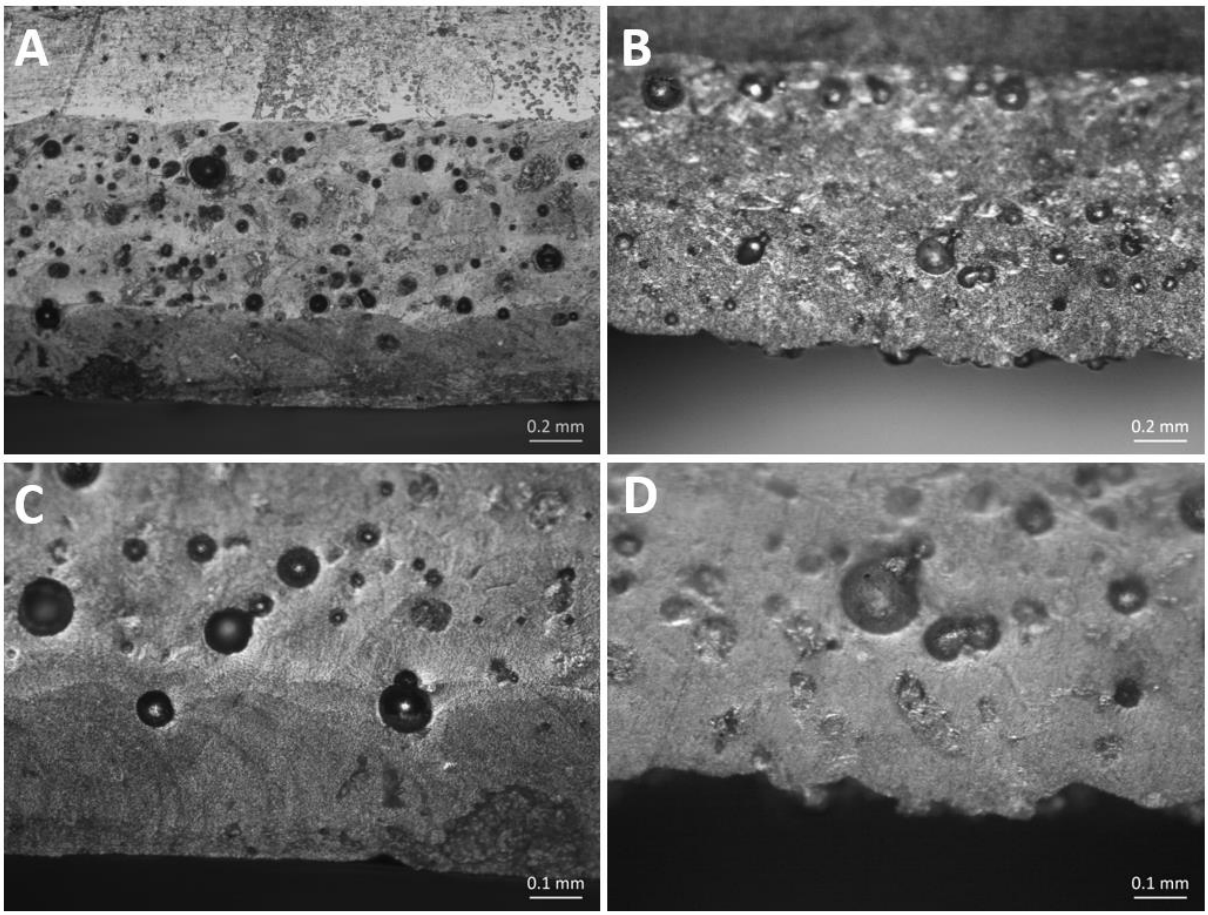

Figure 3.6: A & C are optical images of 5%VC coating with a laser pass. B & D are images of 5%VC without a laser pass.

By visual inspection the laser pass smoothed out the top surface that was rough prior. As it passed on the top surface it created another melt pool. This gave the top surface more time for diffusion and for the voids to collapse. The result is a majority of the voids and pores closing and densification of the coating. By optical inspection of the cross section of the coating, it can be seen that roughly 300µm deep in the laser pass sample the coating had no pores. **Fig 3.6** is an image of the laser pass 5%VC sample and no laser pass 5%VC sample. The top surface ~ 300µm deep is almost completely dense. Any deeper into the coating the pores returned and are roughly the same size as with no laser pass. It can also be seen that the top surface was flat and relatively even

compared to the rough surface of the non-laser pass. This shows that the laser pass did densify the coating to a certain depth.

3.3.3 XRD Analysis.

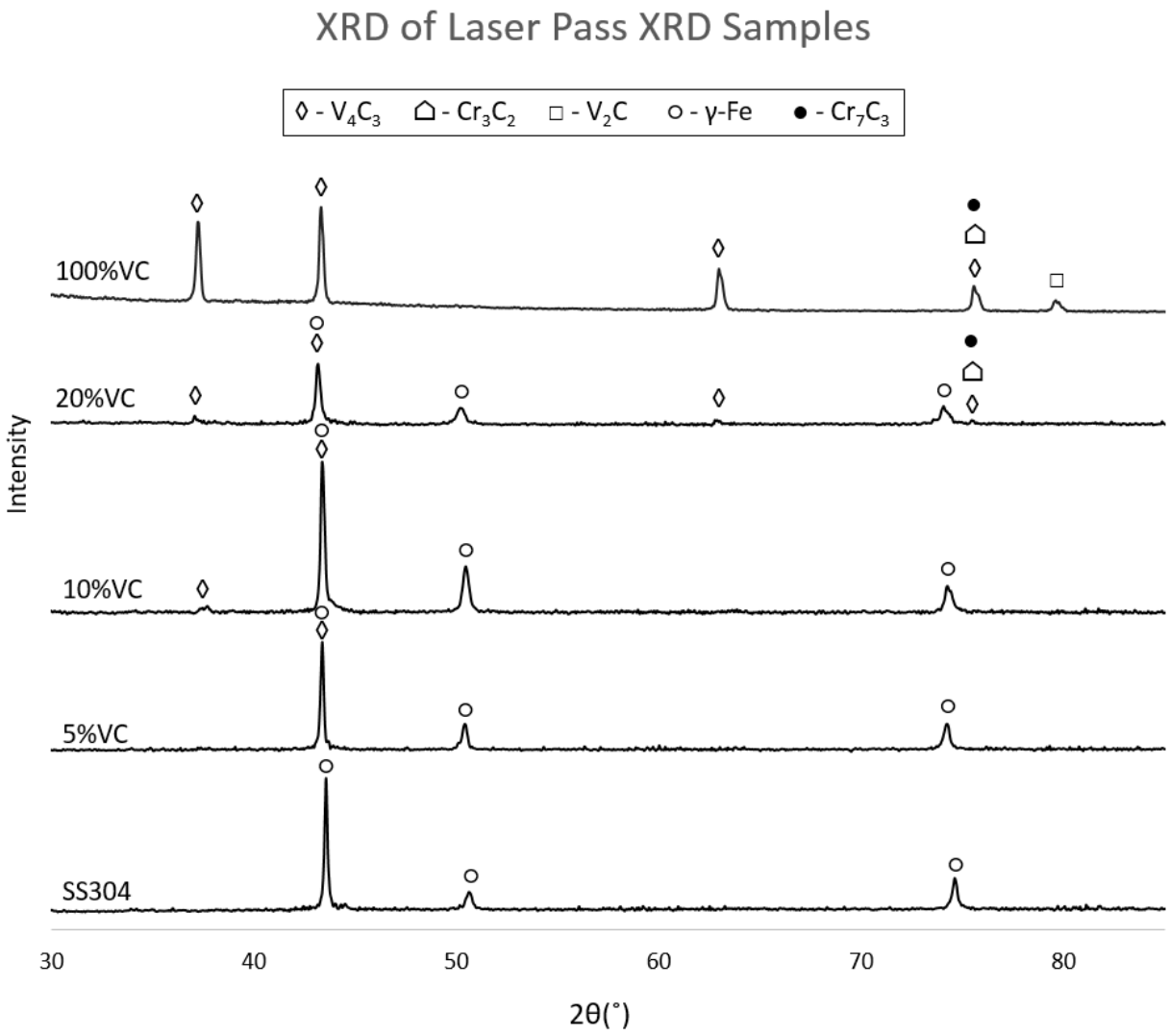

Figure 3.7: XRD plots of all VC samples

Figure 3.7 shows the XRD curves for all the compositions. Analysis of the graphs show shows that the SS304 was all γ-Fe. The 3 peaks present were 43.8˚ - γ (111), 51˚ - γ(200), and 74.8˚ - γ(220)[16,20]. Peaks at 37.2˚, 43.3˚, 62.9˚, and 75.5˚ are peaks for V_4C_3 (ICDD PDF #001-1159)[2]. The last peak at 79.6˚ is for V_2C (ICDD PDF #071-1258)[2]. One research paper has shown

Cr_7C_3 and Cr_3C_2 also have a peak at 75.5°[21]. Whether or not it is present will be discussed later. Shifting of the peaks is caused by the introduction of VC to the structure. As the amount of carbides increased the large peak had a slight shift to the left. This is can be described by Bragg's equation ($2d\sin\theta = n\lambda$). The VC causes lattice strain and increases the interplanar spacing of iron. This increase of spacing has been known to cause small shifts in the peak[22]. Therefore, the large peak is a mixture of the V_4C_3 and γ-Fe peak.

As more VC is added the more V_4C_3 peaks begin to develop. Between SS304 and 5%VC, the major peak shifts slightly to the left but nothing else changes. At 10%VC the 37.2° V_4C_3 peak begins to develop. At 20%VC the 62.9° and 75.5° have very small peaks. Then at 100% there is no γ-Fe phase peaks left, and only V_4C_3 and V_2C. Though XRD cannot quantify the amount of each phase when analyzing a solid sample, there is only one small peak for the V_2C, and very strong peaks for V_4C_3. This suggest that the 100% VC is primarily all V_4C_3. It should be noted the peaks are broadening as the carbide content increases. The broadening of the peak as the carbide content increases indicates that the grains structure is either smaller based on the Scherrer equation or there is more strain in the grain structure[2].

3.3.4 EDS Analysis

Fig 3.8 is an image EDS mapping done on the SS304 substrate, 10%VC, 20%VC, and 100%VC. When mapping was done, an area with one of the precipitates was chosen to characterize what they were made of. The SS304 substrate shows primarily iron and chromium, with evenly distributed Ni. The supplier of the plate did not report any vanadium present as received. Yet there appears to be trace amounts detected in the plate. One reason this could be happening is the VC is diffusing down into the plate as the coating is being deposited.

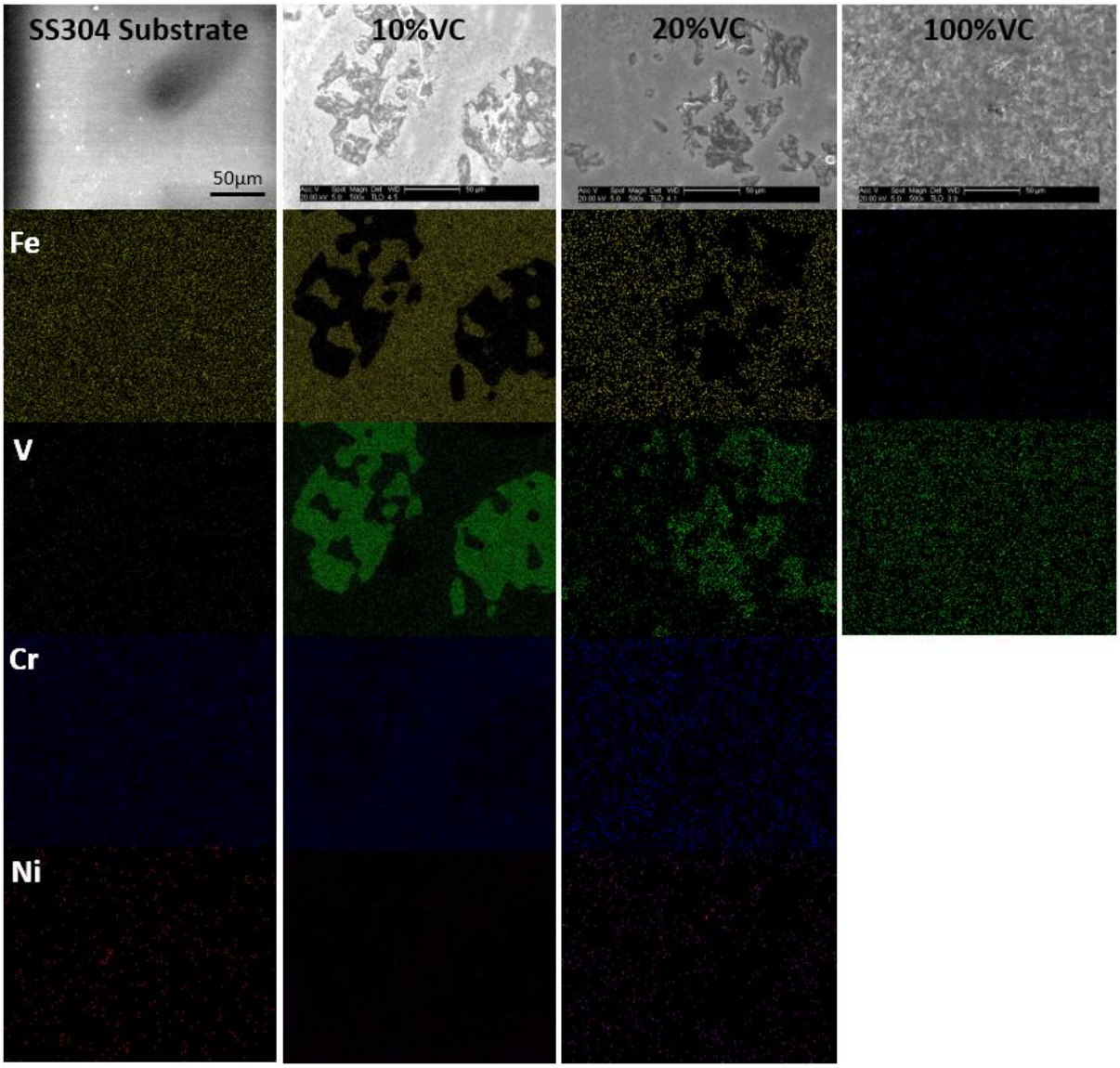

Figure 3.8: EDS mapping of Fe and V on the SS304, 10%VC, 20%VC, and 100%VC

The 10%VC image is placed over one of the VC precipitates. By comparing the iron and vanadium maps, it clearly shows the precipitate is VC with no iron present. Though faint, by close inspection of the chromium map, it can be seen that the areas around the precipitate have a higher density of Cr than in the precipitate. The Cr present in the precipitate suggest the Cr bonded with some of the VC, or at least diffused into it. VC was still present outside of the precipitate confirming the VC had dissolved into the metal matrix. The 20% VC showed the same trend as

the 10%VC with more vanadium surrounding the precipitate. This makes sense considering the higher VC amount.

The 100%VC only has the scans for iron and vanadium. This is because no Cr or Ni was detected. As expected the 100%VC had primarily vanadium and only trace amounts of iron. The trace amounts of iron could be residual SS304 left in the feeder tubes and was being deposited as an impurity. SS304 dust in the chamber could also have been mixing with the powder being deposited leaving impurities. Overall EDS concludes the VC is dissolving in the grain boundaries and the precipitates being seen are primarily VC with possibly trace amounts of Cr.

3.3.5 Hardness Measurements

Average hardness of the top surface of the coatings are reported in **Fig 3.9** and **Table 3.3**. The average of the top surface is only reported because this is the most critical hardness of the of the coatings. It can be seen that the hardness did increase with increasing carbide content. The 5%VC raised the hardness by 67.5-86.8$HV_{0.1}$, 10%VC by 79.5-151.7$HV_{0.1}$, and 20%VC by 92.9-150.9$HV_{0.1}$ (Δ No LP - Δ LP). The laser pass had a much greater impact on the increase in hardness than the addition of more VC after 5%VC. For the non-laser pass samples, the hardness had a 67.5$HV_{0.1}$ increase when 5%VC was added. The addition of 10% and 20% only yielded a 12$HV_{0.1}$ and 13.4$HV_{0.1}$ rise on average, respectively. Those are the on average values, where in reality there was no real difference between the 10% and 20% when standard deviation is taken into consideration. When considering the laser pass, the 5%VC addition increased the hardness by 86.8$HV_{0.1}$ when compared to the laser passed SS304. That is 19.3$HV_{0.1}$ more than the 5% addition without the laser pass. Next the 10%VC 1LP sample increased the hardness by 64.9$HV_{0.1}$. 52.9$HV_{0.1}$ larger increase than the difference between the 5% and 10% non-laser pass samples. Like the non-laser pass, the 20%VC showed no change in hardness compared to the 10%, besides

it had a slightly larger standard deviation. The higher standard deviation is due to the increase in VC precipitates in the coatings. Depending on how close the measurement was taken next to a precipitate, the hardness would drastically increase or decrease. For consistency, measurements were taken away from carbides to only get the saturated matrix readings.

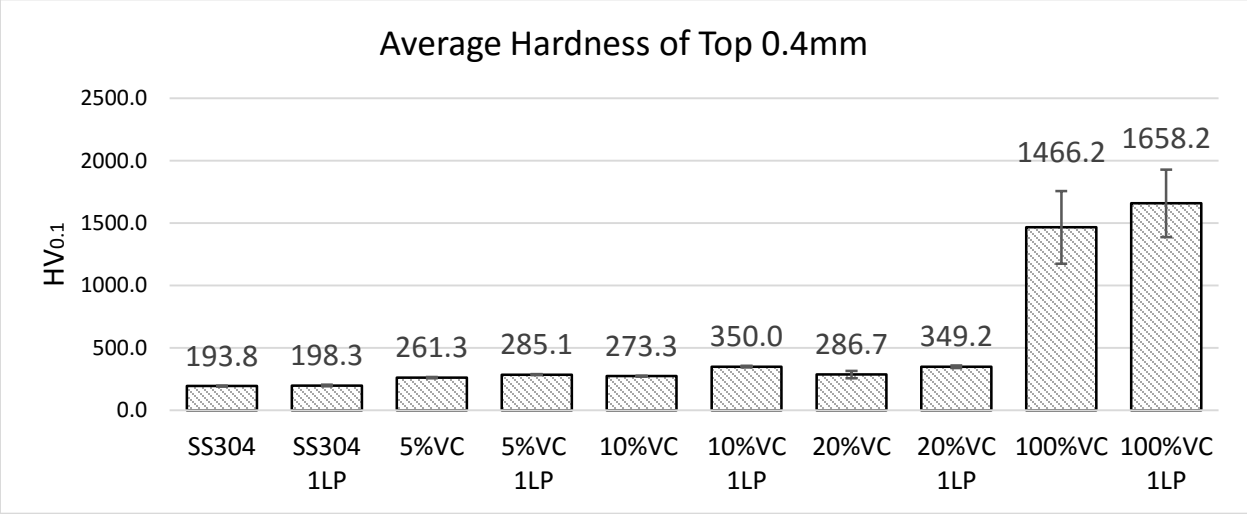

Figure 3.9: Bar graph of coating hardness

Table 3.3

Average hardness of Top 0.4mm		
Sample	**Average Hardness**	**STD**
SS304	193.8	4.03
SS304 1LP	198.3	6.85
5%VC	261.3	4.46
5%VC 1LP	285.1	4.13
10%VC	273.3	4.40
10%VC 1LP	350.0	5.91
20%VC	286.7	29.57
20%VC 1LP	349.2	10.08
100%VC	1466.2	290.6
100%VC 1LP	1658.2	270.3

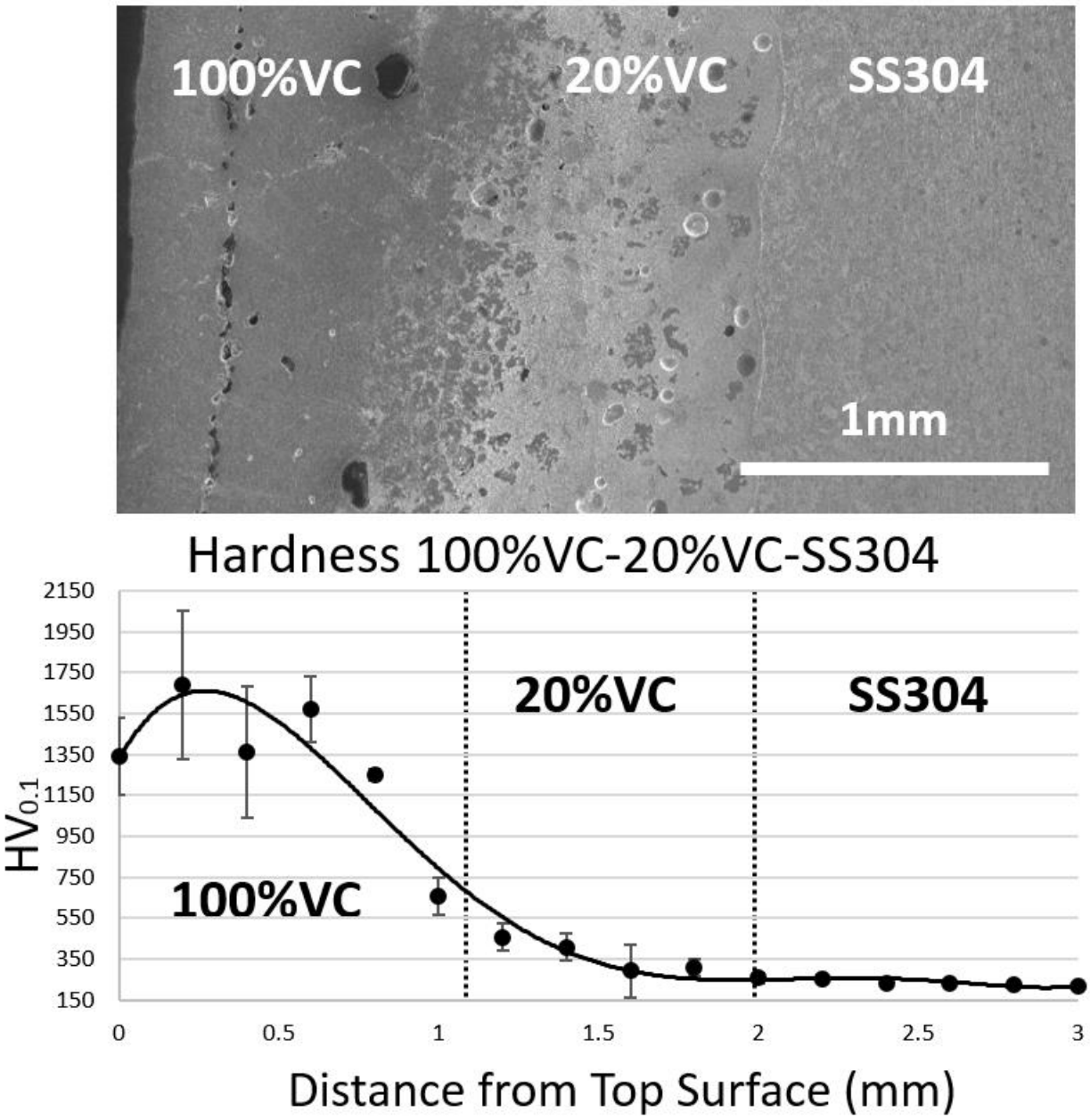

Figure 3.10: Hardness depth profile of 100%VC-20%VC-SS304 coating

The 100%VC increased hardness by a very large amount compared to the other coatings. The average hardness at the top was 1466.2$HV_{0.1}$ and 1658.22$HV_{0.1}$ of the non-laser pass and laser pass samples respectively. That is a 1272.4-1459.9$HV_{0.1}$ increase. The standard deviation was very high at 290.6$HV_{0.1}$ and 270.3 though. This is due to the microporous areas and cracking. Even with a high standard deviation, the VC still exhibits very high hardness relative to the base

coatings. **Fig 3.10** is an image of the hardness depth profile of the 100%VC-20%VC-SS304 coating. The hardness at the top is very high with a lot of variability. Between 0.8mm and 1mm is the interface between the 100%VC and the 20%VC. Between those two points there is a sharp drop in hardness. Around 1.4mm the coatings were fully 20%VC and the readings were close to that of the data from before. Then once the substrate was reached the measurement became uniform and leveled out.

3.3.6 Wear Studies

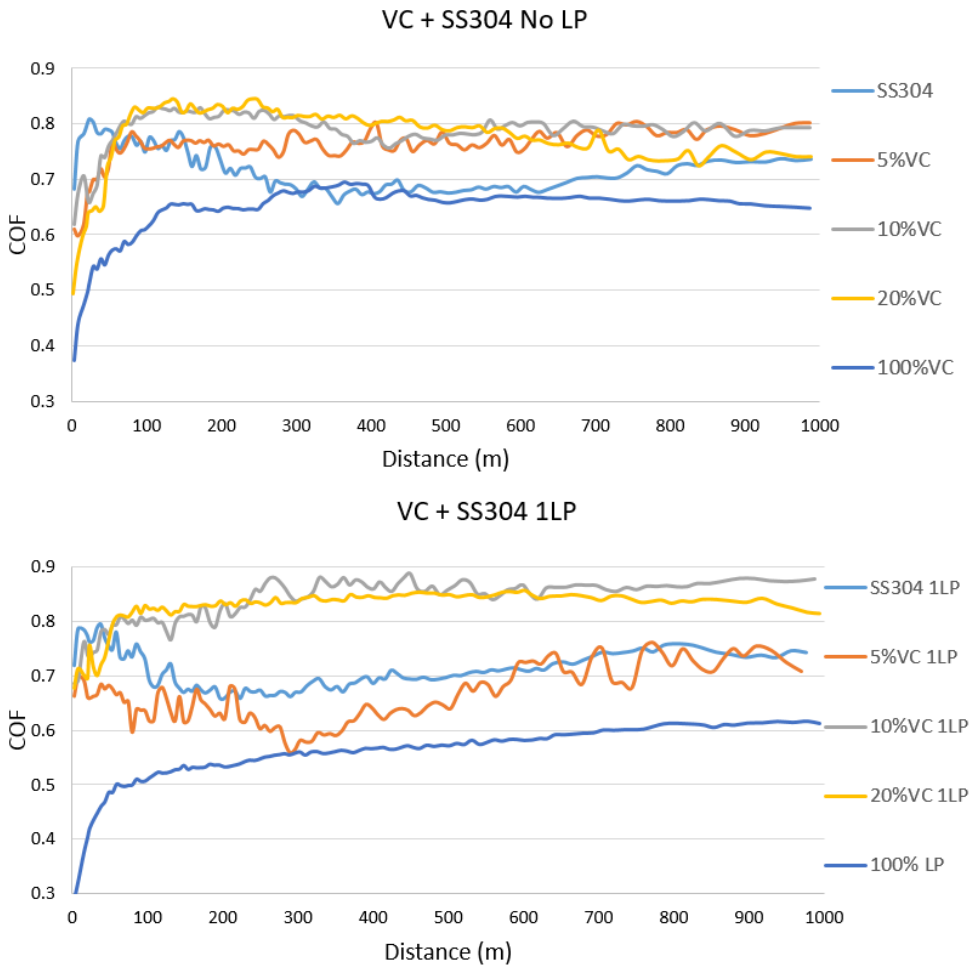

Figure 3.11: Coefficient of Friction plots for 1km tests

Fig. 3.11 shows two plots of the COF of the coatings during the 1km wear test. The top plot shoes the samples without a laser pass and the bottom with. The SS304 did as expected of

most metals and had a sharp rise in COF right at the beginning. This happens as the wear track begins to develop and the surfaces begin to become rough as material is worn away. Next the COF begins to drop as the wear track begins to develop and the ball and track form into the same shape of contact. Then as time goes on the COF curve becomes steady and has fewer fluctuations due to the ball and track being formed to each other. Both of the SS304 coatings followed this trend which can be seen in the plots.

Observing the non-laser pass samples, it would appear the addition of VC to stainless steel did increase the COF. All mixture coatings followed the same trend as the SS304. The 20%VC samples seemed to be decreasing slightly as the distance increased. The laser pass mixture samples seemed to follow the same trend, with the exception of the 5%VC. It had a lower COF than the SS304 until~600m when they became approximately the same. Though it had a low COF, it also had a large degree of change, and varied a lot during the test. The 100%VC samples both caused a decrease in COF compared to the SS304. The non-laser pass started lower than the SS304, then it rose to be about the same, and after 700m started to decrease below it again. The laser pass samples had a steady increase but still was substantially below the SS304 by roughly 0.1.

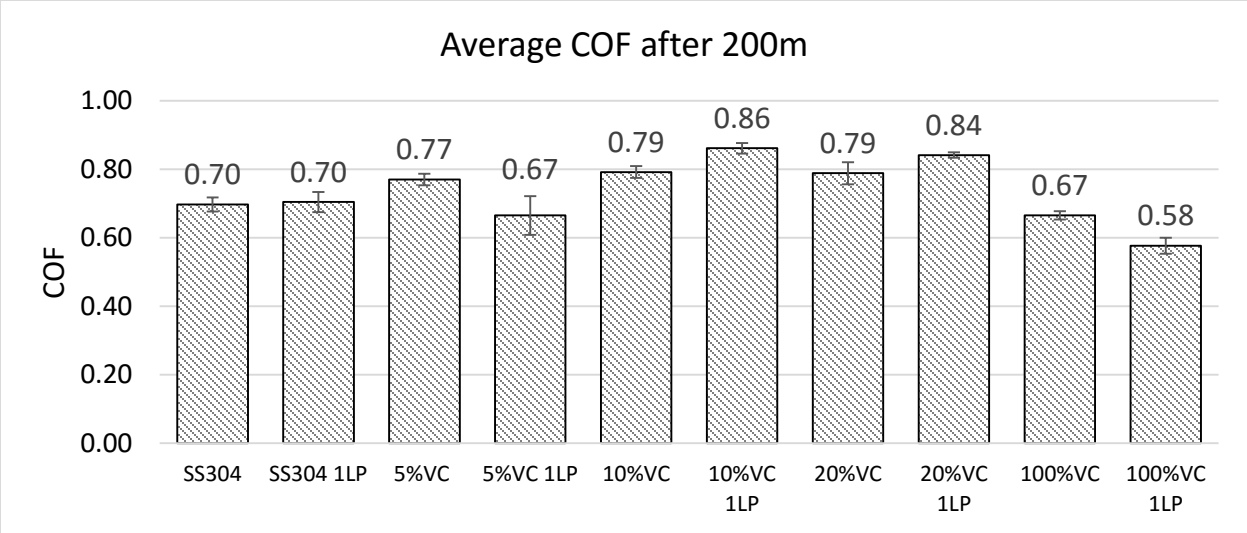

Figure 3.12: Bar graph of Average COF values after 200m

Table 3.4

Average COF after 200m of Wear Test

Samples	Avg. COF	STD
SS304	0.70	0.020
SS304 1LP	0.70	0.029
5%VC	0.77	0.017
5%VC 1LP	0.67	0.057
10%VC	0.79	0.017
10%VC 1LP	0.86	0.016
20%VC	0.79	0.032
20%VC 1LP	0.84	0.008
100%VC	0.67	0.012
100%VC 1LP	0.58	0.023

Fig 3.12 shows a bar graph of the average COF after 200m. **Table 3.4** has the values of the average COF and standard deviation (STD). The average was taken after this distance because as mentioned earlier, this is where the ball and track began to form to each other and the COF became steady. It can be seen the laser pass did not change the overall COF of the SS304. It in fact increased the standard deviation value slightly. As mentioned before, the COF increased with the addition of the carbides with the exception of the 5%VC laser pass. Yet it can be seen there is a large STD that puts it in the range of the SS304 coatings. For the 10%VC and 20%VC samples, the COF increased when compared to their respective non-laser pass counterparts. It also should be noted the 10%VC and 20%VC samples had almost the exact same COF. The 100%VC non-laser pass coating had the same COF as the 5%VC laser pass, but a much lower standard deviation. Overall the 100%VC with a laser pass had the lowest with a 0.58, which is 0.12 less than the SS304.

After the wear test the average wear rate was calculated from the width of the wear track. **Figure 3.13** and **table 3.5** show the results from these calculations. It can be seen the addition of VC significantly decreased the wear rate of the coatings. The SS304 samples were around 4.00E-04 and all the carbide samples were below 1.00E-04 with the exception of 10%VC laser pass. An issue was found when calculating the wear rate during this study which makes these results difficult to compare. The method used the width of the wear track to calculate the cross sectional area of the ball that would be below the surface, and multiplied it by the width of the wear track to attain the volume lost. The calculation was all based on the assumption the ball retained its original radius and geometry. After inspecting the wear tracks, this assumption proved to not be true.

When observing the wear tracks it was found the balls underwent a considerable amount of wear, causing the contacting surface to become flat. This broke the first assumption of the ball retaining its geometry, which meant the wear track did not have a perfect spherical shape. Therefore, the calculation of the volume loss and subsequent wear rate have a considerable amount of error. **Fig. 3.14** is an optical image of some of the laser pass samples wear tracks at 5x,

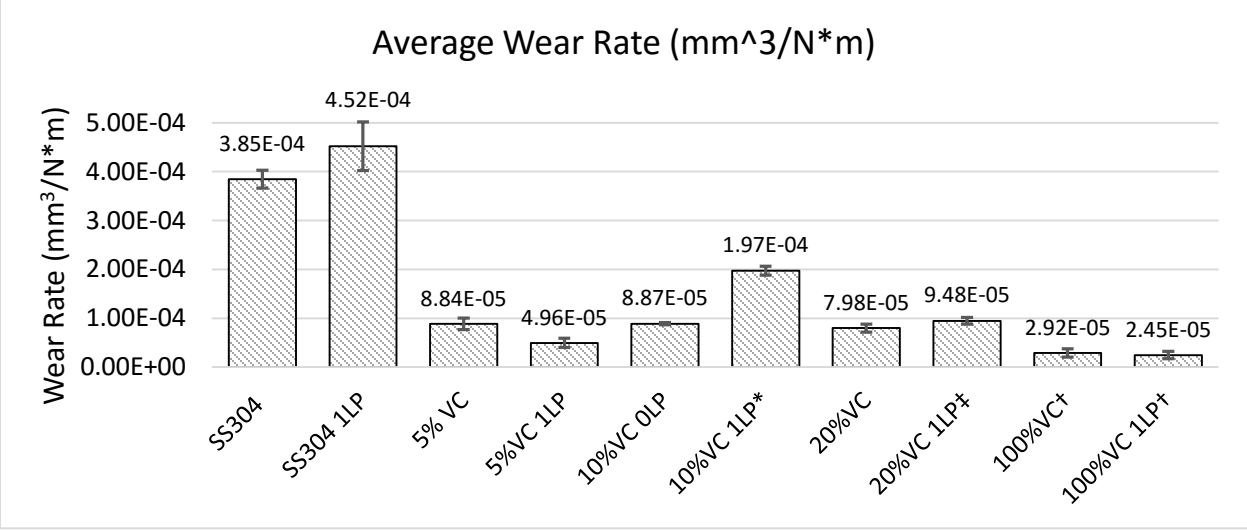

Figure 3.13: Bar graph of wear rate of coating based on width of wear track

* Width of wear track may not be accurate measurement because wear ball wore away. Though the track has a larger width, it is believed less material was lost.

† 100%VC looked as though little to know material was lost, and the wear track was just residue from the Si_3N_4 ball on the surface

‡ Due to grinding errors it is believed too much of the laser pass coating was grinded down, leaving only the porous coating that was unaffected by the laser pass left. This made the wear rate closer to that of the non-laser pass sample

Table 3.5

Wear Rate Calculations of Coatings

Sample	Wear Rate ($mm^3/N*m$)	STD
SS304	3.85E-04	1.84E-05
SS304 1LP	4.52E-04	4.99E-05
5% VC	8.84E-05	1.19E-05
5%VC 1LP	4.96E-05	9.19E-06
10%VC 0LP	4.51E-05	2.48E-06
10%VC 1LP*	7.60E-05	9.19E-06
20%VC	7.98E-05	8.01E-06
20%VC 1LP	9.48E-05	6.83E-06
100%VC*	2.92E-05	8.52E-06
100%VC 1LP*	2.45E-05	7.53E-06

10x, and the wear ball at 5x. It can be seen that the wear balls of all the carbide samples have a flat surface that was contacting the coatings. This means the ball was wearing away indicating the coating had a considerable amount of wear resistance or was more abrasive as the COF data would suggest. The SS304 ball retained a spherical shape, but by using Solidworks™ to measure the wear surface, it was found the ball had a larger radius than the original. This means the calculation for all the samples were larger than what they really were, especially the wear tracks where the ball had a flat surface. It was found that all the carbide samples had a flat surface on the wear ball and the SS304 both retained spherical shape.

This makes comparing the wear rate trends between the carbide samples with the current data inaccurate. Unless a more accurate method that takes into consideration the geometry of the

ball is used, the only thing that can be taken away from the quantitative data is the carbides did significantly reduce the wear rate. This claim is valid because they each had a flat face on the wear ball, which means the calculation is over estimating the amount of volume that is lost from the track. Likewise, the calculation is also overestimating the SS304 wear volume, but because it still has a spherical surface, not as much as the balls with the flat surface are being over calculated. Since all the wear volumes are being over estimated, and the VC coatings are still roughly 83% less that the SS304, it can be claimed that the addition of VC significantly increases wear resistance of the coating.

This also makes sense by visual inspection. **Fig 3.14A** shows the SS304 wear track which is much wider than all the others. It has an oval shape, indicating the wear ball had dropped into the material farther than the other tracks. The 5%VC sample has a much smaller wear track with an average width and resulting wear rate that is 89% less than the SS304. The wear tack does not seem as developed as the SS304 based on the fact there is a center area that seems much

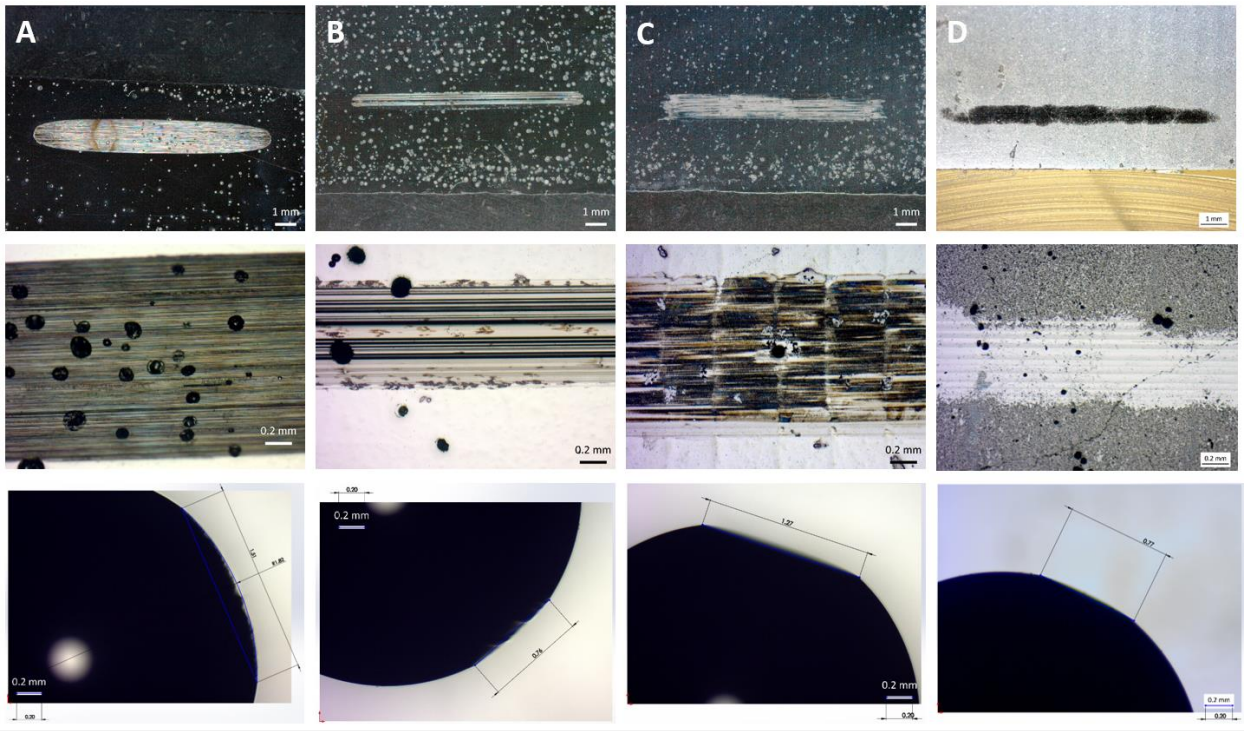

Figure 3.14: Images of wear tracks of laser pass samples and wear ball of (A) Wear track (B) 5%VC (C) 10%VC (D) 100%VC

smoother and does not have the wear lines as seen on the sides of the track and in the SS304. The 10%VC sample has a higher wear rate calculation than the 5%VC, but it is obvious by visual inspection this is not true. The flat spot on the ball measured to be 1.27mm across and the width, and the width of the wear track on average was 1.20mm. This means the flat spot was larger than the area that marked the surface of the 10%VC sample. Based on this and by clear visual inspection, the wear track is just scratches on the surfaces and in no way has an elliptical cross section. Therefore, the wear rate calculation is extremely overestimated, and the 10%VC laser pass sample is less than the 5%VC sample.

The 100%VC sample's wear track is more of a smudge than a wear track. There is a visible mark where the wear ball made contact but little to no material was lost. This can be seen in the 10x image where the track hasn't even begun to make a continuous pattern. An interesting thing

that happened is the wear ball did not lose as much material as it did in the 10%VC test. This is believed to be because the COF was much lower in the 100%VC than in the 10%VC. The Si_3N_4 slid with much less resistance on the 100%VC, therefore not damaging the coating or the ball as much as the 10%VC sample. This is most likely the reason why not much material was lost from the 5%VC ball either. It also had a very low COF.

3.3.7 Abrasive Water Tests

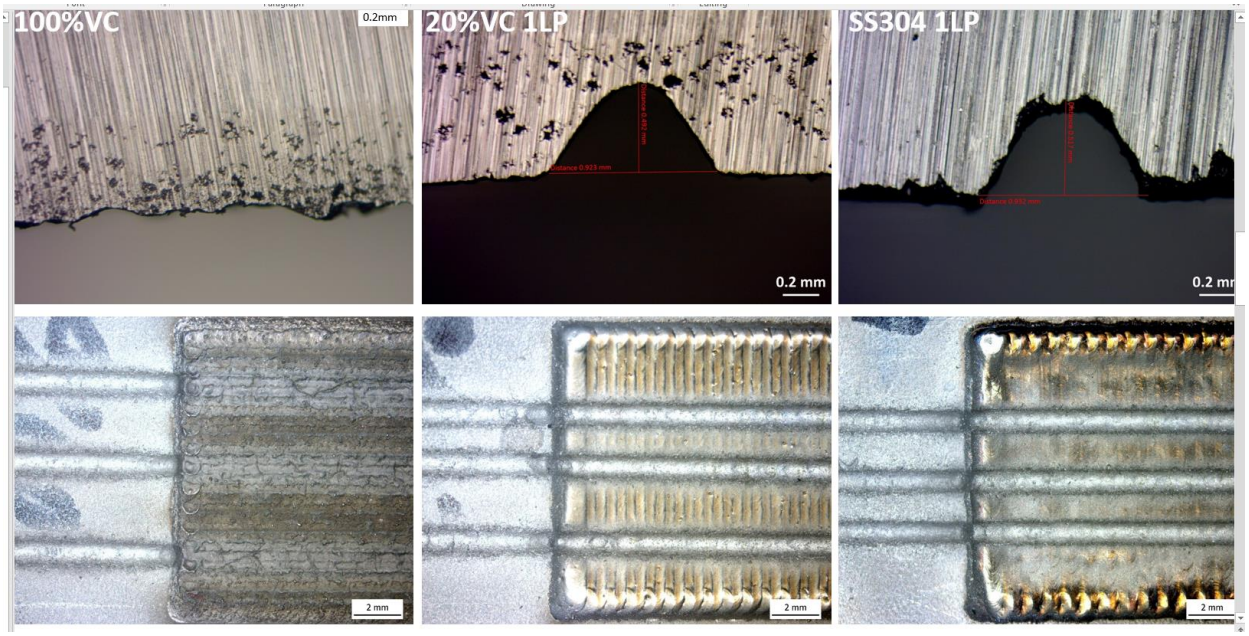

Figure 3.15: Cross section and top images of abrasive water test of coatings

Fig 3.15 shows an image of the cross section and top of the coatings after the abrasive water test. The 20%VC and the SS304 both had considerable material. Both had roughly a 1mm width cut that penetrated 0.5mm. The difference between the two is negligible. It seems the cut was much cleaner through the 20%VC because the cross section has very fine continuous edges. The SS304 seems to have a lot of rough variation. But nothing can really be concluded from this information. The most notable thing is the 100%VC coating had no noticeable damage occur. The water jet is a very aggressive cutting process that easily removes material form the SS304. Yet it

only changed the surface finish of the 100%VC coating. This is quite impressive and shows the 100%VC is a very protective coating that could withstand many forces that steel would erode away to easily to.

3.3.8 Building of Gradient Cylinder

Figure 3.16: (Top) Image of machined cylinder and as built cylinder. (Bottom) Machined gradient cylinder.

To show that this process could be used to add filler material back to damaged parts, a gradient cylinder was made using LENS. **Fig 3.16** shows two cylinders. One has been machined, and the other hasn't They are both the same compositions though. It consists of 20 layers of 10%VC, 20 layers of 20%VC, and 5 layers of 100%VC. The cylinder built well with the exception of the surface finish of the 20%VC. **Fig 3.16** top image shows the before machined surface finish.

It has some small spires protruding from the walls of the 20%VC samples. This was not the case when the coating was being deposited, only when added to the 10%VC. This could be due to the state of the machine at the time, since 100%VC had been deposited before. Possibly residual powder was left in the piping or was stuck in the delivery system. This has been known to happen with carbides and disrupt the powder flow. When the powder flow is disrupted it can cause hatches to grow in odd directions. The cylinder exhibited its ability to be machined except for the 100%VC coating. VC is a brittle material and this cracking was expected, and broke off large portions as brittle materials do. This cylinder shows LENS could add material back to stainless steel parts, which would then give them the added protection of high vanadium carbide SS304, and a very protective coating of 100%VC on the surface.

3.4 Discussion

3.4.0 Microstructural Characterization

The results showed that the VC agglomerated on the grain boundaries, but it also integrated into the grains. VC has a solubility limit temperature from 1100˚C to 1150˚C in austenite[23]. The melting point of SS304 is 1399˚C to 1454˚C[24]. Since the LENS melted the SS304, the temperature was well above the solubility temperature, and some of the VC dissolved in the metal matrix. In the past when 100%VC was deposited by a laser, there was a high amount of substitution of iron in a α-Fe system[19]. Being that this is γ-Fe the diffusion rates most certainly will be different.

The VC is residing on the grain boundaries could be for two different reasons. One is the matrix could have been fully saturated with VC so no more could dissolve into the grains. With nowhere else to go it precipitated on the grain boundaries. The other reason could be the melt pool solidified so fast the VC did not have time to dissolve in the metal matrix. If the second reason were the case though, more time for diffusion would cause the VC to dissolve into the grains. Yet

by observing the laser pass microstructures, we see VC is still present on the grain boundaries. This means it was more likely the first assumption was correct.

The question of whether the carbides on the grain boundaries was only VC is difficult to answer with full confidence. The EDS, XRD, and fact a high amount of VC was added to the coating confirms the carbides were mostly comprised of VC. There is a possibility the VC could be bonding with the chromium and making complex carbides. EDS shows there is some readings of chromium on the precipitate. This could indicate the Cr is a part of the carbide, or it is just Cr being read from underneath the precipitate in the bulk material. The XRD reported possibly the presence of Cr_3C_2 or Cr_7C_3 and Cr bonding with VC has been seen in earlier studies[23]. It has also been reported that in nitrogen, austenitic SS can form intermetallic phases, carbides, and nitrides at high temperatures[25]. Since the substrate did have trace amount of nitrogen, this could be taking place with the Cr, V, C, and possibly N. It seems unlikely though. Since the peak only appears with 100%VC and little to no chromium is present to bond with the carbon at the surface. Also no other peaks for chromium carbides are present. In the past no complex carbides and Fe-V compounds were detected when added to AISI 1045 using the same method[19]. In other studies VC did bond with chromium when using thermal diffusion to apply a coating[21,23]. The differences in the bonding methods between the studies does not give a clear conclusion. Based on the EDS and XRD it seems the VC did not bond with other elements, and the carbides present are almost all pure VC.

As more carbides were added to the microstructure it seems the grains did become finer. The broadening of the γ-Fe peaks indicates the grains are becoming smaller. The VC could be doing this by inhibiting the grain growth of the SS304. Past research has shown that microalloy additions in γ – stainless steel impede grain growth because of finely dispersed carbides[16]. As more

VC was added to the coating, the VC became more widely dispersed, which inhibited grain growth even more. This is why the peaks on the XRD became broader as VC content increased. These small grains are ideal for the coating because they are a well-known way to increase strength and hardness of a metal according to the Hall-Petch formula[26]. Also the VC particles act finely distributed strengthening particles. Having this kind of particle present has been shown to be an effective way to improve creep strength steels[23]. Overall the effect the VC has on the grain structure is ideal for a protective coating.

3.4.1 Interface of Coatings

Microstructural images showed good bonding between the substrate and the coating. Past research shows a MMC of VC with low carbon steel Fe 52 has been able to be deposited and make a strong adhesion[14]. This small or highly localized HAZ has been seen before in other systems as well as stainless steel[27,28]. The fact there is no large pores or voids shows the VC does not alter the ability for a coating to bond to the substrate. This means the coating can be applied to current SS304 parts in use and should not have an issue with adhesion. The interface between the 100%VC and 20%VC was much more gradual. This type of dispersion can be seen in other studies where 100%VC was deposited on a AISI 1045 steel[19]. The large carbide precipitates extend into the 20%VC matrix, and the mixture remains heterogeneous and there seems to be no gradient change.

3.4.2 Laser Pass Grain Refinement

The laser pass appeared to give a more homogeneous uniform distribution of VC. This is due the reheating and extended diffusion time the laser pass gives[19]. The solidification rate of the melt pool does not change, so neither does the grain structure or morphology. Since no more

powder is flowing in and integrating itself in the structure, the layer that was being reheated does

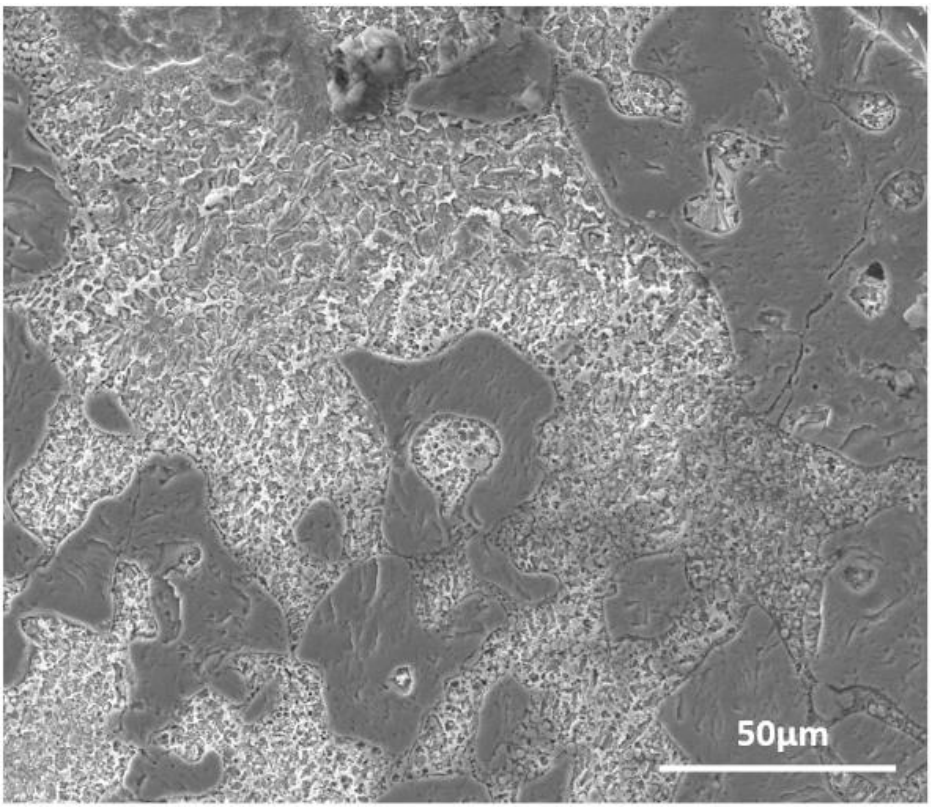

Figure 3.17: Image of Carbides in 20%VC

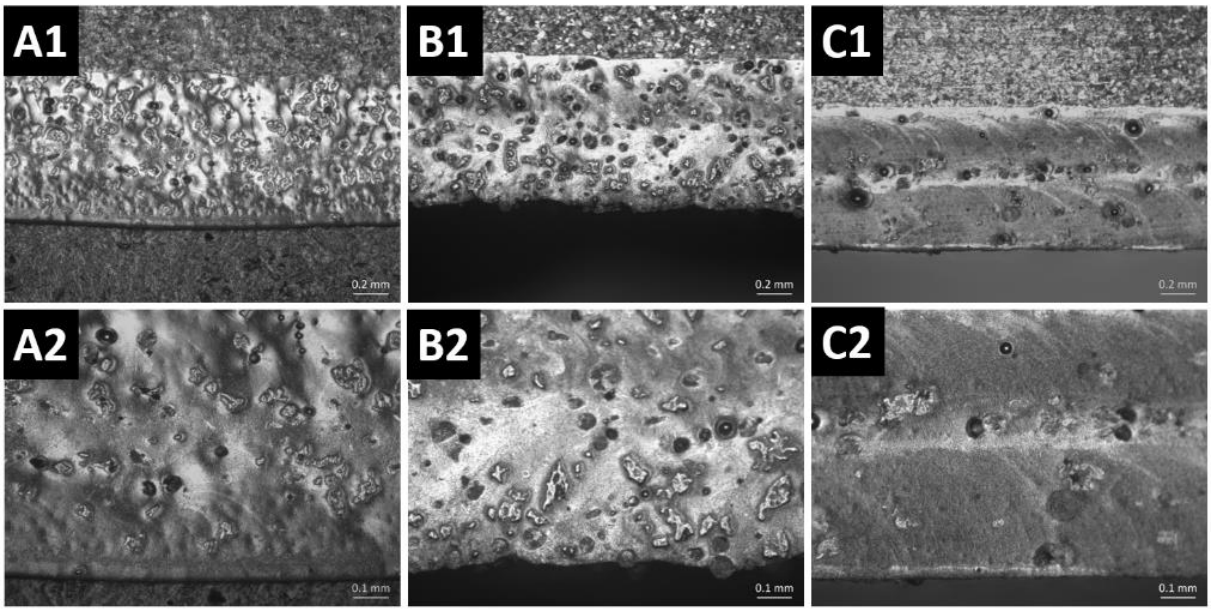

Figure 3.18: Optical images of the 20%VC coatings. (A) 1 laser pass (B) No laser pass (C) Laser pass on both layers (1) 5x magnification (2) 10x magnification

not move a long distance. For this reason, when it is given the added diffusion time, it becomes more homogeneous. **Fig. 3.1** gives more evidence as to why this might be true. When looking at the 20%VC coating in **Fig 3.1A** you can see many dark colored spots dispersed throughout the coatings. These can also be seen in **Fig 3.17**, which is a larger image of the 20%VC-100%VC interface. The dispersed dark areas are large precipitates of VC. **Fig 3.1B** shows the same structure but each layer of the 20%VC sample had a laser pass before the next was deposited. There were significantly fewer carbide precipitates. Most of the remaining ones are near the interface of the first layer on the substrate, and interface of the second on the first. These would be the zones farthest away from the laser pass and would be subject to less heat and subsequent diffusion. For this reason, it can be assumed when given more time for diffusion the VC will dissolve into the matrix and mix more homogeneously, which is proven by the disappearance of the heterogeneous precipitates of VC, and more homogeneous distribution on the grain boundaries.

Another thing the laser pass did was agglomerate the voids. The purpose of the laser pass was to make the coating dense. Yet it appears the coatings with a laser pass are riddled with pores. The pores seem to be away from the HAZ and are larger than the non-laser pass. **Fig 3.1** shows this very clearly with **Fig 3.1A** having many small pores, and **Fig 3.1B** having large pores all over. They are also near interfaces of layers as well. This is because when the layer is heated back up, it allows for not only the VC to diffuse, but also the voids become mobile. It appears the area that fully melts loses most all its porosity as the metal bond and collapses the pores. In the area below the melt zone, the voids do not collapse but agglomerate making large pores. **Fig 3.18** justifies this further by showing the 20%VC sample with a laser pass, no laser pass, and a laser pass on both layers. The coating with one laser pass has a dense layer on top with pores underneath. The non-laser pass is porous throughout the coatings. The coating with a laser pass on each level left two

dense zones on the top of each layer, with pores in-between the interfaces. This means that all porosity could possibly be removed with longer hold times of the laser, or increased power.

3.4.3 Hardness

The added VC increased hardness by lowering the grain size and causing internal stresses in the grain structure. The hardness decreased as it was measured down the depth because of LENS processing. As LENS is building a part, the previous layers deposited and the substrate acts as a heat sink from the layers being deposited. As heat transfers through the part the previously built areas are then annealed. This changes the grain structure and subsequent properties[29]. Though SEM inspection of the grains did not show a noticeable change down the cross section of the coating, very small changes must be taking place that change the properties.

As the amount of VC increased so did the STD of the measurements. This increase in standard deviation is accredited to more precipitates being present as the carbide content increased. It is also why the laser pass standard deviation is less than the non-laser passed standard deviation. As mentioned before, the laser pass allowed for the VC to diffuse into the grains. Since the VC was more homogenously dispersed, it decreased the inconsistency in the hardness.

3.4.4 Abrasive Wear Resistance

Abrasive water tests show the 100%VC had a very high resistance to material loss from abrasive water. All the coating experienced a definitive cut and the 100%VC remained undamaged. An issue with this test is it is very direct and aggressive. For this reason, the difference in abrasive water resistance is unmeasurable unless the difference is very high. Small changes in resistance do not change to amount of material lost to measure large enough difference to make a claim. This is what happened between all the mix test which leaves the results inconclusive. The only thing to take away from them is the coatings have similar abrasive wear resistance, if there is a difference

it cannot be measured from the test. What is known is the mix coatings have a much larger wear resistance and hardness. For this reason, it is believed the abrasive water and cavitation resistance of the coatings should be higher in the mix coatings. The abrasive water test does show the 100%VC definitely has a higher abrasive wear resistance and should serve to better protect components in a hydroelectric generator.

3.4.5 Gradient Coating

LENS was able to produce SS304 coating with different mixture of VC and deposit them to make a gradient cylinder The addition of VC proved to increase the wear resistance and hardness of the coating. The results suggest that the addition of any of these VC coatings should protect a part better than base SS304. From all the test it was clear the 100%VC was the most protective coating. The only issue the 100%VC coating had was it was difficult to build more than a couple layers. Even the deposition of two layers produced a very porous interface. Therefore, it would be difficult and expensive to fix a part that has experience material loss with 100%VC coatings. To overcome this the LENS could deposit SS304 until the missing material is almost replaced, then finish repairing the part with 100%. If the 100% eventually wore away, it would only be SS304 there for protection, and the part would deteriorate as fast as before.

This study has shown that LENS provides another option of adding a gradient fill. By adding mixtures of VC, the hardness and wear resistance increase. Therefore, if LENS was used to repair a part, it could add SS304, then slowly add VC until it reaches the surface where it can apply 100%VC. This increases the protection of the part because if the 100%VC gets damaged, there will still be an even more protective layer underneath. It also is better because it gradually changes properties. **Fig 3.16** shows the 100%VC is brittle and was not able to be machined. This is expected with ceramics, but also means there is a brittle coating on top of a ductile metal. If any

kind of deformation occurs, the 100%VC will crack exposing a weak spot. If the gradient coating is present underneath the VC, it will give better protection if this event occurs than if only SS304 was there. Thereby increasing the longevity of the part. The gradient coating also provides an option to coat parts at less of a cost. If a part does not require a full 100%VC coating, a mixed coating could be used. This would cost much less than applying 100%VC, and still give a lot of added protection to the part.

3.5 Summary

LENS was able to deposit mixed coating of SS304 and VC that exhibited higher hardness and wear resistance than only SS304. It also was able to deposit 100%VC coating and make a gradient coating. Laser processing yielded smaller and more homogenous grains with the VC integrated in the grains and on the grain boundaries. The VC acted as strengthening particles that increased hardness and wear resistance. The addition of a laser pass increased these properties as well as helped densify the coatings. Adhesion to the substrate appeared to be good with a very small heat affected zone. XRD showed the VC inhibited grain growth and produced finer grains. The addition of VC decreased the wear rate of the coating by over 80%. From abrasive water test it was also shown that 100%VC is incredibly resistant to harsh environments that would easily remove material from SS304, and not even harm the coatings. This process could be used to build new parts and apply coatings, or repair damaged ones while simultaneously increasing their resistance to damage in the future.

3.6 References

1. Aghaie-Khafri M, Fazlalipour F. Vanadium carbide coatings on die steel deposited by the thermo-reactive diffusion technique. *J Phys Chem Solids*. 2008;69(10):2465-2470. doi:10.1016/j.jpcs.2008.04.040.
2. Hassanzadeh-tabrizi SA, Hosseini H, Alizadeh S. In situ synthesis of vanadium carbide –

copper nanocomposite by a modified mechanochemical combustion method. *Ceram Int*. 2016:1-4. doi:10.1016/j.ceramint.2016.02.129.

3. Woydt M, Mohrbacher H, Vleugels J, Huang S. Niobium carbide for wear protection – tailoring its properties by processing and stoichiometry. *Met Powder Rep*. 2016;00(00). doi:10.1016/j.mprp.2015.12.010.

4. Shah S V, Dahotre NB. Laser surface-engineered vanadium carbide coating for extended die life. *J Mater Process Technol*. 2002;124(1-2):105-112. doi:10.1016/S0924-0136(02)00109-7.

5. Leunda J, Soriano C, Sanz C, Navas VG. Laser Cladding of Vanadium-Carbide Tool Steels for Die Repair. *Phys Procedia*. 2011;12:345-352. doi:10.1016/j.phpro.2011.03.044.

6. Chicco B, Borbidge W., Summerville E. Experimental study of vanadium carbide and carbonitride coatings. *Mater Sci Eng A*. 1999;266(1-2):62-72. doi:10.1016/S0921-5093(99)00035-0.

7. Plesset BYMS, Ellis AT. On the mechanism of cavitation in centrifugal pumps. *Wear*. 1958;1(4):353. doi:10.1016/0043-1648(58)90042-5.

8. Qiu N, Wang L, Wu S, Likhachev DS. Research on cavitation erosion and wear resistance performance of coatings. *Eng Fail Anal*. 2015;55:208-223. doi:10.1016/j.engfailanal.2015.06.003.

9. Lo KH, Cheng FT, Kwok CT, Man HC. Improvement of cavitation erosion resistance of AISI 316 stainless steel by laser surface alloying using fine WC powder. *Surf Coatings Technol*. 2003;165(3):258-267.

10. Razi S, Madanipour K, Mollabashi M. Optics & Laser Technology Laser surface texturing of 316L stainless steel in air and water : A method for increasing hydrophilicity via direct creation of microstructures. *Opt Laser Technol*. 2016;80:237-246. doi:10.1016/j.optlastec.2015.12.022.

11. Vamsi Krishna B, Bandyopadhyay A. Surface modification of AISI 410 stainless steel using laser engineered net shaping (LENSTM). *Mater Des*. 2009;30(5):1490-1496. doi:10.1016/j.matdes.2008.08.003.

12. Balla VK, Soderlind J, Bose S, Bandyopadhyay A. Microstructure, mechanical and wear properties of laser surface melted Ti6Al4V alloy. *J Mech Behav Biomed Mater*. 2014;32:335-344. doi:10.1016/j.jmbbm.2013.12.001.

13. Yadollahi A, Shamsaei N, Thompson SM, Seely DW. Materials Science & Engineering A Effects of process time interval and heat treatment on the mechanical and microstructural properties of direct laser deposited 316L stainless steel. *Mater Sci Eng A*. 2015;644:171-183. doi:10.1016/j.msea.2015.07.056.

14. Nurminen J, Näkki J, Vuoristo P. Microstructure and properties of hard and wear resistant MMC coatings deposited by laser cladding. *Int J Refract Met Hard Mater*. 2009;27(2):472-478. doi:10.1016/j.ijrmhm.2008.10.008.

15. Ezazi MA, Yusof F, Sarhan AAD, Hamdi M, Shukor A, Fadzil M. Employment of fiber

laser technology to weld austenitic stainless steel 304 l with aluminum alloy 5083 using pre-placed activating flux. *JMADE*. 2015;87:105-123. doi:10.1016/j.matdes.2015.08.014.

16. Shirdel M, Mirzadeh H, Parsa MH. Abnormal grain growth in AISI 304L stainless steel. *Mater Charact*. 2014;97:11-17. doi:10.1016/j.matchar.2014.08.022.

17. Bandyopadhyay A, Dittrick S, Gualtieri T, Wu J, Biomedical WMK, Engineering M. Calcium phosphate – titanium composites for articulating surfaces of load-bearing implants. *J Mech Behav Biomed Mater*. 2016;57:280-288. doi:10.1016/j.jmbbm.2015.11.022.

18. Chakraborty SS, More H, Racherla V, Nath AK. Journal of Materials Processing Technology Modification of bent angle of mechanically formed stainless steel sheets by laser forming. *J Mater Process Tech*. 2015;222:128-141. doi:10.1016/j.jmatprotec.2015.02.044.

19. Herrera Y, Grigorescu I., Ramirez J, Di Rauso C, Staia M. Microstructural characterization of vanadium carbide laser clad coatings. *Surf Coatings Technol*. 1998;108-109:308-311. doi:10.1016/S0257-8972(98)00662-8.

20. Lu J, Sun W, Becker A. Material characterisation and finite element modelling of cyclic plasticity behaviour for 304 stainless steel using a crystal plasticity model. *Int J Mech Sci*. 2016;105:315-329. doi:10.1016/j.ijmecsci.2015.11.024.

21. Ghadi A, Soltanieh M, Saghafian H, Yang ZG. Investigation of chromium and vanadium carbide composite coatings on CK45 steel by Thermal Reactive Diffusion. *Surf Coatings Technol*. 2016;289:1-10. doi:10.1016/j.surfcoat.2016.01.048.

22. Li Q, Lei Y, Fu H. Laser cladding in-situ NbC particle reinforced Fe-based composite coatings with rare earth oxide addition. *Surf Coat Technol*. 2014;239:102-107. doi:10.1016/j.surfcoat.2013.11.026.

23. Park D, Huh M, Jung W, Suh J, Shim J, Lee S. Effect of vanadium addition on the creep resistance of 18Cr9Ni3CuNbN austenitic stainless heat resistant steel. *J Alloys Compd*. 2013;574:532-538. doi:10.1016/j.jallcom.2013.05.106.

24. Chen H, Bi G, Lee BY, Cheng CK. Journal of Materials Processing Technology Laser welding of CP Ti to stainless steel with different temporal pulse shapes. *J Mater Process Tech*. 2016;231:58-65. doi:10.1016/j.jmatprotec.2015.12.016.

25. Kartik B, Veerababu R, Sundararaman M, Satyanarayana DV V. Materials Science & Engineering A Effect of high temperature ageing on microstructure and mechanical properties of a nickel-free high nitrogen austenitic stainless steel. *Mater Sci Eng A*. 2015;642:288-296. doi:10.1016/j.msea.2015.07.011.

26. Zhou W, Xiong J, Wan W, et al. The effect of NbC on mechanical properties and fracture behavior of WC-10Co cemented carbides. *Int J Refract Met Hard Mater*. 2015;50:72-78. doi:10.1016/j.ijrmhm.2014.11.006.

27. Stucker B, Esplin C, Justin D. An Investigation of LENS ® -Deposited Medical-Grade CoCrMo Alloys. 2004:68-79.

28. Griffith ML, Keicher DM, Atwood CL, et al. Free Form Fabrication of Metallic Components Using Laser Engineered Net Shaping (LENS^{TM}). *Proc 7th Solid Free Fabr Symp*. 1996:125-132. doi:10.4028/www.scientific.net/AMR.15-17.175.

29. Griffith M., Schlienger M., Harwell L., et al. Understanding thermal behavior in the LENS process. *Mater Des*. 1999;20(2-3):107-113. doi:10.1016/S0261-3069(99)00016-3.

CHAPTER FOUR

NIOBIUM CARBIDE METAL-CERAMIC COMPOSTIE COATINGS

4.1 Introduction.

NbC has incredible hardness (~ 17-22GPa), high wear resistance, and a high melting temperature (3873˚C)[1,2]. It is a group VB element which are known to make very hard phases in many common alloys[2]. Unlike other carbides between group IV to VI, it has been given little attention compared to titanium, vanadium, and chromium[2]. Similar to VC it has also been researched to be used to strengthen steel for high wear applications[1]. As mentioned in chapter three, materials with high modulus and hardness have been resistant to cavitation and abrasive wear damage[3,4]. For the same reasons as VC, NbC was tested to see if it was an effective additive to make protective metal ceramic composites. It was hypothesized that LENS could deposit a gradient coating of NbC in SS304 to make a metal matrix composite with increased hardness, wear resistance, and abrasive water resistance. The LENS process could then deposit and add these coatings to new parts, or restore damaged ones and add extra protection.

4.2 Materials and Methods

The processing and analysis of this study was the same as the VC, but a little less in depth. There was no 100%, 20%, or gradient cylinders made. When conducting these experiments, the batches of 0%, 5%, and 10% NbC and VC were made at the same time. Preliminary analysis was done and found VC increased hardness more and exhibited slightly higher wear resistance. For this reason, additional samples were built first for VC such as 20%, 100%, samples with a laser pass on every level, and a gradient cylinder. Due to time restrictions this was not done for NbC. Therefore, the only compositions made and tested were 0%, 5%, and 10%. In addition to that EDS

was not conducted on these samples. All other processing and analysis was the same for these samples as the VC. To reduce redundancy, materials and methods will not be written in this chapter. Please refer to chapter three for processing parameters and analysis.

4.2.0 Materials

NbC powder were purchased from American Elements® with 99% purity and a particle size of -100/+270 mesh. 304/304L (SS304) powder was bought from Carpenter® with a powder size of -140/+325 mesh. The composition of the powder is listed in **Table 4.1**. They were then mixed in proportions of 0%, 5%, and 10% wt. Powders were weighed and mixed on a ball mill for one hour to ensure thorough mixing and heterogeneity. For the rest of this paper the coatings will be referred to by their respective NbC content. Coatings were mixed before and not mixed using the LENS to know the exact content of the NbC powder. The LENS could mix the powders by loading the different powders into the different hoppers, then gradually change the feed rate of each one. This way it could make a gradient part by changing the NbCC to SS304 ratio with each layer. If this was done it would be difficult to know the exact amount of NbC in each coating. Therefore, the powders were mixed before for research purposes.

Table 4.1: Chemical Compositions of Materials Used (wt.%)

	C	Cr	Ni	P	Si	Mn	S	N
304/304L Plate	0.022	18.15	8.05	0.033	0.44	1.72	0.0003	0.07
304/30L Powder	0.03	18 to 20	8 to 12	0.045	1	2	0.030	-

4.3 Results

4.3.0 Processing Parameters

In order to integrate the NbC into the stainless steel a high laser power was used. Even though a lower laser power has shown to retain more austenite, it was this study was more focused on melting the NbC into the coating so a higher power was used[5]. Though martensite may be more ideal for hard protective coatings. The coating made were porous as the VC were. As mentioned in chapter 3, it is difficult to optimize parameters of the LENS in these experiments. Since this study was done for initial proof of concept and material property testing, the porous coatings made were deemed satisfactory. (Refer to Ch. 3.3.1 for discussion on difficulties making dense coatings.)

4.3.1 Microstructure

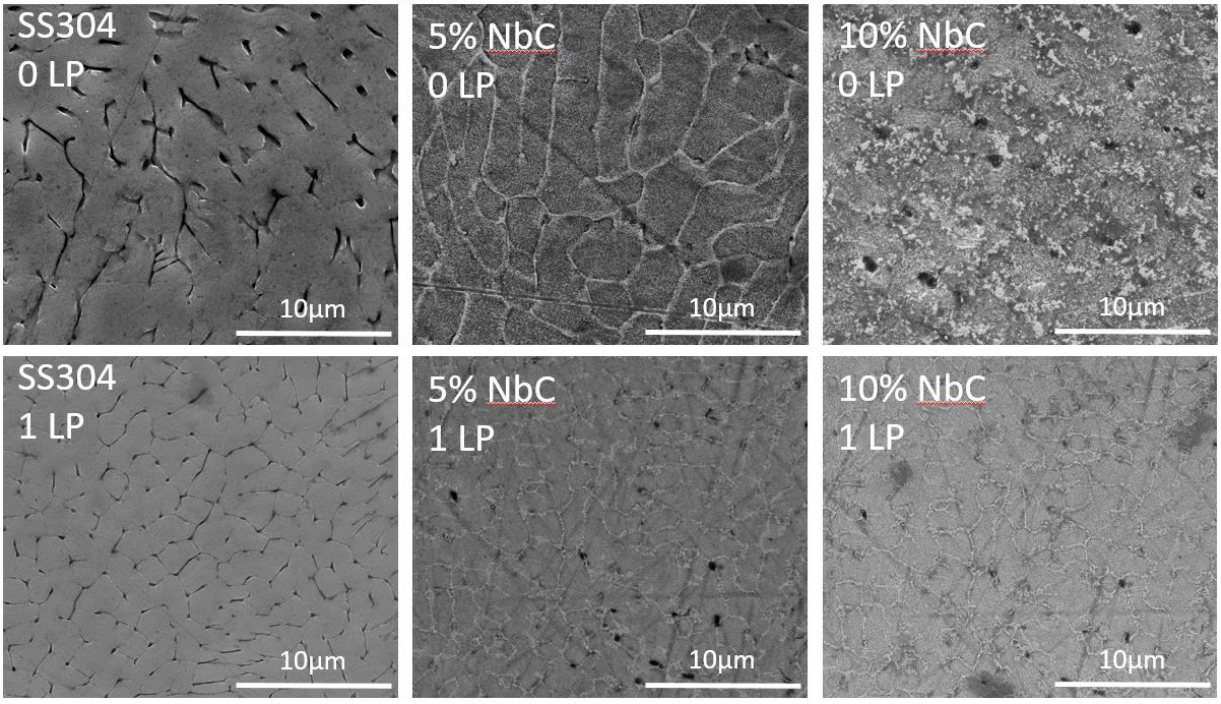

Figure 4.1: Microstructures of SS304 and NbC coatings

Fig 4.1 is an image of all the microstructures of the coatings. LENS processing of SS304 resulted in small grains with more heterogeneous morphology. Fast solidification rates during

LENS processing do not allow for much grain growth, resulting in smaller grains[6,7]. Unlike the VC, there was a significant difference in grain size between the laser pass and non-laser pass samples. Looking at the difference in the 5%NbC this can be easily observed. The grain structures look very similar, with equiaxed morphology and carbides on the grain boundary. The 10%NbC and 5%NbC laser pass samples are almost indistinguishable between each other. The grain structures are the same and it is difficult to tell by observation if one has a higher carbide amount than the other. The real odd grain structure present is the 10%NbC non-laser pass. It has the pits as seen in the other sample that are assumed to be between grains. Yet the carbides are dispersed throughout the metal, not on the grain boundaries. The laser pass appears to have given NbC more diffusion time to agglomerate on the grain boundaries. The substrate and adhesion was almost identical to the VC. It appeared good with no voids or notable weak points. (Refer to Ch.3.3.2 for substrate and adhesion analysis)

The laser pass densified the metal at the surface, lowered the grain size, and allowed for the NbC to agglomerate on the grain boundaries. As mentioned earlier the laser pass made the grains much smaller in all the samples. The laser pass has been known refine, homogenize, and cause dissolution of coarse carbides[5]. This effect can be seen clearly in the 10%NbC sample. The non-laser pass has the carbides spread throughout the grain structure, making any grain structure hard to distinguish. After the laser pass the carbides agglomerated on the grain boundaries and the morphology has changed to that of the 5%NbC laser pass sample. The difference between the non-laser pass samples could be an effect of the increased amount of NbC. It could be inhibiting grain growth as the VC did, but even to a higher extent. The NbC residing on the grin boundaries appears just as the VC did when high vanadium carbide steel was laser deposited[8]. Since they are in the same group of the periodic table, it does not seem unlikely they would act in the same manner. It

is known that carbide dispersion directly affects the strengthening of a coating[9]. Based on this, the higher distribution of carbides should be helping to strengthen the coating.

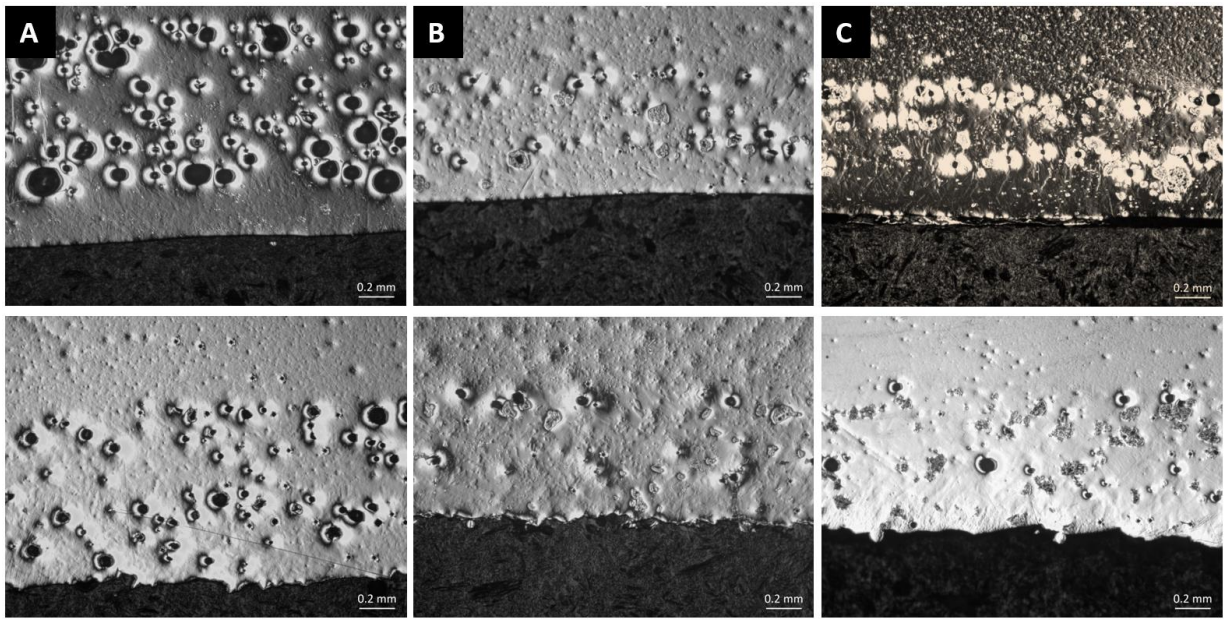

Figure 4.2: Optical images of laser pass coatings at 5x. Top row: Laser pass, Bottom Row: Non-laser pass. (A) SS304 (B) 5%NbC (C) 10%NbC

The laser pass levelled out the top surface that was rough prior. The re-melting of the surface densified and graded out the top layer. **Fig 4.2** show images of the coatings with and without laser pass. Starting with the SS304, the laser pass does densify the top layer roughly 300µm deep. After that the coating becomes very porous, and seems to have the highest porosity of all the coatings. The pores also seem larger in the SS304 laser pass than in the non-laser pass. This is hypothesized to be because the added heat of the laser pass allowed for the pores to agglomerate. Though this ideally would lead to fewer and larger pores. This is not the case in the SS304, and there appears to be a greater number of larger pores than when compared to the non-laser pass samples.

The NbC coatings appear to have less porosity than the SS304, and have a smaller depth. All the coatings were built with the same parameters, but the coating depth was shorter for the

NbC samples. This would suggest the NbC is helping the coating bond more uniformly with little porosity forming. The difference in the laser pass and non-laser pass NbC are less obvious than the SS304. The non-laser pass also has a dense top layer roughly 300μm deep. When closely observing the samples it was found there were large precipitates of carbides in the coatings, and were heterogeneously mixed. This proposes the NbC did not have enough time for diffusion, or the matrix was saturated with the NbC and therefore agglomerated on the grain and in precipitates. The 10%NbC had more of these precipitates as expected due to higher NbC content. As seen in the VC samples, there were fewer precipitates after the laser pass due to increased diffusion time.

4.3.2 XRD Analysis.

XRD analysis shows the NbC has an FCC structure with carbon occupying the interstitial positions[10]. **Fig 4.3** is an XRD plot of the NbC samples. Analysis of the graphs show shows that the SS304 was all γ-Fe. The 3 peaks present were 43.8˚ - γ (111), 51˚ -γ(200), and 74.8˚ - γ(220)[11,12]. The NbC peaks are a 34.6˚ (111), 40.2˚ (200), 58.3˚ (220), and 69.7˚ (311) [9,10,13,14]. The only peak not able to be accounted for was a small one at 46.4˚. It only started to develop on the 10%NbC sample. It could be the bonding of the NbC to an oxygen or chromium. A similar peak close to this was seen in $Ca_4Nb_2O_9$[15]. Though since no calcium was present, this would seem unlikely.

The main peaks slightly shift as NbC was added, but not nearly as much as the VC. NbC only caused a shift of roughly 0.1˚ where VC caused a shift of 0.2˚. This could mean the NbC is not causing as much lattice strain as VC[16]. Also there does not seem to be any noticeable peak broadening. Since the laser pass microstructures look the same, this makes sense that they would also be the same. It would only increase if the grains were getting smaller. Possibly a comparison between the non-laser pass and laser pass would cause a difference.

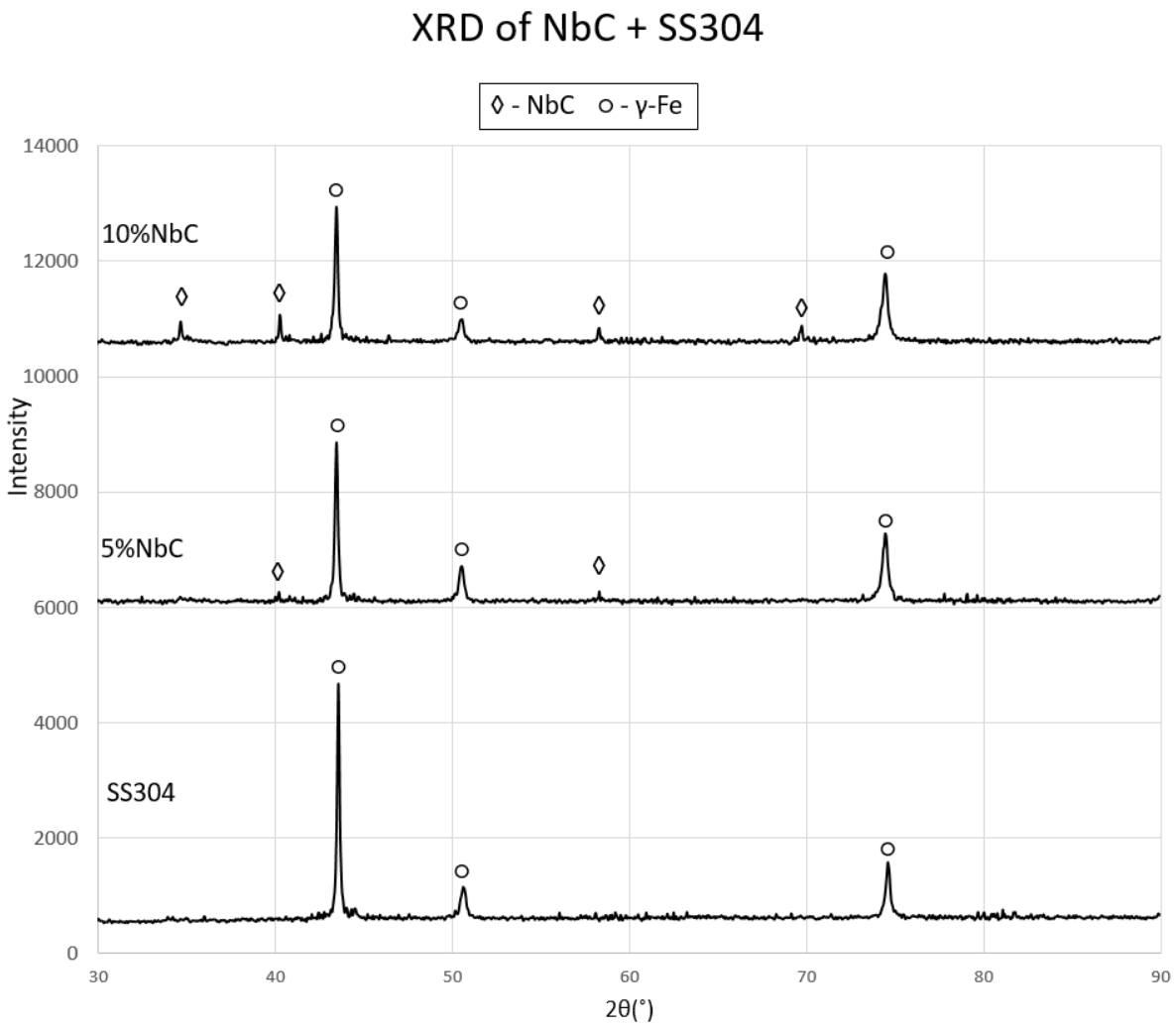

Figure 4.3: XRD plots of all NbC samples

4.3.3 Hardness Measurements

Average hardness of the top surface of the coatings are reported in **Fig 4.4** and **Table 4.2**. The top surface hardness is the most critical and is why it is the only part reported. The trend in the hardness is what would be expected of the laser pass and added NbC. As more NbC is added the hardness increases. Likewise the laser pass densifying the top surface proved to increase hardness as has been see before[5].

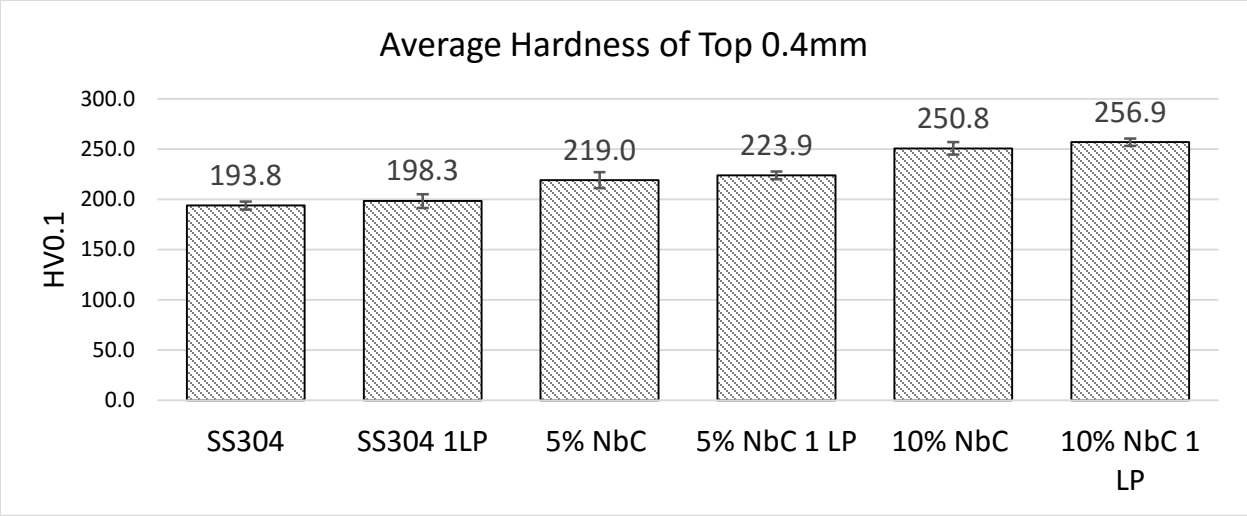

Figure 4.4: Bar graph of coating hardness

Table 4.2

Average Hardness of Top 0.4mm		
Sample	**Average Hardness**	**STD**
SS304	193.8	4.03
SS304 1LP	198.3	6.85
5% NbC	219.0	7.97
5% NbC 1 LP	223.9	3.93
10% NbC	250.8	6.17
10% NbC 1 LP	256.9	3.68

Though the hardness did increase with increasing carbide content it was not a very large change. The 5%NbC raised the hardness by 25.2-25.6$HV_{0.1}$ and 10%NbC by 57.0-58.6$HV_{0.1}$ (Δ No LP - Δ LP). Unlike the VC the laser pass did have a large impact on the increase in hardness. The difference between the laser pass and non-laser pass was quite negligible, though all laser pass increased the hardness slightly. Overall the STD was small on all samples showing consistency in the coating. The only time there were large deviations was when a measurement was taken near a carbide precipitate.

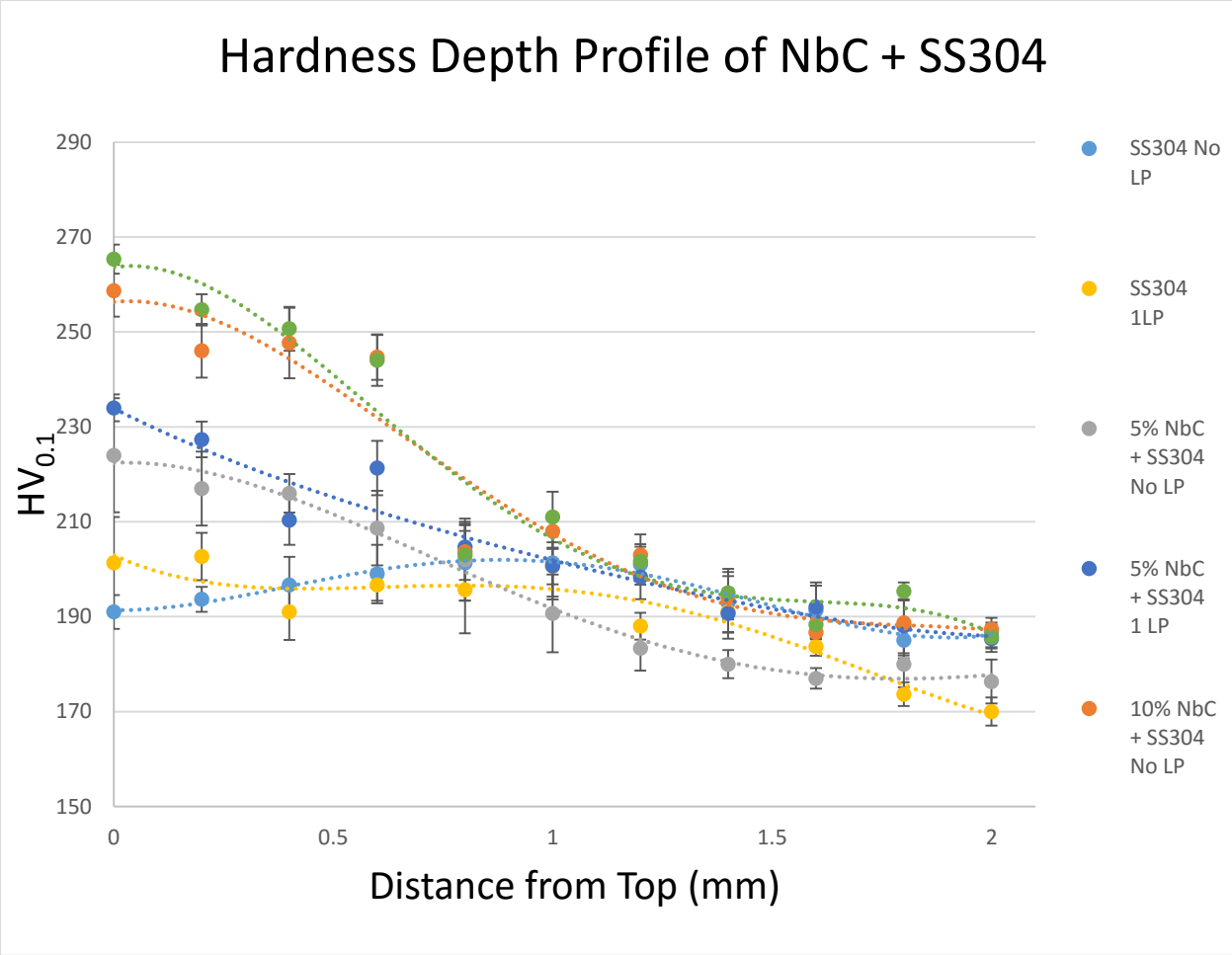

Figure 4.5: Hardness depth profile of NbC samples

Fig 4.5 is an image of the hardness depth profile of all the NbC coatings. The top surface of the coating was the hardest due to the fastest solidification rate. The hardness then decreases down the depth of the coating due to annealing. As each layer is deposited the previous layers of the coating acted as a heat sink. This causes the grains to get some annealing time which lowers the average hardness slightly. It has been mentioned earlier that small changes in the heat history of the layer will change its properties[17]. As the depth increases all coatings return to the same hardness between 190-170$HV_{0.1}$ on the substrate. This profile shows the gradient change of properties from the surface to the substrate. The coating will add extra protection on the surface, then slowly integrate to the bulk properties of the substrate.

4.3.4 Wear Studies

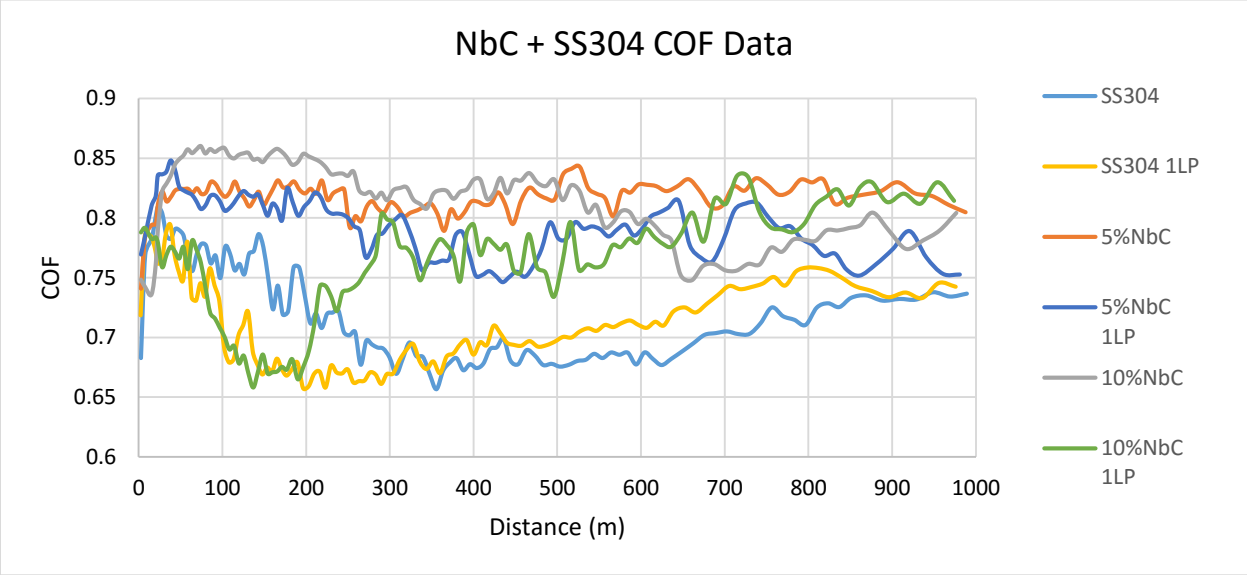

Figure 4.6: Coefficient of Friction plots for 1km tests

Fig. 4.6 shows a plot of The COF over the course of the 1km wear test. All the tracks follow the general progression of a wear track where they start low as the two polished surfaces are interacting. As the material begins to deform, the metal shears, and the surface begins to become rough the COF has a sharp increase. Next the COF begins to drop as the wear track begins to develop and the ball and track form into the same shape of contact. Then as time goes on the COF curve becomes steady and has fewer fluctuations due to the ball and track being formed to each other. Both of the SS304 coatings followed this trend which can be seen in the plots. All the NbC samples followed the same trend besides the 10%NbC 1LP. They all had a COF above the SS304, and remained relatively constant. Over the duration of the test. The 10%NbC had a large drop in the beginning, then after 200m rose to the levels of the other NbC coatings. It almost followed the SS304 1LP exactly under 200m. It ended in the same COF range as the other NbC though.

Fig 4.7 and **table 4.3** show the averages of the COF after 200m. All the coatings were roughly the same and on average 0.1 above the SS304. If the average was take before 200m though, the 10%NbC 1LP would be less. The point of taking it after 200m though is to get the value after a wear track has been developed. The change in the 10%NbC 1LP from being low at 200m increased its STD. Overall the 5%NbC coatings had the lowest STD and most consistency. All the laser pass samples had higher STD due to the change in morphology of the grains. In the beginning the wear track was being developed on the densified layer. Once the track passed this it was on the porous layer with more heterogeneously dispersed carbides. This caused more fluctuations in COF and increased the STD.

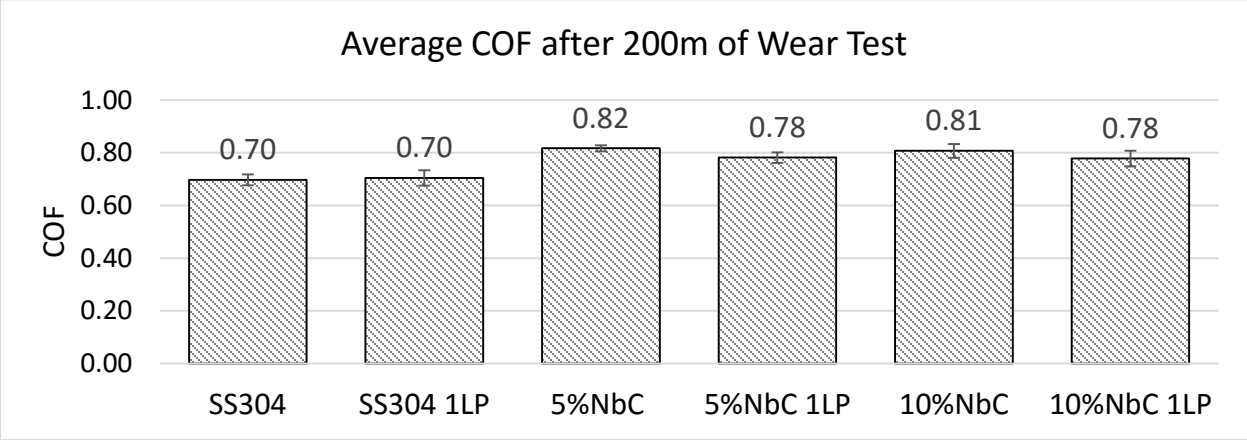

Figure 4.7: Bar graph of Average COF values after 200m

Table 4.3

Average COF after 200m of Wear Test		
Samples	Avg. COF	STD
SS304	0.70	0.020
SS304 1LP	0.70	0.029
5%NbC	0.82	0.011
5%NbC 1LP	0.78	0.020
10%NbC	0.81	0.026
10%NbC 1LP	0.78	0.030

Fig 4.8 and **table 4.4** show the normalized wear rates of the samples. The NbC caused a significant reduction in wear rate. The calculations were subject to the same issue as the VC, and the calculation is subject to some over estimation. **Fig 4.9** is an image of the wear tracks and wear balls of the laser pass samples. It can be seen that the balls of the NbC samples are flat which means the wear rates are over estimated (Refer to Ch. 3.3.7 for discussion on errors with calculation). That being said the NbC lowered the wear rate by 77%. The laser pass also decreased the wear rate in the NbC coatings, but raised it for the SS304.

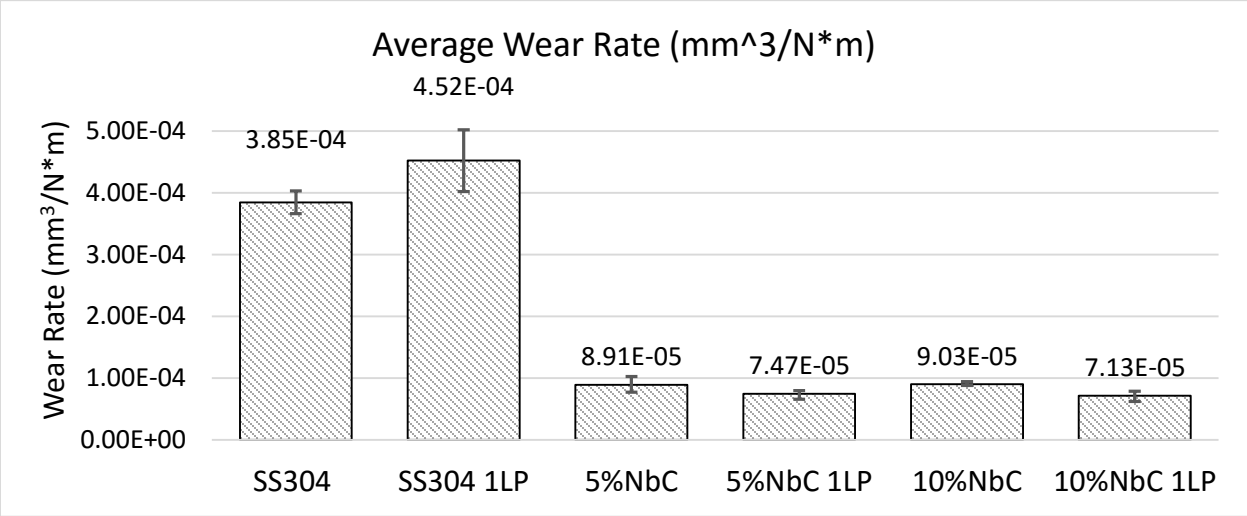

Figure 4.8: Bar graph of wear rate of coating based on width of wear track

Table 4.4

Wear Rate Calculations of Coatings

Sample	Wear Rate (mm^3/N*m)	STD
SS304	3.85E-04	1.84E-05
SS304 1LP	4.52E-04	4.99E-05
5%NbC	8.91E-05	1.35E-05
5%NbC 1LP	7.47E-05	4.99E-06
10%NbC	9.03E-05	3.75E-06
10%NbC 1LP	7.13E-05	7.59E-06

In **Fig 4.9** wear tracks significantly reduce in size from the SS304. There is little difference between the 5%NbC and 10%NbC track widths. There is however a noticeable brown color on the side of the 5%NbC wear track. This was seen on some the VC samples as well. It is believed this is corrosion. It was not present on the 10%NbC coating though. This could suggest the added NbC gives more corrosion resistance. Though it was not seen on the SS304. The wear balls were flat on the carbide samples suggesting more abrasion and wear of the Si_3N_4 ball. This shows the carbide coating has significant wear resistance but also higher abrasion.

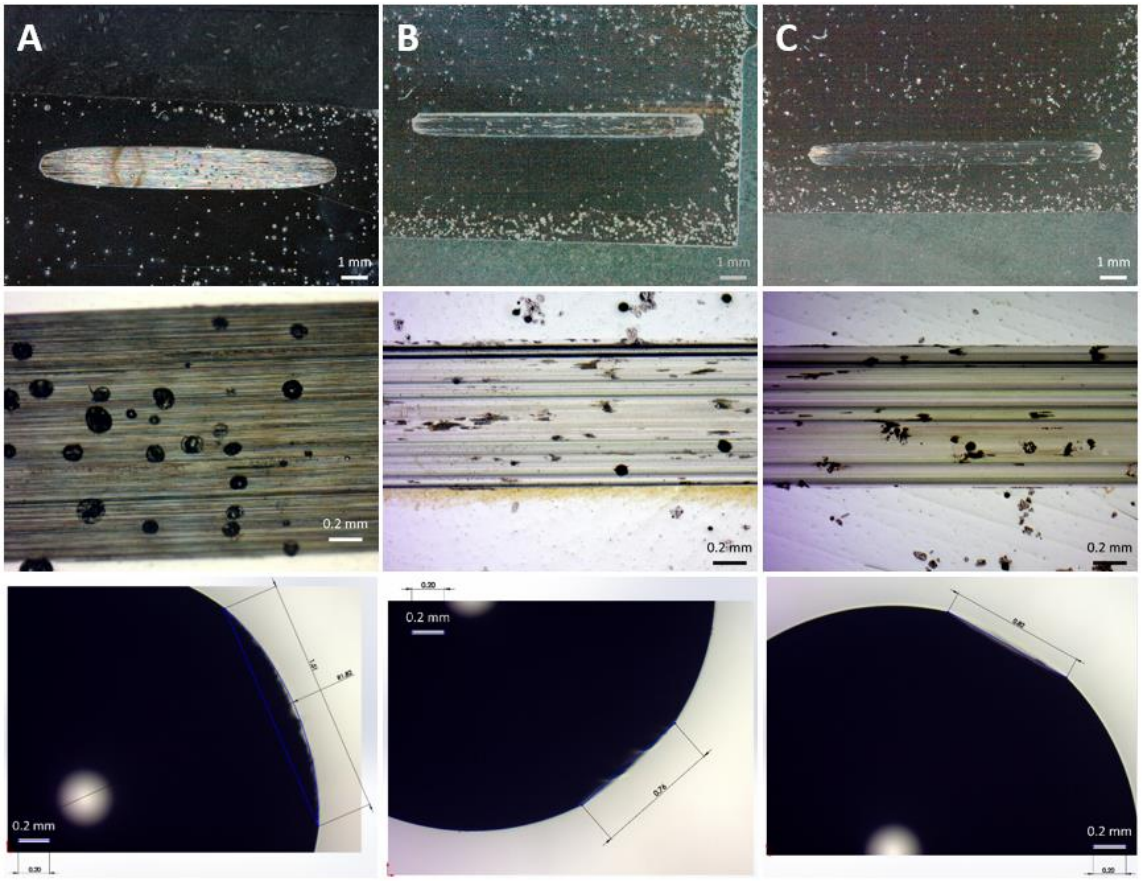

Figure 4.9: Images of wear tracks of laser pass samples and wear ball of (A) Wear track (B) 5%NbC (C) 10%NbC

4.3.5 Abrasive Water Tests

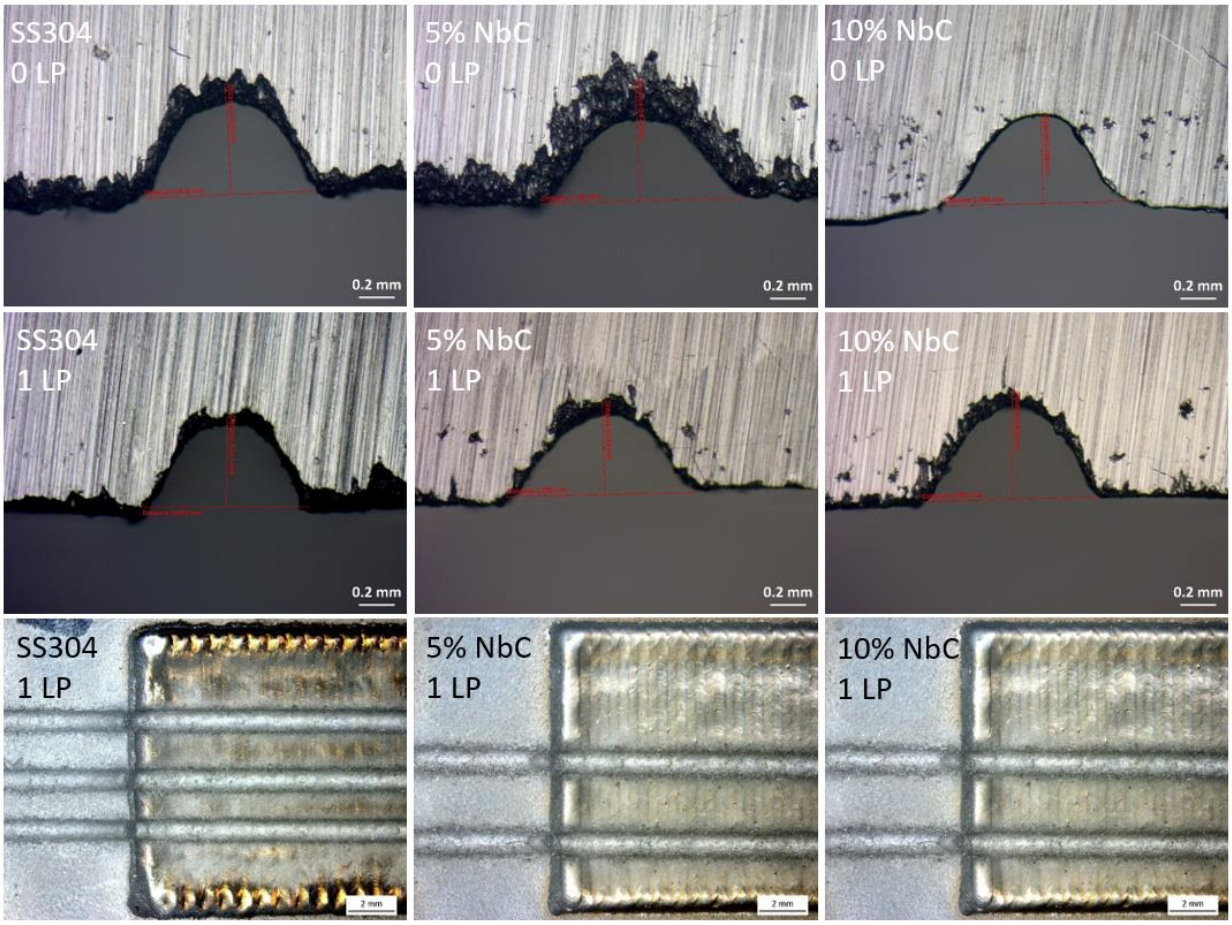

Figure 4.10: Cross section and top images of abrasive water test of coatings

Fig 15 shows an image of the cross section and top of the coatings after the abrasive water test. All the coatings had a considerable amount of material loss. The difference is rather negligible. Due to the aggressive nature of this test, it is difficult to lower the parameters to only cause a slight amount of damage to the coatings. The machine used is made to cut through very large thick materials. It was interesting how some of the cuts have very definitive boundary lines, while others were very rough. There does not seem to be any noticeable pattern to this phenomenon. For example, the non-laser pass 10%NbC has a very clean and definitive boundary line. The 5%NbC though has a very rough and uneven one. This could have happened when grinding the cross

section before imaging. Or it could infer the 10%NbC has a higher resistance to abrasive water because it is not penetrating further into the material as fast. Overall this test proved inconclusive for if the coatings would have better abrasive water resistance.

4.4 Discussion

4.4.0 Microstructure and Mechanical Properties.

SEM images showed the NbC agglomerated on the grain boundaries. This makes sense due to the fact NbC has low solubility in iron compared to other carbides such as tungsten[2]. This does not mean the NbC is not integrated into the grain boundaries, just most likely at lower amounts than the VC. The NbC is then causing stress in the metal as a secondary precipitate, overall increasing the strength, hardness, and wear resistance[18–21]. It was noticed the hardness had less of an increase than in the VC samples. This could mean the NbC do not cause as much lattice strain, therefore not increasing the hardness as much. The NbC added to the grain boundaries is what is causing the small increase in the hardness and significant increase in wear resistance. The precipitates of the NbC were what cause all the increases in mechanical strength.

XRD showed as more NbC was added, more FCC peaks of NbC appeared. In the VC XRD the peaks broadened as more VC was added, inferring finer grain size based on Scherrer[22]. This means there was no grain refinement as more NbC was added. This agrees with the SEM images who's grain size does not appear to change between the laser pass samples.

The laser pass was effective in densifying the surface as well as allowing for extended diffusion of the NbC. The 10%NbC sample is a great example of this and shows how the NbC was dispersed in the structure with no distinguishable order before the laser pass. The material must have solidified so quickly the NbC could not diffuse to the grains. After the laser pass the NbC was situated on the grains with a distinguishable structure similar to the 5%NbC. All the laser pass

samples morphology and size were roughly the same. NbC is known to inhibit grain growth as other carbides do[23]. This could be why the 10%NbC had no noticeable grain structure until the laser pass gave it extended diffusion time. The densification of the top surface proved to increase hardness slightly and lower the wear rate.

The dispersed carbides also increased the COF of the coatings. The NbC precipitates and presence on the grain boundary left small very hard particles dispersed throughout the structure. This made it so as wear occurred and the metal wore down, the carbides were left to interact with the Si_3N_4. This made the wear track like a piece of sand paper with smooth metal as the base and hard NbC placed on top of it. These particles increased abrasion and increased the COF. Likewise, they prevented damage to the underlying material and caused more abrasion on the wear ball. This is ideal for a protective coating. As it wears the NbC is exposed which acts as a defense mechanism. These particles prevent more wear and cause damage to the part acting on it. For this reason, the coating may not be ideal for a bearing where you want both surfaces to remain undamaged. It is however excellent when the application only requires wear resistance to the surface the coating is applied to.

4.4.1 Laser Pass Effect on COF

When looking at the COF 10%NbC sample was the anomaly of the NbC coatings. It first dropped like SS304 laser pass, but then rose back up to the COF of the other NbC coating. This could be due to the laser pass. The laser pass could have dispersed the NbC enough that the particles were more finely spaced in the coating and homogeneous. This made it so the “sand paper” effect did not increase the abrasive properties of the coating. This made the COF remain low until the wear track reached the unaffected zone of the laser pass. Then the COF returned to the properties of the other coatings. The only issue with this theory is it was not the case for the

5%NbC. The 5%NbC did however experience a drop after 200M, and ended lower than all the other NbC coatings.

4.4.2 NbC Used for Protective Coating

The coating did prove to build well and have good adhesion to the substrate. It seemed to build with lower porosity than the SS304 samples. This meant using the same parameters yielded a coating with a smaller thickness. This could be attributed to the pores closing and having a denser coating, which is more ideal when depositing a protective coating. Based on the results seen this coating could be deposited in a gradient fashion to add extra protection to parts and tailor the properties.

The increase hardness and wear resistance would suggest it could be used to protect hydro components, though the abrasive water test did not show conclusive results. The issue with that test was the water jet is a powerful machine that is designed to cut through just about anything. The aggressive nature of the machine made it so it was very difficult to lower the invasiveness of the cut. The result was all coatings experienced material loss to a degree that it was indistinguishable if more lost from one coating or another. The only results gathered from the test were the 100%VC did not experience damage which was quite impressive. **Fig 4.11** and **Fig 4.12** show the test samples before and after the cut. As you can see, even from a large image, all the samples experience roughly the same amount of damage besides the 100%VC.

Figure 4.11: Abrasive water test samples before test

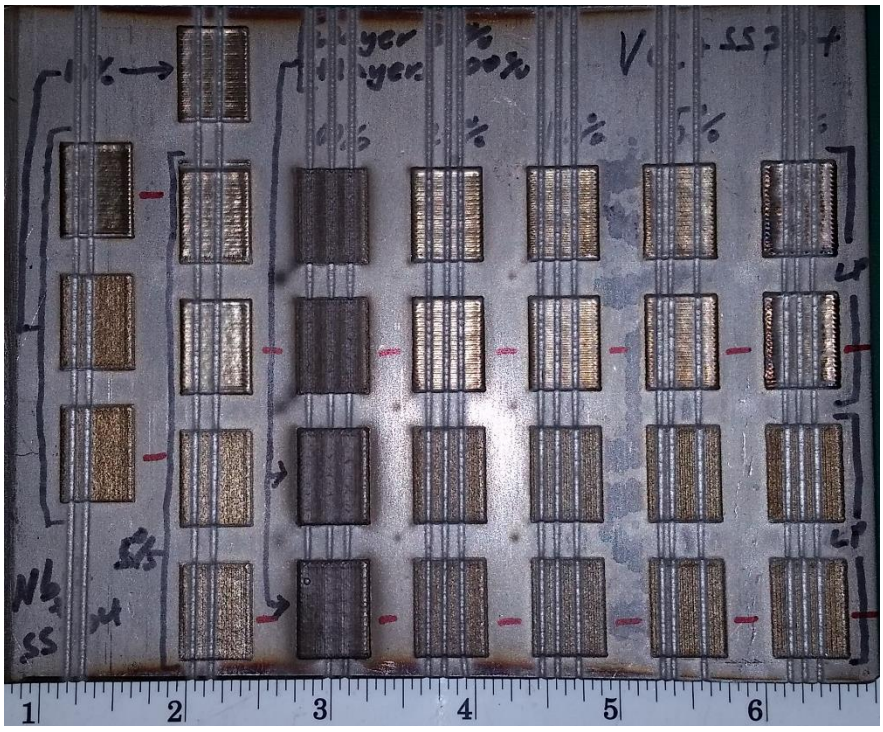

Figure 4.12: Abrasive water test samples after test

4.5 Summary

LENS was able to deposit mixed coating of SS304 and NbC that exhibited higher hardness and wear resistance than only SS304. Laser processing yielded smaller and more homogenous grains with the NbC integrated in the grains and on the grain boundaries. The NbC acted as strengthening particles that increased hardness and wear resistance. The addition of a laser pass increased these properties as well as helped densify the coatings. Adhesion to the substrate appeared to be good with a very small heat affected zone. XRD showed the NbC was FCC and was more was prominent as more NbC was added. The addition of NbC decreased the wear rate of the coating by over 77%. Abrasive water test was inconclusive for the samples because the test was too aggressive to acquire quantitative difference in the material loss. Overall this process could be used to build new parts and apply coatings, or repair damaged ones while simultaneously increasing their resistance to damage in the future.

4.6 References

1. Sen U. Kinetics of niobium carbide coating produced on AISI 1040 steel by thermo-reactive deposition technique. *Mater Chem Phys*. 2004;86(1):189-194. doi:10.1016/j.matchemphys.2004.03.002.
2. Woydt M, Mohrbacher H, Vleugels J, Huang S. Niobium carbide for wear protection – tailoring its properties by processing and stoichiometry. *Met Powder Rep*. 2016;00(00). doi:10.1016/j.mprp.2015.12.010.
3. Plesset BYMS, Ellis AT. On the mechanism of cavitation in centrifugal pumps. *Wear*. 1958;1(4):353. doi:10.1016/0043-1648(58)90042-5.
4. Qiu N, Wang L, Wu S, Likhachev DS. Research on cavitation erosion and wear resistance performance of coatings. *Eng Fail Anal*. 2015;55:208-223. doi:10.1016/j.engfailanal.2015.06.003.
5. Vamsi Krishna B, Bandyopadhyay A. Surface modification of AISI 410 stainless steel using laser engineered net shaping (LENSTM). *Mater Des*. 2009;30(5):1490-1496. doi:10.1016/j.matdes.2008.08.003.
6. Bandyopadhyay A, Dittrick S, Gualtieri T, Wu J, Biomedical WMK, Engineering M.

Calcium phosphate – titanium composites for articulating surfaces of load-bearing implants. *J Mech Behav Biomed Mater*. 2016;57:280-288. doi:10.1016/j.jmbbm.2015.11.022.

7. Chakraborty SS, More H, Racherla V, Nath AK. Journal of Materials Processing Technology Modification of bent angle of mechanically formed stainless steel sheets by laser forming. *J Mater Process Tech*. 2015;222:128-141. doi:10.1016/j.jmatprotec.2015.02.044.

8. Leunda J, Soriano C, Sanz C, Navas VG. Laser Cladding of Vanadium-Carbide Tool Steels for Die Repair. *Phys Procedia*. 2011;12:345-352. doi:10.1016/j.phpro.2011.03.044.

9. Marques MT, Livramento V, Correia JB, Almeida A, Vilar R. Production of copper – niobium carbide nanocomposite powders via mechanical alloying. 2005;399:382-386. doi:10.1016/j.msea.2005.03.090.

10. Orjuelag A, Rincón R, Jairo J. Corrosion resistance of niobium carbide coatings produced on AISI 1045 steel via thermo-reactive diffusion deposition. *Surf Coat Technol*. 2014;259:667-675. doi:10.1016/j.surfcoat.2014.10.012.

11. Shirdel M, Mirzadeh H, Parsa MH. Abnormal grain growth in AISI 304L stainless steel. *Mater Charact*. 2014;97:11-17. doi:10.1016/j.matchar.2014.08.022.

12. Lu J, Sun W, Becker A. Material characterisation and finite element modelling of cyclic plasticity behaviour for 304 stainless steel using a crystal plasticity model. *Int J Mech Sci*. 2016;105:315-329. doi:10.1016/j.ijmecsci.2015.11.024.

13. Wang L, Sun J, Kang B, et al. Electrochemical behaviour and surface conductivity of niobium carbide-modified austenitic stainless steel bipolar plate. *J Power Sources*. 2015;246(2014):775-782. doi:10.1016/j.jpowsour.2013.08.025.

14. Sansone M, Bonis A De, Santagata A, Rau J V, Galasso A, Teghil R. Pulsed laser ablation and deposition of niobium carbide. *Appl Surf Sci*. 2015. doi:10.1016/j.apsusc.2015.10.056.

15. Song Q, Xu Q, Meng J, et al. Preparation of niobium carbide powder by electrochemical reduction in molten salt. *J Alloys Compd*. 2015;647:245-251. doi:10.1016/j.jallcom.2015.05.269.

16. Hassanzadeh-tabrizi SA, Hosseini H, Alizadeh S. In situ synthesis of vanadium carbide – copper nanocomposite by a modified mechanochemical combustion method. *Ceram Int*. 2016:1-4. doi:10.1016/j.ceramint.2016.02.129.

17. Thompson SM, Bian L, Shamsaei N, Yadollahi A. An overview of Direct Laser Deposition for additive manufacturing ; Part I : Transport phenomena , modeling and diagnostics. *Addit Manuf*. 2015;8:36-62. doi:10.1016/j.addma.2015.07.001.

18. Pang W, Man HC, Yue TM. Laser surface coating of Mo–WC metal matrix composite on Ti6Al4V alloy. *Mater Sci Eng A*. 2005;390(1-2):144-153. doi:10.1016/j.msea.2004.07.065.

19. Novichenko D, Marants a., Thivillon L, Bertrand P, Smurov I. Metal matrix composite material by direct metal deposition. *Phys Procedia*. 2011;12(PART 1):296-302. doi:10.1016/j.phpro.2011.03.038.

20. Schneider Y, Soppa E, Kohler C, Mokso R, Roos E. Numerical and experimental investigations of the global and local behaviour of an Al(6061)/Al2O3 metal matrix composite under low cycle fatigue. *Procedia Eng*. 2011;10:1515-1520. doi:10.1016/j.proeng.2011.04.253.

21. Glage a., Weider M, Hasterok M, et al. Mechanical properties of metal matrix composites based on TRIP steel and ZrO2 ceramic foams. *Procedia Eng*. 2011;10:548-555. doi:10.1016/j.proeng.2011.04.092.

22. Baker M a. Advanced characterisation of nanocomposite coatings. *Surf Coatings Technol*. 2007;201(13):6105-6111. doi:10.1016/j.surfcoat.2006.08.118.

23. Medeiros FFP, Da Silva a. GP, De Souza CP. Synthesis of niobium carbide at low temperature and its use in hardmetal. *Powder Technol*. 2002;126(2):155-160. doi:10.1016/S0032-5910(02)00042-6.

CHAPTER FIVE

CONCLUSIONS AND FUTURE WORK

5.1 Conclusions

LENS processing proved to be an effective way of making micro-porous filters and adding hard protective vanadium carbide coatings. As additive manufacturing continues to integrate into modern manufacturing, this shows it has the ability to do so much more. The present studies show the versatility of the LENS. It can make small interconnected filters, adjust porosity, and could add them to a part being built. That same machine can apply a gradient coating to a part for added protection and wear resistance. Or a broken part that has been experiencing material loss could have material added back as well as gain added protection by adding vanadium carbide. It can be used to only partially melt powder to create interconnected channels, or melt vanadium carbide with a melting temperature of 2800˚C.

Conclusions that can be made from this work are:

1. LENS was able to make porous structures with interconnected and varying porosity. It proved to be able to make a micro-porous filter with partially sintered particles obstructing direct passage through the filter. The structure also increased surface area and was reproducible to a 2% porosity difference. Porous structures were made by changing the build parameters as opposed to designing a CAD model of the pore structure.
2. After optimization of build parameters interconnected porous structures were made with porosity ranging from 21% to 15.5%. The configuration of pores would have higher surface area and be ideal for used as a filter due to the globules of metal in the center of the interconnected channels. The ultimate compressive strength varied from 645-556MPa of

the porous cylinders. Microstructure was similar to that of laser processed Ti6Al4V with martensitic like grains.

3. In this thesis LENS was also used to deposit a mixed coating of NbC and VC with SS304 that exhibited higher hardness and wear resistance than only SS304. Laser processing proved to yield smaller and more homogenous grains. The VC and NbC strengthened the alloy by causing stress on the grain boundary, as well as inhibiting grain growth. The addition of a laser pass increased these properties as well as helped densify the coatings.
4. The VC reduced the wear rate by 80% and the NbC by 77%. The hard carbide phase made the coating a metal matrix composite that reinforced the matrix and resisted wear. The side effect is the coefficient of friction increased slightly because of this.
5. The Abrasive water test showed the 100%VC coating was very protective and was not damaged by the water stream. All the other coatings experience some material loss that was hard to measure between the samples. Though there was no distinguishable difference between the material loss of the mixture coatings, it does not mean the coatings would not have higher resistance to abrasive water and cavitation.
6. A case can also be made from these finding that the coatings would have high cavitation resistance. It is incredibly hard, it had excellent wear resistance, and it showed good adhesion to the substrate. The fact it did not experience any damage from a jet of abrasive water that easily cut the other coatings shows it should add a high amount of protection from forces experienced in a hydroelectric generator.
7. This study demonstrated is this process could be used to build new parts and apply coatings, or repair damaged ones while simultaneously increasing their resistance to damage in the future. The coatings were able to be deposited on a SS304 substrate. In the VC study, the

coatings were able to be deposited upon each other, which there is no reason why the other coating could not do this as well. This means a gradient coating could be built using the LENS and be deposited on a 316 or 304 substrate. The properties can be tailored by the amount of carbides present in the stainless steel. Parts could be made to gradually become harder and more wear resistant until there is a 100%VC coating with superior protective properties on the surface.

5.2 Future Work

For the carbide coatings there is large variety of things to still be researched. For both studies processing parameters must be optimized to create a dense coating. Once this is done the true mechanical properties of the coating can be tested. Further research of the mechanical properties should be done, such as compression test to understand how the carbide change the modulus of the coating. In regards to protecting against cavitation, it should be tested on an accelerated cavitation testing in artificial sea water and deionized water should be done. Unfortunately, with no access to these machines this testing could not be done in the present study. On the same lines the corrosion resistance should be studied to see if the added carbides increase its oxidation resistance. To further optimize the coatings the VC should be built in a nitrogen environment due to its ability to bond with nitrogen and make very strong mixed coatings of vanadium carbonitride. Likewise, possibly mix the NbC with boron nitride to make niobium borides which also have shown excellent protective properties.

APPENDIX

COMPRESSIVE DEFORMATION OF POROUS LUNAR REGOLITH

A.1 Introduction

NASA and other space organizations around the world have been trying to develop technology in order to make the idea of creating settlements on the moon a reality[1,2]. In order to make this idea feasible, large structural component must be able to be made by utilizing *in situ* resources such as lunar soil. The surface of the moon is covered in a layer of broken up heterogeneous soil-like rock that has no organic matter termed as regolith[3,4]. The abundance of this regolith makes it an ideal candidate for making building materials for structures if it could be processed into a strong stable building material. Past research has been done on microwave sintering of the lunar soil due to its proposed many advantages compared to conventional sintering[5,6]. Yet few studies have been conducted on conventional sintering to make structural components and had results published. In this study, the ability of making a dense ceramic from JSC-1A lunar regolith powder was tested using conventional sintering techniques. JSC-1A has very little difference from the lunar regolith from the Apollo 17 sample 70051 besides slightly lower amounts of TiO_2 and higher amounts of alkali oxides, making it ideal for this study[7,8]. The objective was to test if the JSC-1A could be pressed and sintered to produce a dense ceramic; as well as see the difference in mechanical strength of the material as a function of porosity.

A.2 Experimental Procedure

The material used was a mixture of JSC-1A, JSC-1AF, and JSC-1AC lunar mare regolith simulant obtained from Orbital Technologies Corporation. The lunar simulant came in powder form ranging from 5mm to less than 25 micron. The powder was sieved in order to have the powder separated into different sizes. Different size powder particles were then pressed up to

~145MPa using 12.7 mm and 7 mm diameter cylindrical dies keeping the height to diameter ratio between 2:1 and 1.5:1. By changing the powder size being packed together the porosity was able to be changed and controlled. Samples were sintered in a Zircar Hot Spot 110 (Zircar, Florida, New York) furnace at 1200°C for 20 min.

The phases of the sintered samples were analyzed and compared to the phases in the original powder using X-ray diffraction (XRD) analysis using a Siemens D-500 X-ray powder diffractometer (Siemens AG, Karlsruhe, Germany) with CuK_{α} radiation and a Ni-filter. The microstructure was observed using a field emission scanning electron microscopy (FEI Quanta 200) (FEI Inc., OR, USA). The apparent density of the samples was calculated using Archimedes method.

Compression tests were conducted on the sintered samples using a screw-driven universal testing machine (AG-IS, Shimadzu, Japan). The test had a constant stroke rate of 0.5 mm per minute until fracture. Hardness tests were conducted using a Vickers micro-hardness tester (Shimadzu, HMV-2T) at a load of 100g (0.98N) with a dwell time of 15s. At least ten tests were conducted and the average value is reported here.

A.3 Results and discussion

A.3.0 Microstructure and Phase Analysis

A micrograph of the polished surface of one of the higher porosity samples is shown in **Fig A.1**. Pores are present which appear to be closed with some interconnectivity. In another study of JSC-1AF, the hematite phase reduced to magnetite while in an oxygen environment. This reduction caused oxygen to be released which resulted in bubble type voids and porosity[9]. Pores seen in Fig. 1 are very similar and hypothesized that they are a result of the oxygen release

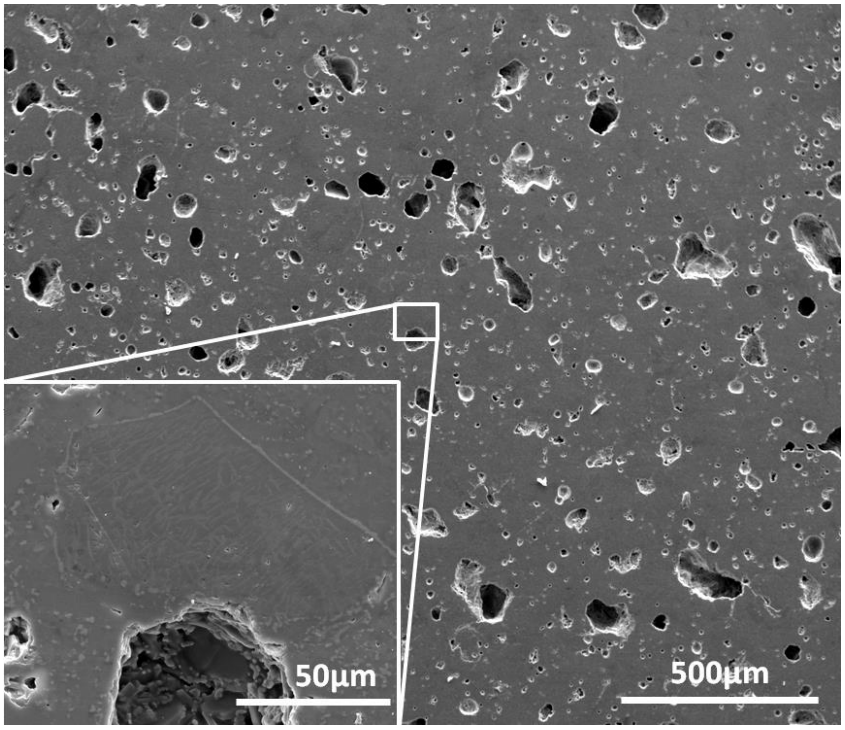

Figure A.1: Polished surface of high porosity JSC-1A sintered sample

during sintering. The porosity is also the result of the free space between the coarse grains prior to heat treating. During sintering the grains bond where the surfaces are in contact, but the larger spaces between them do not always fill in leaving porosity. The higher magnification image shows a pore with dense ceramic surrounding it. Such result confirms that the JSC-1A particles did sinter together and create a dense ceramic structure. The low porosity samples look the same but have fewer smaller pores. Melting temperature of JSC-1A was reported to be 1120°C.[7] In our study, complete melting was not noticed however liquid phase sintering was evident from the polished microstructures[10]. **Fig A.2** shows the fracture surface of the low porosity sample at both lower and higher magnifications. It can be seen that the initial failure appears to have started on the edges of the cylinder and propagated across the body. It is common in ceramic bodies pressed using a die to have higher porosity near the edges due to frictional forces which causes a porosity gradient from the surface to the inside[11]. **Fig A.3** shows the higher porosity samples' fracture surface.

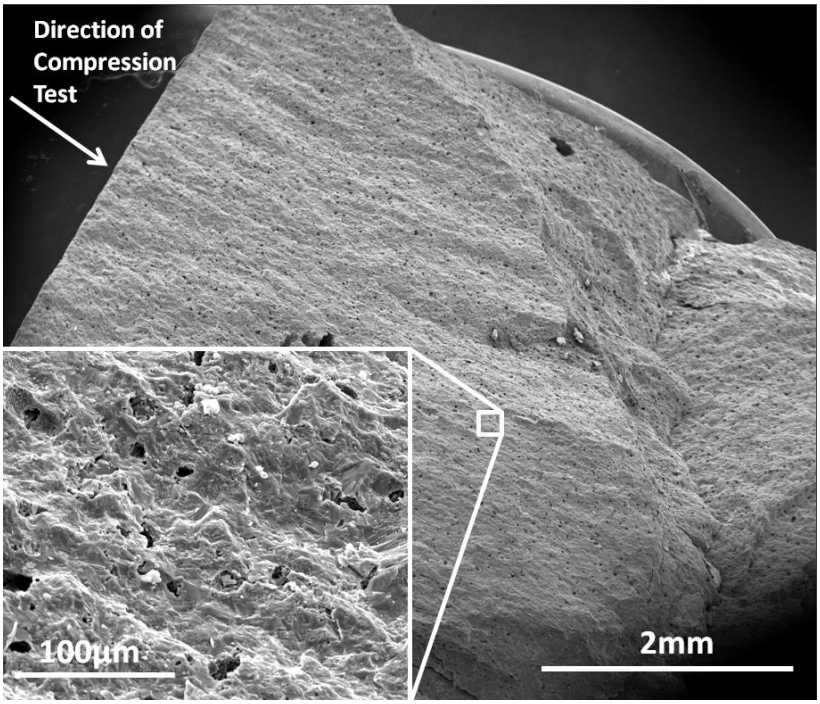

Figure A.2: Fracture surface of low porosity JSC-1A sintered sample.

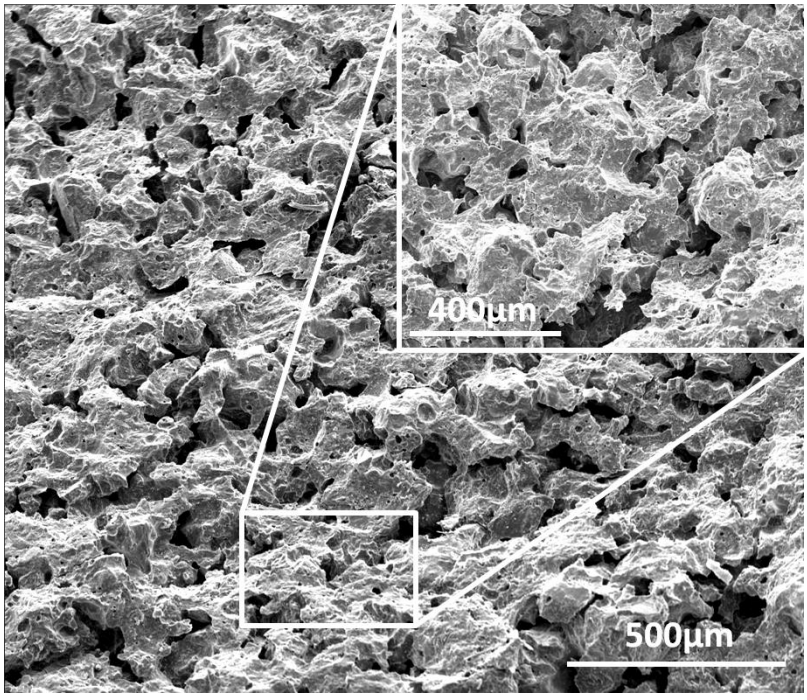

Figure A.3: Fracture surface of high porosity JSC-1A sample.

XRD results showed that the as received JSC-1A did have the phases of anorthite and forsterite as seen in other studies (Results not shown)[7,12]. The sintered powder did appear to undergo some phase changes. It retained the anorthite phase but lost the forsterite. The new phases detected were albite, diopside, enstatite, and hematite (Results not shown).

A.3.1 Mechanical Properties

Hardness test results can be seen in **Table A.1**. The average hardness was 1030.2 $HV_{0.1}$ ± 69.73 $HV_{0.1}$. Table 1 also shows the compression test results. The results show the 99.0 +/-0.5% dense samples had a failure stress on average of 232 MPa with an average modulus of elasticity of 10.9 GPa. The 92+/-2% dense failure stress was 103.2 MPa and its average modulus of elasticity was 5.98 GPa.

Table A.1: Hardness and compression test results for JSC-1A	**Apparent Porosity (%)**	**Failure Stress (MPa)**	**E (GPa)**	**Hardness ($HV_{0.1}$)**
99.0% Dense (+/- 0.5%) Avg.	**0.41**	**232**	**10.9**	**1027**
Standard Deviation	0.24	43.7	1.89	98.41
92% Dense (+/- 2%) Avg.	**8.44**	**103.2**	**5.98**	**"**
Standard Deviation	1.44	26.7	0.71	"

The hardness results proved to be quite high and comparable to materials like Mg-PSZ (1020HV_{30}) and other commercial grade zirconia[13]. The compression test showed that lowering the porosity did increase the failure stress and modulus of elasticity. On average raising the porosity from 8% ±2% to 1.0%±0.5% raised the failure stress by ~77%. **Fig A.4** shows two representative compression test plots. Both tests had the same stress-strain curve shape, but the

lower porosity has a higher slope than the high porosity sample. We have used Ryshkewitch equation[14] on our porous ceramic data -

$$\sigma = \sigma_0 e^{-BP}$$

where σ = Strength of porous body, σ_0 = Strength of nonporous body of the same material, P = porosity expressed as fraction and B = Slope of ln σ vs. P, a materials constant. Based on our data, the calculated value for σ_0 is 240.7 MPa and B is 0.123. Theoretically, if the JSC-1A can be sintered into full density with zero porosity, the compressive strength should be ~240.7 MPa. It is worth noting that the theoretical strength is projected based on our average compressive strength, and not based on the highest strength data that we have measured. The highest strength data measured for JSC-1A was 275.5 MPa for 99.5% dense sample. If we use Ryshkewitch's equation to calculate σ_0, the calculated value for σ_0 is 282.2 MPa considering full density. In both cases of curve fitting, R^2 was 0.99.

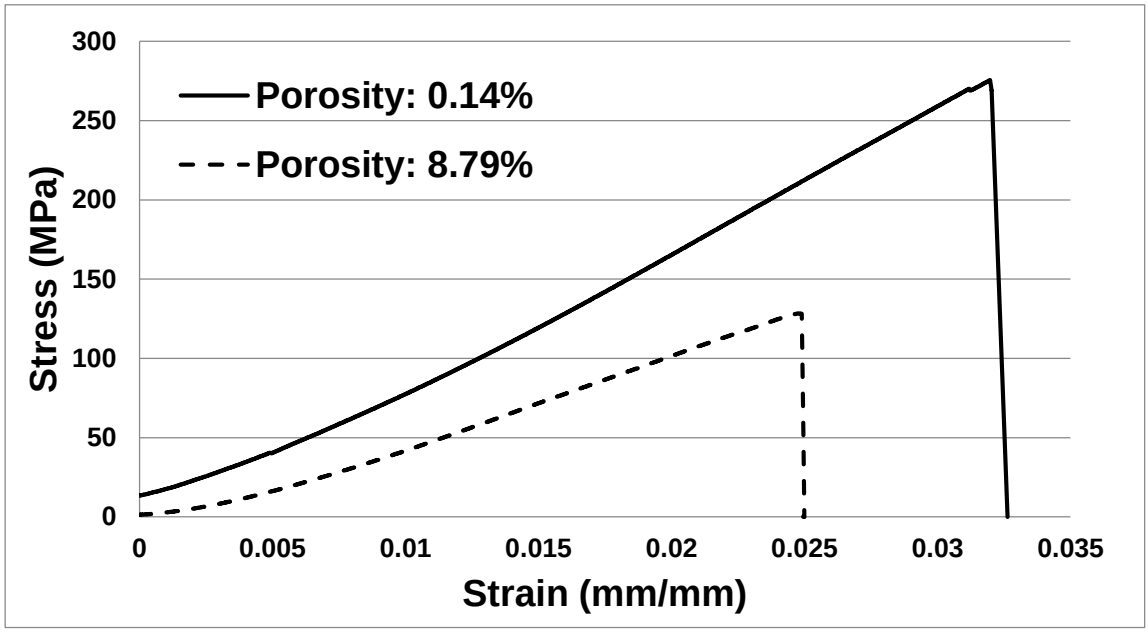

Figure A.4: Stress - strain plot of high and low porosity JSC-1A samples.

The failure stress exhibited by the cylinders was quite high and shows that the regolith has the possibility of being used for structural components. This is especially true if the sintered moon rock could be made dense which was found to be possible. The method of packing the very fine powder in a die worked well. The powder had a tendency to agglomerate and flow was not good when it was only particles smaller than 45μm.This was overcome by mixing the powders of different sizes. The result was a dense product but easier to handle. It was also easy to make a more porous sample if desired using the method of mixing larger particle size powder in the starting material. Samples were even made to have porosity as large as 12% without using any pore formers.

The technique of sieving powder and then pressing and heating could be feasible to employ in a lunar environment. The regolith taken from multiple sites of the Apollo 12 and 14 missions, as well as other missions, had a median grain size of 0.05 mm to 0.735 mm and went as low as 40μm[2,15,16]. This means the powders could be sieved to the sized used in this experiment without any extra processing. The results from sintering on the lunar surface should be close to the same if real lunar regolith was used due to the fact JSC-1A is very similar as mentioned earlier. Though it should be noted that some areas do have different compositions and there could be variation depending on where the soil is harvested from on the lunar surface[16,17,18].

A.4 Summary

In this study JSC-1A was successfully pressed and sintered to produce a dense ceramics body. It was found that JSC-1A could be pressed in a die and will hold together well enough to be moved to a furnace and not break. A sintering process was found that caused the powder to undergo liquid phase sintering and created a strong ceramic body. Microstructural analysis showed that new phases developed during sintering. The final samples had average failure stress

in compression of 232 MPa and 103.2 MPa for 99.0 +/-0.5% and 92 +/-2% dense samples, respectively.

A.5 References

1. M.Green, T. Talbert,. *Office of the Chief Technologist*. NASA. October 31, 2012 http://www.nasa.gov/offices/oct/home/niac_countour_crafting.html
2. M. Iai. R. Luna. Journal of Aerospace Engineering, © American Society of Civil Engineers. 2011. 24:433-441
3. F.Cain. (2008, October 30). *Lunar Regolith.* Retrieved from Universe Today: http://www.universetoday.com/20360/lunar-regolith/
4. J. S. McCloy, S. K. Sundaram, J. Matyas, P. P. Woskov. Review of Scientific Instruments 82, 054703 (2011). American Institute of Physicts. © 2011. doi: 10.1063/1.3590016
5. L. Taylor, T. Meek, (2005). Microwave Sintering of Lunar Soil: Properties, Theory, and Practice. Journal of Aerospace Engineering, 18(3), 188-196. Doi:10.1061/(ASCE)0893-1321(2005)18:3(188)
6. T. Meek, D. Vaniman, R. Blake, M. Godbole. (1987). Sintering of Lunar Soil Simulants Using 2.45GHz Microwave Radiation. Abstracts of the Lunar and Planetary Science Conference, vol. 18, page 635.
7. C.Ray, S.Reis, S.Sen, J. O'Dell. Journal of Non-Crystalline Solids, 2010, 356, 2369-2374.
8. K. A. Alshibli. A. Hasan. Journal of Geotechnical and Geoenvironmental Engineering © American Society of Civil Engineers. 2009.135:673-679.
9. J.Matyas, R.Wegeng, M. Robinson, A.Casella, J. McCloy. AIAA SPACE 2011 Conference & Exposition 27-29 September 2011. Long Beach, California: The American Institute of Aeronautics and Astronautics, Inc. .
10. R. M. German. Liquid Phase Sinering. Plenum Press, New York. © 1985
11. Rice, R. W. *Porosity of Ceramics.* New York: Marcel Dekker, Inc. 1998
12. Owens, C. (2006, December 12). Retrieved from Orbitec: http://www.orbitec.com/store/JSC-1AF_Characterization.pdf
13. AZoM.com. Zirconia -Physical and Mechanical Property Comparision of the different types of Zirconias. July 23, 2014, http://www.azom.com/article.aspx?ArticleID=940
14. W. Duckworth. Discussion of Ryshkewitch paper by Winston Duckworth. Journal of The American Ceramic Society. Vol. 36, No. 2.

15. J. K. Mitchell, L. G. Bromwell, D.Carrier III, N. C. Costes, R. F. Scott. Journal of Geophysical Research, 1972, October 10, 77(29), 5642-5664

16. C. Meyer. Lunar Sample Compendium. 74220 Soil (or clod) 1180 grams. 2010

17. E. Roedder. P. W. Weiblen. Apollo 17 "Orange Soil" – a result of Meteorite Impact on Liquid Lava? Reprinted from Nature. July 27, 1973. Vol. 244, No. 5413, pp. 210-212,

18. D. S. McKay. D. A. Morrison. Journal of Geophysical Research. Vol. 76, No. 23. August 10, 1971